UCLouvain

École polytechnique de Louvain

Stable porous silicon membranes for biosensing

Author: **Clara Whyte Ferreira**
Supervisor: **Laurent Francis**
Readers: **Roselien Vercauteren, Sophie Demoustier**
Academic year 2020–2021
Master [120] in Chemical and Materials Engineering

Abstract

In this work, a robust fabrication method for stable mesoporous silicon membranes using standard microfabrication techniques is presented. Over the last three decades, the interest in porous silicon (PSi) has grown due to its highly tunable and remarkable properties that can be dramatically different from those of bulk silicon. The fabrication of porous silicon membranes (PSiM) is achieved by detaching the porous layer from the underlying bulk silicon substrate. The formation of this permeable barrier helps to overcome the infiltration limitations of close-ended PSi and allows its application to different fields, such as optical detection, drug delivery, microfluidics, energy conversion and electronics. The application of interest in this work is enabling real-time optical biosensing.

Due to the high reactivity of the hydride terminated surface species present on the porous silicon surface, the as-prepared matrix is not stable in aqueous solution. In order to passivate the PSi membrane and decrease the biosensor's limit of detection to competitive levels, atomic layer deposition was used to coat the porous matrix with different metal oxides, namely aluminum oxide (Al_2O_3), hafnium oxide (HfO_2), and titanium oxide (TiO_2). The fabricated membranes were characterized in terms of morphology, optical, mechanical and chemical properties. Stability tests, resistance to flow analysis, and noise level determination were also performed.

Finally, the biosensing performance of an Al_2O_3 passivated porous silicon membrane was tested through selective optical detection of bacteria lysate in phosphate buffered saline using PlyB221, an endolysin encoded by the bacteriophage Deep-Blue targeting the B. *cereus*. The biosensor was able to detect the bacterial lysate, with an initial bacteria concentration of 10^6 colony forming units per mL (CFU/mL), in less than 10 min.

Acknowledgements

Becoming an engineer is a challenging journey that one cannot travel alone. In this path, I had the chance to meet outstanding people who have helped me grow and arrive at the conclusion of my master thesis.

I would first like to thank Prof. Laurent Francis for the opportunity to work on this subject, as well as for his guidance and supervision during the past few months. I am also grateful to Prof. Sophie Demoustier for the availability to be a part of my jury and to read my final work.

My sincere thanks to Roselien Vercauteren for her immeasurable help, enthusiasm, availability, and consistent guidance. This work's objectives would never have been achieved without her. I will always be grateful for her teachings, patience, and support that helped shape me into a better engineer and researcher.

My acknowledgments go also to Romain Tuyaerts for all his insights, motivation, and assistance. Thank you for all the challenging and enthusiastic scientific discussions.

I appreciate the help from the whole WINFAB staff, members, and users. Special thanks to Nicolas André for his availability and so many good ideas, to Sebastian Faniel for his assistance with the atomic layer depositions, and to Benjamin Huet for sharing his research experience.

Thanks to Grégoire Le Brun, Romain Hanus, Rafael Puyol, and Margot Hauwaert for sharing their office, knowledge, and kindness.

To Audrey Favache, thanks for her incredible patience and valuable help with the nanoindentation technique. Thanks also to Prof. Arnaud Delcorte and Pierre Eloy for their help with XPS characterization.

I am very grateful to my parents, Juliane and Lauro, and to my brother Arthur for their encouragement all along the way and their unshakable faith in me. Many thanks to Rafael for all his love and support.

List of acronyms

WHO World Health Organization

AMR antimicrobial resistance

CDC Centers for Disease Control and Prevention

PCR polymerase chain reaction

ELISA enzyme-linked immunosorbent assay

ALD Atomic Layer Deposition

APTES 3-aminopropyltriethoxysilane

APDMES 3-aminopropyldimethylethoxysilane

MALDI-TOF MS matrix-assisted laser desorption ionization time-of-flight mass spectroscopy

LoD limit of detection

RIFTS reflective interferometric Fourier transform spectroscopy

FFT fast Fourier transform

EOT effective optical thickness

PSi porous silicon

PSiM porous silicon membrane

CFU colony forming unit

SLIM spectroscopic liquid infiltration method

PL photoluminescence

SERS surface enhanced Raman scattering

Contents

Chapter 1

Introduction

If there is one lesson humankind can take from the 21st century's second decade beginning is how fast diseases can spread in a globalized world. Furthermore, they can have a major impact in health and well-being linked to social, economic, political and environmental aspects. In parallel to this scenario, antimicrobial resistance (AMR) is a growing and pressing issue. AMR is a result from the survival of infectious micro-organisms (e.g. bacteria) that would normally be killed or prevented from growing by regular antimicrobial drugs. Once these strains have survived, they grow and spread due to the lack of competition from other strains. Although resistance to antimicrobials is a natural process, it has been growing in an alarming rate during the past years because of overuse of these drugs [1].

Most antimicrobials prescriptions, and especially for antibiotics are made outside the hospital, by doctors without without a proper diagnosis, by pharmacists or by self-medicating patients buying antibiotics 'over-the-counter' (i.e. without a prescription from a doctor). Many of these prescriptions are given based on the so-called "empirical diagnosis" that comes from intuition and expertise of medical professionals. This is a consequence of the fact that the available diagnostic tools are time consuming (up to 36h culture of bacteria) and acutely ill patients cannot wait that long. Furthermore, even when health risks are not that high most doctors' surgeries and pharmacies are under time, patient and financial pressure, and must address patients' needs much faster. These scenario shows how rapid diagnostics can have a major impact in the use of antibiotics, by letting doctors know if a patient has an infection and if this infection is viral or bacterial, ensuring that only the patients that actually need the medication will get it [1].

Biosensors have received interest from the scientific community in the pursue of a cheap, fast, specific, and sensitive diagnostic approach [2]. These devices could have an important impact in deceleration of AMR growth, but also in the control of epidemics and food-born outbreaks, in providing diagnosis where access to a fully equipped laboratory is not possible, and for time-sensitive infections [3].

Master thesis objectives

This master thesis focuses on the development of a versatile, fast-diagnosis, selective and sensitive biosensor for bacteria detection. In order to do so, an optical detection

scheme based on porous silicon membranes is proposed. Porous silicon is the substrate of choice due to its easily tunable properties and straight-forward route of fabrication. The optical biosensing scheme can also be easily implemented and the biosensor is sensitive to minute changes in its environment. Differently from other biosensors proposed in the literature [4], the method of detection presented here does not use a biorecognition layer. The bacteria are detected by first performing a selective lysis of the targeted bacteria by an endolysin in a vial; and secondly, optically monitoring the bacterial lysate filtering through a porous silicon membrane using the reflective interferometric Fourier transform spectroscopy (RIFTS), as proposed by Vercauteren *et al.* [5]. The concept is illustrated with a selective optical detection of *B. cereus* lysate in phosphate buffered saline using the recently characterized PlyB221 endolysins, encoded by the Deep-Blue phage targeting *B. cereus*[6].

One of the issues with freshly-etched porous silicon is the presence of hydride terminated groups which makes the structure highly reactive and unstable [4]. Therefore, the main goal of this thesis is improving the stability of porous silicon membranes in aqueous media, together with the reduction of the noise level and, as a consequence, decreasing the the limit of detection to a competitive value ($<10^3$ CFU/mL[1]). Furthermore, an investigation of the mechanical properties is proposed to better understand to which extent these parameters are affected by porosity and pore size.

Master thesis outline

This master thesis is organized as follows:

- **Chapter 2** reviews the bacteria detection methods currently adopted in the diagnostic field and biosensing alternatives for these techniques. Porous silicon is presented as a substrate for biosensing and its fundamentals, fabrication techniques, common architectures, challenges, and characterization techniques are discussed. Finally, the advantages of using porous silicon membranes and an optical detection scheme are presented.
- **Chapter 3** discusses passivation strategies commonly used to stabilize porous silicon surface chemistry. The fabrication of passivated porous silicon membranes through the atomic layer deposition of Al_2O3, TiO_2 and HfO_2 is performed. The membranes are characterized in terms of morphology, optical, mechanical and chemical properties. Stability tests, resistance to flow analysis, and noise level determination are also conducted. The optical drift over time, due to the porous matrix degradation, show the advantage of atomic layer deposition passivation over low temperature oxidation for more accurate optical measurements.
- **Chapter 4** demonstrates the use of an Al_2O_3 passivated porous silicon membrane for optical biosensing of *B. cereus* lysate.
- **Chapter 5** summarizes the scientific findings and proposes some perspectives for further improvement of the biosensor in order to achieve the required performance for a point-of-care testing device.

[1]CFU stand for colony-forming unit, used to estimate the number of viable bacteria in a sample

Chapter 2

Biosensing and porous silicon: state of the art

Contents

Overview

This chapter offers an overview of the bacteria detection methods currently adopted in the diagnostic field and biosensing alternatives for these well-established techniques. Porous silicon (PSi)-based biosensors are discussed along with fabrication techniques, common architectures, challenges, and characterization. Special focus is given to porous silicon optical biosensors and porous silicon membranes.

2.1 Bacterial detection

Pathogenic bacteria proliferation, especially antibiotic-resistant bacteria, is one of the main threats to global health. The World Health Organization (WHO) declared antimicrobial resistance (AMR) as one of the top 10 global public health threats facing humanity [7].

According to the Centers for Disease Control and Prevention (CDC)'s on Antibiotic Resistance Threats in the United States (2019), more than 2.8 million antibiotic-resistant infections occur in the United States each year, and more than 35.000 people die as a result [8]. Worldwide, 700.000 people die of resistant infections every year and it is estimated that, by 2050, this number will increase to 10 million lives a year. Furthermore, if action is not taken, the cost in terms of lost global production between now and 2050 would reach 100 trillion USD [1]. Figure 2.1 shows a comparative graph of deaths from drug-resistant infections and other causes, including bacterial diseases (tetanus and cholera) and diarrhoeal disease (caused by bacteria, viruses, and other pathogens). It can be seen that AMR could become a lead cause of death.

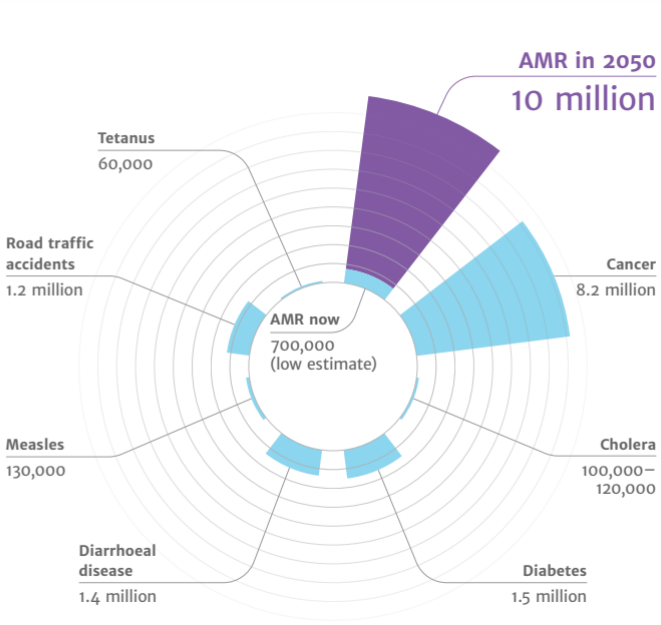

Figure 2.1: Annual deaths from drug-resistant infections and other causes, now and by 2050. Extracted from [1].

Moreover, according to the WHO, food safety is also a public health priority. Foodborne illnesses are usually infectious or toxic in nature and caused by bacteria, viruses, parasites, or chemical substances entering the body through contaminated food or water. Diarrhoeal diseases are the most common illnesses resulting from the consumption of contaminated food, causing 550 million people to fall ill and 230.000 deaths every year. It is also the second leading cause of death in children under five years old. Among the most common foodborne pathogens are *Salmonella*, *Campylobacter*, and *Enterohaemorrhagic Escherichia coli* (*E. coli*).

Detection and identification of contamination due to pathogens in an early stage is, thus, a key concern due to the enormous social and economic impact of infections caused by microorganisms. In order to tackle the antimicrobial resistance growing issue, the causative agents must be identified as rapidly as possible, so that directed patient treatment and/or contact precautions can be initiated [9].

The most common tools used for pathogen detection are polymerase chain reaction (PCR), culture and colony counting methods, enzyme-linked immunosorbent assay (ELISA) and matrix-assisted laser desorption ionization time-of-flight mass spectroscopy (MALDI-TOF MS). They involve DNA analysis, counting of bacteria, antigen–antibody interactions, and chemical compound analysis, respectively. These methods are widely used for their high sensitivity and selectivity. However, they present some disadvantages as the time required for the analysis and the complexity of their use [10]. The mentioned methods are further described in this section and summarized in table 2.1.

Table 2.1: Conventional methods of bacteria detection [9, 10, 11, 12].

	Selectivity	**Limit of detection**	**Assay time**	**Cost**
Culture	Low	Low CFU	> ½ day	Low
MALDI-TOF MS	High	10^5 CFU/mL	0.2-3h after culture	High
PCR	Very high	$10 - 10^5$ CFU/mL	>2h	High
ELISA	High	$10^3 - 10^4$ CFU/mL	> ½ day	High

2.1.1 Culture and colony counting method

The majority of clinical microbiology laboratories still rely on culture for the detection of most bacterial pathogens from clinical samples. Traditionally, culture is performed using general purpose agar based media (*e.g.* blood agar) that will support the growth of a wide range of pathogens. The detection is usually carried out using optical methods, mainly by ocular inspection [10].

The culture and colony counting method is the oldest bacterial detection technique and remains the standard detection method because it is inexpensive and relatively sensitive (low CFU/mL detection limit). However, the method is highly time-consuming, requiring 24-48h [13] for culture growth and taking up to 16 days for confirmed positive results depending on the bacteria to be detected [10].

2.1.2 Polymerase chain reaction (PCR)

The polymerase chain reaction (PCR) method is less time-consuming than other techniques such as culturing and plating. It takes from 5 to 24h to produce results (depending on the specific PCR variation used, *i.e.* real-time PCR, multiplex PCR, reverse transcriptase PCR, etc.) without taking into consideration any previous enrichment steps [10]. Furthermore, amplification of DNA, using PCR methods, provides a means of producing large quantities of DNA from a relatively small number of organisms. Traditional culture methods often lack the sensitivity and specificity that can be attained with the PCR method to amplify

targeted regions of the bacterial [14].

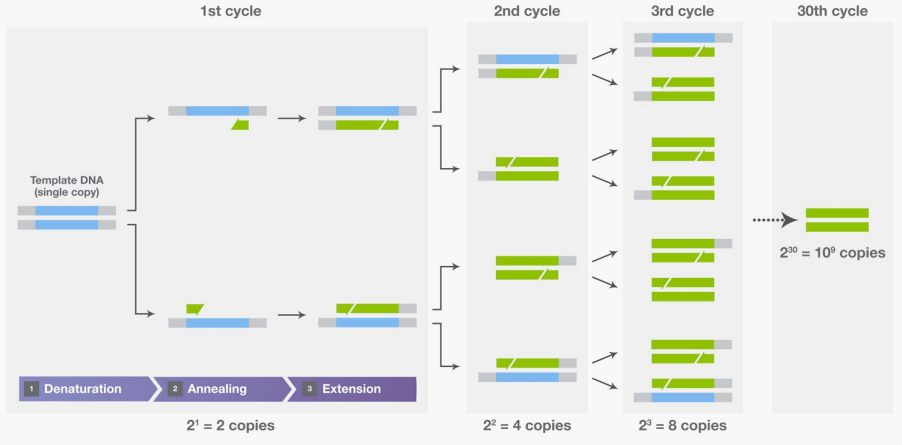

Figure 2.2: Three steps of PCR - denaturation, annealing, and extension as shown in the first cycle, and the exponential amplification of target DNA with repeated cycling. Extracted from [15].

PCR is a biochemical process capable of amplifying a single DNA molecule into millions of copies in a short time, as shown in figure 2.2. Amplification is achieved by a series of three steps [15]: denaturation, annealing and extension. These steps are followed by exponential amplification with repeated cycling. The presence of the amplified sequence is subsequently detected by gel electrophoresis that separates DNA fragments according to their size through the application of an electrical field. Finally, the limit of detection ranges from $10 - 10^5$ CFU/mL [10].

2.1.3 Enzyme-linked immunosorbent assay (ELISA)

The enzyme-linked immunosorbent assay (ELISA) has become one of the most widely used serological tests for antibody or antigen detection. This test involves the linking of various "label" enzymes to either antigens or antibodies.

Figure 2.3 shows the double antibody sandwich assay method used for the detection of antigens. In this method, a specific antibody is fixated on a well. Then, a test antigen is added and, in case it reacts with the specific antibody, it is retained after the well is washed (unbound antigen will be washed away). The next step consists of adding a commercially prepared antibody-enzyme conjugate specific for the antigen. A complex of outer antibody-enzyme, middle antigen, and inner antibody is formed (*i.e.,* a layered Ab-Ag-Ab sandwich). A substrate is added and the enzyme will convert it to a colored product. This resulting colored product can be quantitatively measured by optical density scanning of the plate [16].

If the antigen has reacted with the absorbed antibodies in the first step, the ELISA test is positive (*i.e.*, it is colored). If the antigen is not recognized by the absorbed antibody, the ELISA test is negative because the unattached antigen has been washed away, and no antibody-enzyme is bound (it is colorless) [16]. Another method is called indirect immunosorbent assay approach that detects antibodies rather than antigens by fixing the

antigen directly to the well instead of binding it to the antibody.

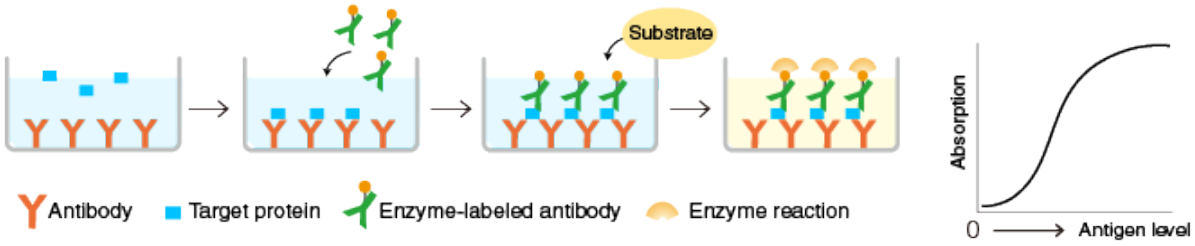

Figure 2.3: The direct or double antibody sandwich method for the detection of antigens, ELISA test. Extracted from [17].

This technique is very powerful due to its high selectivity for a wide range of targets, unfortunately, it is quite complex and expensive [3]. Furthermore, each step requires long incubation times, and to achieve the required sensitivity bacteria need to be concentrated into a smaller volume or cultured prior to assay [18]. Nevertheless, it is one of the most established techniques nowadays as well as the source of inspiration for many biosensor applications. Its limit of detection ranges from $10^3 - 10^4$ CFU/mL and the analysis time is typically one day [10].

2.1.4 Matrix-assisted laser desorption ionization time-of-flight mass spectroscopy (MALDI-TOF MS)

In recent years, MALDI-TOF MS has emerged as a potential tool for microbial identification and diagnosis [14]. The process is illustrated in figure 2.4. First, the analyte is prepared by mixing or coating with an energy-absorbent matrix, and dried to remove the liquid solvent, forming a "solid-solution" of analyte-doped matrix crystals. The sample within the matrix is ionized, *i.e.* bulk portions of the "solid solution" are removed by laser ablation, and the protonated ions are separated on the basis of their mass-to-charge ratio (m/z). Finally, a mass analyzer (typically a time-of-flight analyzer for biological applications) is used to detect and measure the samples. A characteristic spectrum is generated for analytes in the sample and detection can be made by comparing it to known database (by matching the masses of biomarkers of unknown organism with the proteome database). This technique holds some advantages such as relatively fast detection, high accuracy, lower cost than molecular and immunological-based detection methods and no requirement of trained laboratory personnel. However, the initial cost of the the MALDI-TOF equipment is high [14]. Furthermore, identification requires approximately 10^5 CFU/mL, thus, organisms to be cultured before analysis [11].

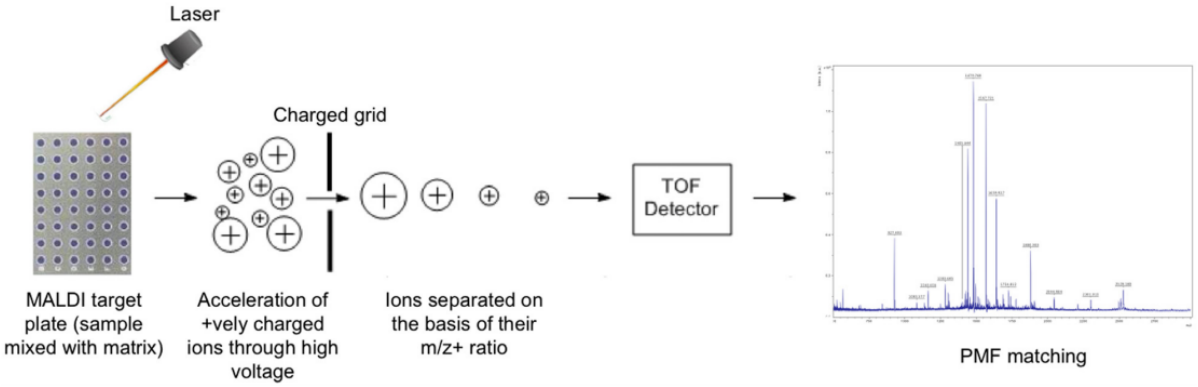

Figure 2.4: Schematic diagram showing the work-flow in a MALDI-TOF MS. Extracted from [14].

2.2 Biosensors

As previously discussed, determination and detection of bacteria with traditional biochemical assays are inherently time-consuming and laborious task. Nevertheless, quick, sensitive, cost-effective and accurate bacterial detection methods need to be developed to identify pathogens at an early stage. Biosensors provide new analytical equipment which are sensitive, fast and portable [19].

Biosensors were first introduced by Clark and Lyons in 1962 when they developed an enzyme (glucose oxidase) containing membrane for the detection of glucose [20]. Since then, the field has much evolved and the merge of biosensors with nanotechnology led to important breakthroughs in diagnostic medicine. Nanotechnology is at the forefront of diagnostic science because of its wide range of applications in the field of biosensing due to its higher surface area to volume ratio, electrochemical properties, and ability to manifest biological signaling and transduction mechanism [21].

Biosensors can be defined as measurement systems for analyte detection that combine a biological component with a physiochemical detector. Usually, these devices detect biomolecules such as nucleic acids, proteins, and cells that are associated with a disease. They are composed of three main parts: a biological sensing platform, a transducer, and a signal processor, as shown in figure 2.5. The sensing element is usually called bioreceptor and emulates in vivo molecular recognition phenomena. Sensing elements can be cells, microbes, cell receptors, antibodies, enzymes, or nucleic acid. The second element, the transducer or detector, senses the signal related to the physiochemical (*e.g.* optical, electrochemical or mass-based) change caused by the interaction between the bioreceptor and the analyte. Its function is transforming this signal into another one that can be evaluated and quantified. Finally, the last part of the biosensor is the reader device or signal processor that usually involves a software and a hardware to generate results that can be interpreted and analyzed [22].

The performance of a biosensor depends on the optimization of certain static and dynamic attributes [23]:

- **Selectivity** - the ability of a biosensor to interact specifically with the desired analyte mixed with other substances and contaminants. This is the main feature to take under consideration when choosing bioreceptors.
- **Reproducibility** - the ability of the biosensor to generate identical responses for a duplicated experimental set-up. This feature is characterized by the precision and accuracy of the transducer and electronics in a biosensor. Reproducible signals are responsible for the reliability and robustness of the sensor.
- **Stability** - the degree of susceptibility to ambient disturbances in and around the biosensing system. Drifts can be observed in the output signal if the system is subjected to these disturbances under measurement. This feature has a direct impact on the error in the measured concentration and can affect the precision and accuracy of the sensor. In application where high incubation time or continuous monitoring are required, stability is crucial. Some factors that can influence stability include temperature sensitivity of transduction and electronics, affinity of the bioreceptor (degree to which the analyte binds to the bioreceptor) and degradation over a period of time.
- **Sensitivity** - the minimum amount of analyte that can be detected by a biosensor. Sensitivity can be also translated as the limit of detection (LoD). In several medical and environmental applications, sensitivity is required to be as low as ng/ml or even fg/ml to confirm the presence of traces of analytes in a sample. For bacteria detection, it can also be measure by CFU/mL (at least one living and growing cell) and cells/mL (living and dead cells).
- **Linearity** - the attribute that shows the accuracy of the measured response (for a set of measurements with different concentrations of analyte) to a straight line. Mathematically, it is represented as $y = mc$ where c is the anayte concentration, m the sensitivity of the biosensor and y the output signal. This feature can be associated with the resolution of the biosensor and range of analyte concentrations under test. Resolution, in this context, is defined as the smallest change in analyte concentration needed to induce a detectable response. Linearity is also associated with linear range, i.e. the range of analyte concentrations for which the biosensor response changes linearly with the concentration.

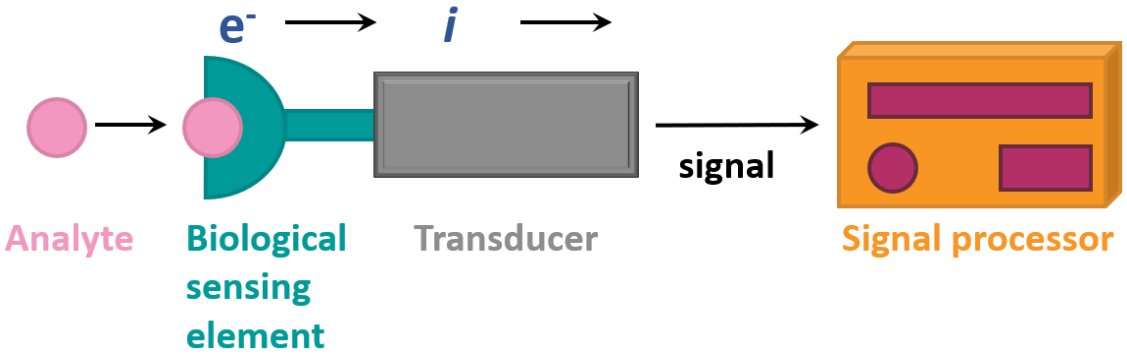

Figure 2.5: Scheme of a biosensor basic design. Adapted from [24].

Biosensors are classified according to their transduction method and their biorecognition element, as shown in figure 2.6. The most common transduction methods are optical, electrochemical and mass-based. These will be discussed in more details in the following sections.

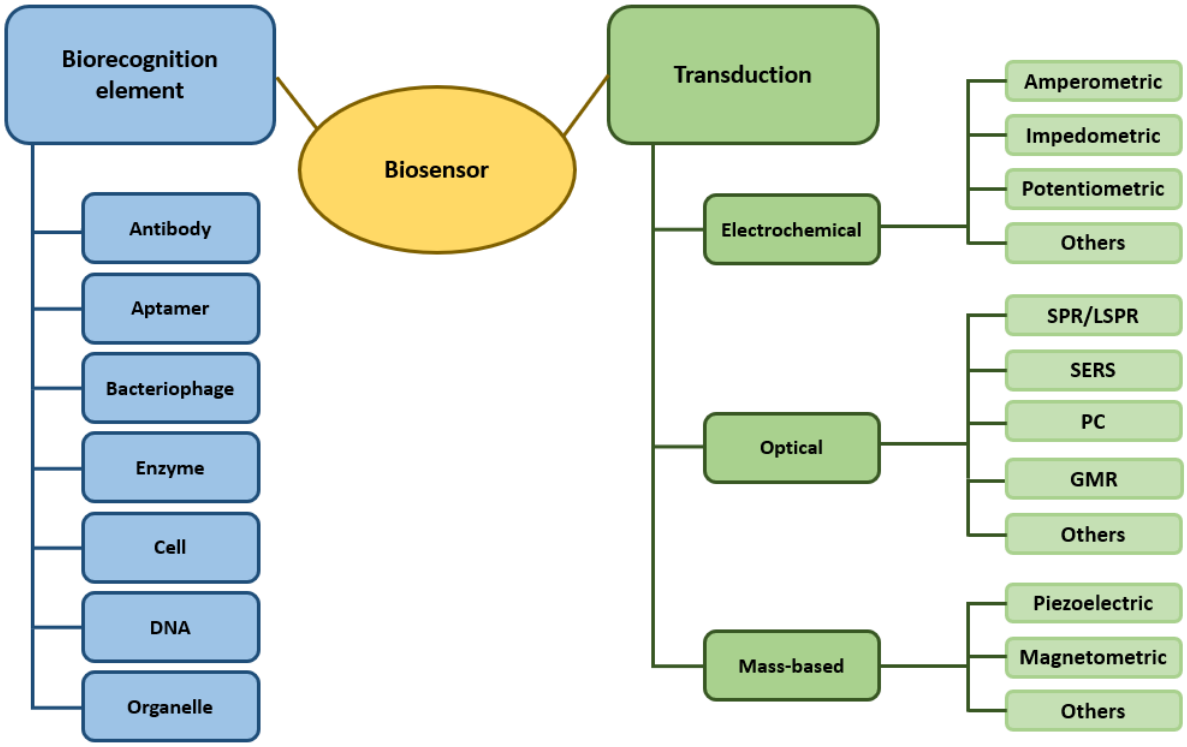

Figure 2.6: Components and classification of biosensor. Adapted from [25] and [26].

2.2.1 Optical biosensors

Optical biosensors perform analysis through the measurement of photons, using optic fibers and transduction elements [22]. Optical detection can be based on absorption, reflection, refraction, dispersion, infrared, Raman scattering, chemiluminescence, fluorescence, and phosphorescence [26]. The optical biosensors most discussed in the literature are fluorescence-based biosensors, surface enhanced raman spectroscopy (SERS)-based biosensors, grating and photonic crystal (PC) biosensors, guided mode resonance (GMR) based biosensors, and plasmon-based biosensors [27].

Fluorescence based biosensors detect fluorescent emission caused by electromagnetic radiation absorption by fluorophores or fluorescently labeled molecules. A fluorescence biosensor is composed of an excitation light source (typically light-emitting diodes and lasers), fluorophore molecules that label target biomolecules, and a photodetector that records the fluorescence intensity and spectrum. The fluorophore molecules used can be small molecules, proteins, or quantum dots that label proteins, nucleic acids, or lipids [27]. Fluorescent based methods are the most commonly used in the field of optical biosensors. This methodology is very efficient because it combines the high sensitivity of fluorescence detection, with the high selectivity provided by specific molecular recognition elements [28].

Surface-enhanced Raman spectroscopy (SERS) is based on Raman scattering resulting from inelastic process. This phenomenon happens when the kinetic energy of the incident photons is increased or decreased by interacting with molecular vibrations or rotations, phonons, or other excitations. Since, typically, spontaneous (normal) Raman scattering is very weak, enhancement by molecules adsorbed on a specific medium or interface is needed to improve the sensitivity. Two main mechanisms are responsible for this enhancement: an electromagnetic mechanism and a chemical mechanism [27].On one hand, the chemical mechanism contributes to enhancement through chemisorption of the molecule to the noble metal surface, allowing the electrons from the molecule to interact with the electrons from the metal surface. On the other hand, the electromagnetic mechanism is a wavelength dependent effect arising from the excitation of the localized surface plasmon resonance (LSPR). Plasmon resonance is the collective oscillation of conduction electrons that can occur in noble metal nanoparticles (NPs), sharp metal tips, or roughened metal surfaces, enhancing the incident electrical field intensity. SERS detection can be performed both in intrinsic and extrinsic formats by evaluating the Raman signature. In intrinsic SERS biosensing, this signature is directly obtained from the analyte of interest, such as a small molecule, DNA strand, or protein. In extrinsic SERS, the analyte or interaction of interest is associated with a molecule with an intense and distinguishable Raman signature, and it is, therefore, obtained indirectly. SERS detection has gained attention of reserachers because of its high sensitivity, the "fingerprinting" ability to produce distinct spectra from molecules similar in structure and function, and the fact that water has a very small Raman scattering cross-section, which leads to minimal background signal from aqueous samples [29].

Photonic Crystals (PCs) can be considered as a periodic arrangement of regularly shaped materials with different dielectric constants. The periodicity can vary from one dimensional to three dimensional. They have distinct wavelengths of reflection that are governed by the distance between the layers. Thus, when this periodicity is changed due to, for example, a biochemical stimulus, the wavelength of maximum reflectance also will change and sensing is possible. Advantages of this detection method include low cost and easy handling. Furthermore, the result can be amenable to visual readout by unskilled operators [30].

A guided mode ressonant (GMR) grating can be defined as a thin waveguiding film in optical contact, or merged, with a grating. The waveguiding film operates usually by having a higher refractive index than its surrounding media (the cladding), and, because of its thin dimension, supports a discrete number of guided modes [31]. The resonant peak (that can be evaluated in reflectance or transmittance) is highly sensitive to the changes in surrounding refractive index, allowing to determine target analytes and the corresponding concentrations [32].

Surface plasmon resonance (SPR) is a technique based on the opto-electronic phenomenon that occurs when a visible or near-infrared light is incident upon a metal surface, such as Ag, Au, Cu, and Al. When the frequency of the incident light is equal to the resonant frequency of the metal, an energy transfer from the photons of the light to the surface electrons of the metal takes place. Consequently, the electrons move and generate

an electrical wave called plasmon. This surface plasmon ressonance phenomenon takes place at an specific light frequency and a specific incidence angle. Furthermore, it is highly dependent on the refractive index close to the metal surface that changes with the mass on the chip surface. This dependency makes SPR-based devices suitable for sensing because the binding of biomolecules, within the range of the electric field, changes the mass on the chip surface and it perturbs the plasmon changing the resonance wavelength. Localized plasmon resonance-based methods use a surface composed of nanomaterial with a dimension smaller than the wavelength of light, allowing the evaluation of local changes in the refractive index due to molecule binding events. Plasmon resonance-based techniques hold the advantage of being labelfree and real-time methodologies. Additionally, they present high sensitivity, rapidity, and cost-effectiveness while retaining the conformational and functional integrality of biomolecules to be investigated [28].

2.2.2 Electrochemical biosensors

The operation principle of electrochemical sensors is the reaction with the analyte of interest to produce an electrical signal proportional to the analyte concentration. A typical exemple of electrochemical sensor is a sensing electrode (working electrode) and a reference electrode separated by an electrolyte but, for most applications, a three electrode system is applied with the reference connected to a high-input-impedance potentiostat and a counterelectrode is used to complete the circuit for current flow. This detection method is very attractive because of its relative simplicity. It is possible to produce easy-to-use portable rapid detection systems because inexpensive electrodes can be easily integrated with simple electronics. Furthermore the emergence of new nanomaterials such as carbon nanotubes and graphene and its applications in electrochemical biosensing is lowering the limit of detection (LoD) to unparalleled levels, leading to important breakthroughs and new biosensing applications [33]. Several techniques can be used for electrochemical biosensing:.

- **Amperometric:** measuring currents due to the reduction or oxidation of electroactive species. Amperometric biosensors transduce the biological recognition events caused by electroactive species at the sensing surface into a current signal for the quantification of an analyte within a sample matrix. Typically, two electrodes are separated by an electrolyte solution and the measured current is linearly correlated to the concentration of the analyte. The simplicity of the working principle led to the development of low-cost portable devices for several applications ranging from disease diagnosis to environmental monitoring. A well known example monitoring of glucose levels by people with diabetes, where a test can be made within minutes using a small droplet of blood extracted by pricking a finger with a small needle [33].

- **Impedometric**: measuring the impedance of the system upon immobilisation of biolayers at the electrode surface. Impedometric biosensors typically use electrochemical impedance spectroscopy (EIS), where the impedance is measured over a wide range of AC potential frequencies (typically from 100 kHz to 1 mHz). EIS provides a frequency-domain response linked to the physico-chemical changes that take place when an analyte binds to a bioreceptor immobilised on an electrode. This technique can be divided into two categories: : Faradaic and non-Faradaic EIS.

The first one uses redox probes and the main analysis is focused on charge transfer resistance changes generated by the obstructing presence of the analyte when it binds to the surface. The second one exploits charging currents, without the use of redox probes, and the analysis is mostly based on the electrochemical double layer capacitance changes upon target binding [33]. Improved binding strategies and surface optimisation have allowed very low limits of detection, reaching protein detection down to attomolar (aM) concentrations [34].

- **Potentiometric:** measuring variations in open circuit potential. Potentiometric biosensors measure the electrical potential between working and reference electrode, using a high impedance voltmeter. Potentiometric sensors are usually applied for measuring metal ions, toxins, carbohydrates. Recently, these sensors have been improved by functionalizing the electrode to allow biomolecules binding and the application of aptamer is a breakthrough among functionalization strategies [35]. Furthermore, biologically sensitive field-effect transistors (BioFETs) are a special type of potentiometric biosensors, offering remarkable sensitivity to detect biomolecular binding events or metabolic reactions at the interface of living systems and electronics [36].

2.2.3 Mass-based biosensors

Mass-based detection, or gravimetric detection, offers direct label-free analysis with increased specificity and sensitivity. The transduction is based on resonance phenomenon that allows sensing the small changes in mass. This phenomenon can be measured by various parameters such as frequency, amplitude and phase. Mass-based biosensors are cost-effective and relatively easy to operate. These biosensors can be further classified into piezoelectric and magnetoelastic biosensors [25].

Piezoelectricity refers to the ability of certain materials to generate an electric charge in response to applied mechanical stress. Piezoelectric biosensors use piezoelectric crystals that are made to vibrate at a specific frequency with the application of a time modulated electrical signal. Thus, the frequency of oscillation is dependent on the applied electrical frequency to the crystal as well as the mass of the crystal. When the mass increases, by the binding of chemicals, for example, the frequency of oscillation of the crystal changes. This change can be measured electrically and used to determine the additional mass of the crystal.

Magnetoelastic (ME) biosensors are based on based on the Joule magnetostriction of magnetic materials, which can vibrate longitudinally at a characteristic frequency, depending on physical parameters of the materials, when subject to a time varying magnetic field. When the testing temperature, humidity and other environmental parameters are constant, the resonance frequency change of the magnetoelastic sensor depends only on the mass change on its surface. Recently, ME biosensors have emerged as an interesting acoustic-wave transducers for development of high-sensitive biosensors. The main competitive advantage of these sensors is that they are wireless, namely there is no physical connection between the detection electronics and the sensor [37].

2.3 Porous silicon: fundamentals and biosensing

As previously discussed, biosensors transduction methods can rely on different mechanisms. Nevertheless, optical transducers outperform most physical transducers as there is no influence of the nature of the sample or of external disturbances on the signal [5]. Furthermore, optical biosensors offer significant advantages over electrochemical and mass-based techniques and other types of sensors for multi-target sensing and continuous monitoring [38].

Over the past decades, porous silicon (PSi) has emerged as a promising nanomaterial for label-free optical biosensing applications as its optical properties, i.e., photoluminescence (PL) and reflectance, are highly sensitive to the presence of chemical and biological species inside the pores [38]. Moreover, PSi presents unique and tunable photonic properties allowing for label-free biosensing. Its fabrication process is relatively simple and cost-effective, and its high internal surface (up to 800 m^2g^{-1}) [39], results in a large area for hosting biological molecules and interactions. The surface of the pores is also reactive and can be easily functionalized with chemical and biological molecules by well-established surface chemistries. All those characteristics place PSi as a superior alternative to other planar photonic biosensors for many applications [39].

Hence, PSi fundamentals, fabrication process, and working principle of the optical photonic structure-based biosensing will be further discussed in the following sections. Special attention will be given to PSi membranes because they have been found to increase both the response time and amplitude of the sensors [5].

2.3.1 Fabrication process

Porous silicon is generated by electrochemically etching crystalline silicon in aqueous or non-aqueous electrolytes containing hydrofluoric acid (HF). Even if chemical dissolution of silicon in aqueous HF solution is thermodynamically feasible, this reaction is very slow unless strong oxidizing agents (such as O^2 or NO^{3-}) are present in the solution, or unless the oxidation reaction is driven by electrochemistry. The reason for this time-consuming procedure is the presence of surface hydrides that passivates the surface and limits the corrosion kinetically. Once the silicon is chemically or electrochemically etched in HF-containing solutions, the exposed silicon surface becomes terminated with H atoms, as shown in figure 2.7, residual oxides or fluorides are removed by the HF electrolyte [40].

In order to perform electrochemical etching, two electrodes are needed. Therefore, two reactions occur simultaneously in an electrochemical cell, the anode (oxidation) reaction and the cathode (reduction) reaction. The two-electrode cell is shown in figure 2.8, where the working electrode (silicon) is the anode and the cathode counter-electrode is typically platinum [40]. The etching cells are fabricated in HF-resistant materials, like Teflon® or polyether ether ketone (PEEK) [41].

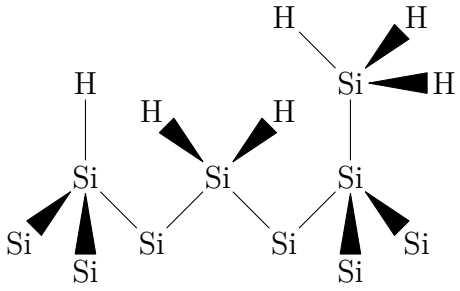

Figure 2.7: Hydrides on the porous silicon surface. Three types of surface hydrides are depicted: SiH, SiH_2, and SiH_3. Adapted from [40].

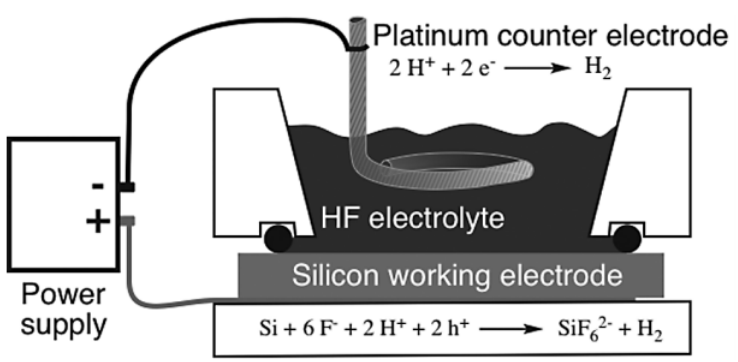

Figure 2.8: Schematic of a two-electrode electrochemical cell used to make porous silicon with the main oxidation and reduction half-reactions occurring during the formation of porous silicon. Extracted from [40].

Within the electrochemical process, two regimes can be observed: pore formation and electropolishing, as shown in figure 2.9. It can be seen, that the holes reaching the pore tips weaken the Si-H surface bonds and allow the dissolution of the silicon. By increasing the current density, the pore walls become thinner, until the pores merge in the electropolishing regime. When analysing the current–potential curve for silicon in an HF electrolyte, one can see that, at the beginning, the current increases exponentially with the potential until reaching a maximum. Then, it decreases somewhat and, afterwards, it increases more slowly with increasing potential, as seen in figure 2.10 [40]. The transition between the two regimes, each one governed by a different equation as also shown in 2.10, depends on the substrate's properties, like doping or crystalline orientation, and the fabrication parameters, such as electrolyte concentration and temperature, but is mostly governed by the ratio between the applied current density and the concentration of fluorine ions [41]. Although some roughening can occur, electropolishing generally removes silicon atoms uniformly, and a smooth, polished surface will result [40].

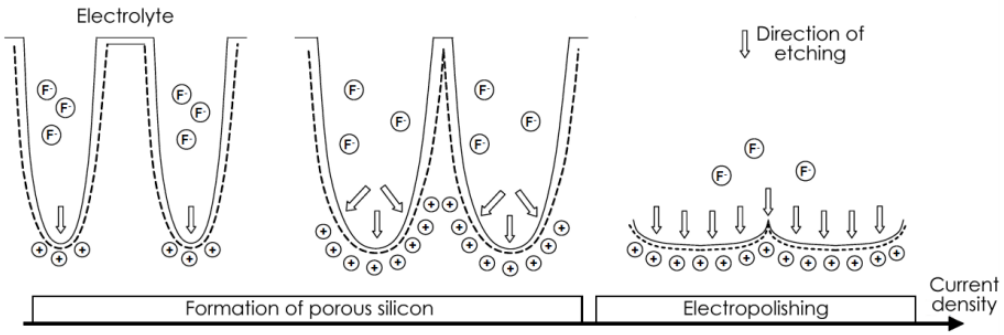

Figure 2.9: Mechanism of pore formation with increasing current densities. Extracted from [42].

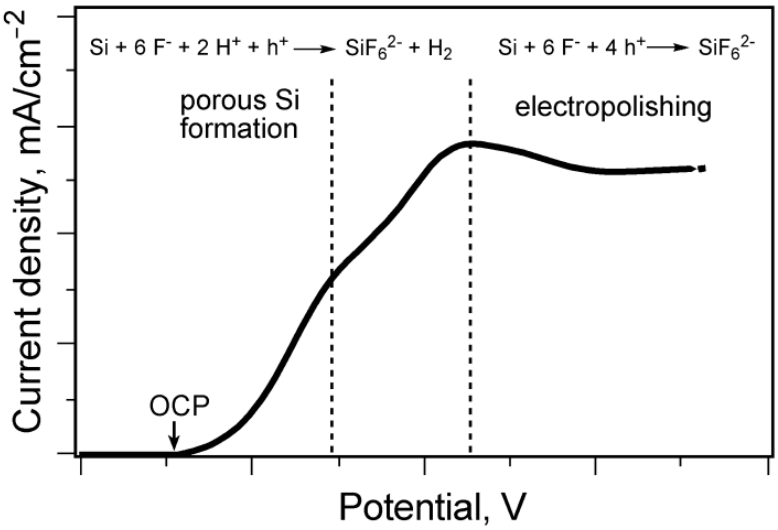

Figure 2.10: General current density versus applied potential curve for electrochemical etch of silicon in an HF electrolyte, showing the regimes for porous silicon formation and for electropolishing. "OCP" indicates the open circuit potential, or rest potential, of the silicon electrode. Extracted from [40].

The process behind pore formation in porous silicon is influenced by combination of multiple parameters, such as electrolyte composition, dopant type and concentration, applied voltage, temperature, and light intensity [40]. No complete understanding of the mechanisms that determine PSi morphology exists because the Si porosification is a very complicated process, which depends on a great number of parameters involved [43]. Nevertheless, some general trends are observed during the porosification process as summarized in table 2.2.

Table 2.2: Effect of Anodization Parameters on PSi Formation. Extracted from [44].

	Parameters		
An increase of	**Porosity**	**Etching rate**	**Critical current**
HF concentration	Decreases	Decreases	Increases
Current density	Increases	Increases	-
Anodization time	Increases	Almost constant	-
Temperature	-	-	Increases
Wafer doping (p-type)	Decreases	Increases	Increases
Wafer doping (n-type)	Increases	Increases	-

Furthermore, there are some common features between the different possible experiments [40]:

- pores nucleate uniformly with no particular order on the silicon surface, except in the case where the wafer has been specifically pre-patterned;
- current flows preferentially near the pores bottom;
- the pore walls tend to become passivated, which leads to primary dissolution of silicon at the porous silicon/crystalline silicon substrate interface;
- after their formation, pores do not reconstruct nor redistribute;
- the resulting samples have a pore diameter distribution rather than a single pore size.

2.3.2 Morphology

The morphology of PSi samples is characterized by three key features: pore size, layer depth and porosity [3]. As previously mentioned, different parameters play a role in pore formation and, therefore, the structure and morphology of PSi is highly dependent on the choice of those.

The first important parameter is the pore size. Generally, PSi is classified based on the diameters of its pores defined according to the International Union of Pure and Applied Chemistry (IUPAC) [45]:

- micropores: $d < 2\ nm$
- mesopores: $2 < d < 50\ nm$
- macropores: $d > 50\ nm$

Generally, n-type wafers tend to give macropores, highly doped p+ , p++ , or n+ give mesopores, and p- type silicon yields meso- to micro- pores [40]. Current density has a main influence on the pore size and growth rate. As shown in figure 2.11, larger pores are formed at higher current densities. Furthermore, due to the increased growth rate, an increased current density leads to an increased layer thickness for the same anodization time [3].

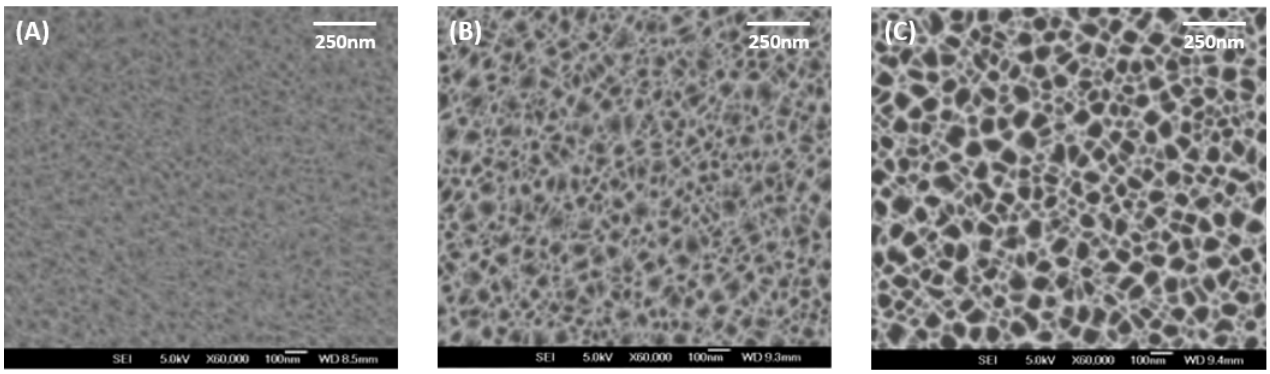

Figure 2.11: Top-view SEM images of the dependence of pore diameter and morphology on applied current density: (A) 5, (B) 15, (C) 25 mA/cm^2. Samples anodized from a 0.010–0.018 $\Omega cmn - typeSi. Adapted from$[46].

The second feature is the pore depth, or layer thickness, is directly correlated to the etching time. Longer etching times will lead to thicker layers. Indeed, if the etching time is doubled, for a same current density, the porous layer thickness will also be multiplied by two. However, for large depths, the HF concentration might be compromised, due to diffusion limitations, inducing a change in the growth rate that will affect the direct relation between etching time and layer depth [3].

Porosity is the third morphological feature and is defined by the IUPAC as "the ratio of the total pore volume V_p to the apparent volume V". A distinction must be done between open porosity, closed porosity and total porosity:

- open porosity: the volume of pores accessible to a given probe molecule;
- closed porosity:the volume of pores inaccessible to a given probe molecule;
- total porosity: *open porosity + closed porosity*; the volume of pores accessible to a given probe molecule plus the volume of pores that are inaccessible to the probe.

Since porous silicon is prepared by the corrosion of solid crystalline silicon, all the pores in a freshly etched PSi sample are part of an open-porous material with no inaccessible pores. However, post-processing techniques such as surface passivation may lead to the closure of some pore mouths and the material will contain closed porosity [40]. This is an important notion for biosensing applications because the pores of the PSi layer might not be large enough to accommodate the biomolecule of interest, thus part of the porosity is not usable [3]. Furthermore, the passivation treatments developed in this work (see Chapter 3), might induce a decrease in open porosity.

Transitional layer

At the beginning of the anodization process, a transitional layer is obtained.This is a thin but very dense layer of PSi exhibiting very small pore openings (< 10 nm) and a low porosity. This layer prevents the penetration of large molecules due to the small pore size, compromising the formation of the expected regular PSi layer, whose pore diameter and

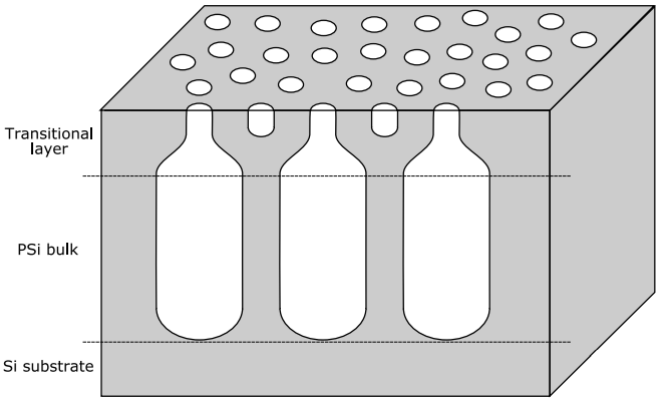

Figure 2.12: Schematic of the pore morphology: after nucleation, some of the pores do not grow into the bulk, while the rest grows both in diameter and in length, leading to the formation of a dense transitional layer on top of the more homogeneous PSi bulk layer. Extracted from [3].

porosity are directly linked to the current density [3]. The expected pore morphology is shown in figure 2.12.

Due to the mentioned reasons, the presence of the transitional layer is undesirable. Therefore, it needs to be removed to ensure an homogeneous PSi layer. The most used method in the literature consists in electrochemically etching at a high current density a first layer of PSi, called sacrificial layer, then removing it by wet etching using a base solution, usually KOH or NaOH [3].

2.3.3 Porous silicon characterization

As previously discussed, the three most important morphological characteristics of a porous silicon film are thickness, porosity and pore size. These features can be characterized using different techniques.

Pore size, morphology and sample thickness can be evaluated through electron microscopy (transmission electron microscopy and the various scanning electron microscopies) and scanned probe techniques (atomic force microscopy and scanning tunneling microscopy). For example, scanning electron microscopy (SEM) top-view images allow the measurement of pore size and, with the aid of an image analysis routine, porosity can be estimated for the surface layer. Furthermore, by breaking a wafer to obtain a cross-section, one can use SEM imaging to measure the porous layer thickness.

Another technique which allows the characterization of both the porosity and thickness is the spectroscopic liquid infiltration method (SLIM). This is a non-destructive optical characterization method, as described in the following section.

Spectroscopic liquid infiltration method (SLIM)

Smooth, reflecting porous silicon films display an optical interference pattern (Fabry–Pérot fringes) arising from constructive and destructive interference of light from the top and

bottom of the porous layer. To observe this effect, a flat and smooth layer is needed, with no pores or other features larger than 500 nm. Furthermore, the pore dimensions in the layer must be significantly smaller than the wavelength of light [40].

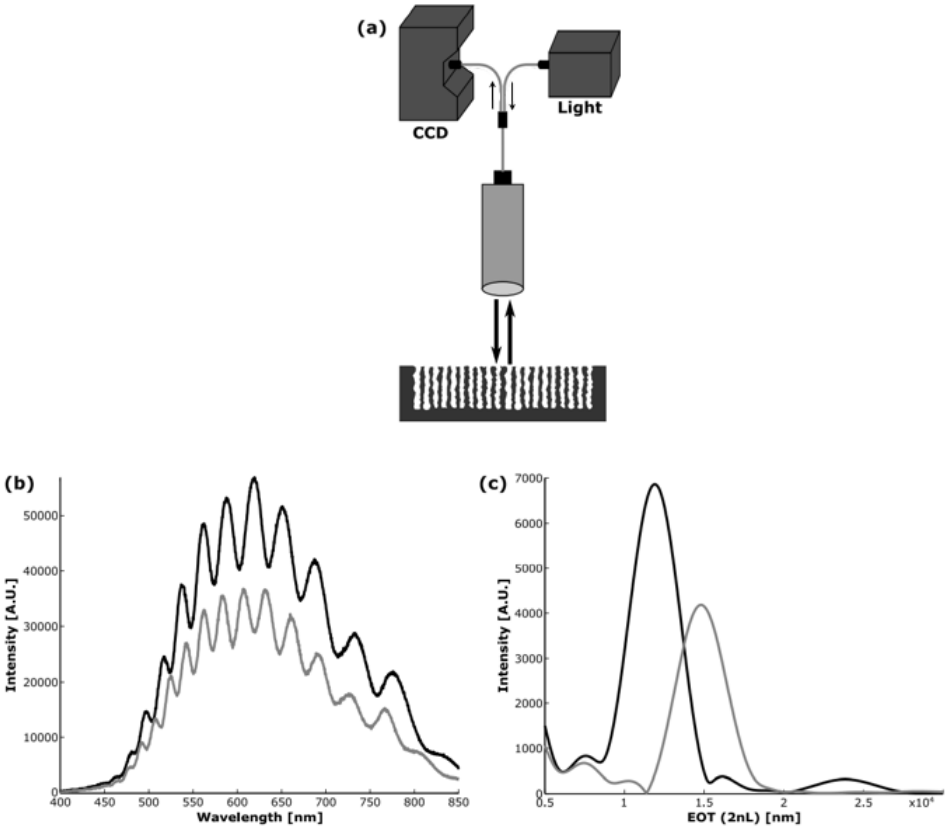

Figure 2.13: Schematic of the working principle of SLIM using white light reflectance interferometry. (a) White light from a halogen light source passes through a bifurcated optic fiber and is focused on the surface of PSi in the normal direction using bi-convex lenses. The light is reflected back from the two interfaces through the lenses and optic fiber towards the CCD spectrophotometer. (b) Reflectance spectra showing interference fringes resulting from the double reflection at the interfaces, the black and grey traces are the spectra for PSi in air and ethanol, respectively. (c) Fourier transforms of the reflectance spectra from (b) resulting in a peak whose position corresponds to the effective optical thickness, 2nL [3]. Extracted from [3].

The SLIM method relies on the acquisition of the sample's reflectance spectrum in the visible light range at an incidence normal to the PSi surface using a CCD spectrophotometer, as shown in figure 2.13.a. The reflectance spectrum is acquired two times at the exact same spot, each time under a different media of known refractive index filling the pores. Usually the first spectrum is acquired in air, while the second is acquired in presence of a solvent. The obtained optical interference pattern exhibiting Fabry–Pérot fringes, shown in figure 2.13.b. is submitted to a Fourier transform operation, shown in figure 2.13.c. The corresponding frequency spectrum, exhibits a frequency peak whose position is equal to the effective optical thickness (EOT) $2nL$ of the associated filling medium/porous layer

complex, with n being the average refractive index of the filled porous layer and L the thickness of the porous layer. Finally, the $2nL$ values of the PSi layer can be inserted in the Bruggeman effective medium model to predict the porosity and thickness of porous silicon, fully described by Ref. [40].

If the porous silicon film is composed of more than one layer, the FFT yields values of $2nL$ for the separate layers as distinct peaks. For a double - layer structure (see section 2.3.4), for example, the FFT spectrum will display three peaks, corresponding to the values of 2 nL for layers 1, 2, and 3, respectively, as schematically shown in figure 2.14 [40].

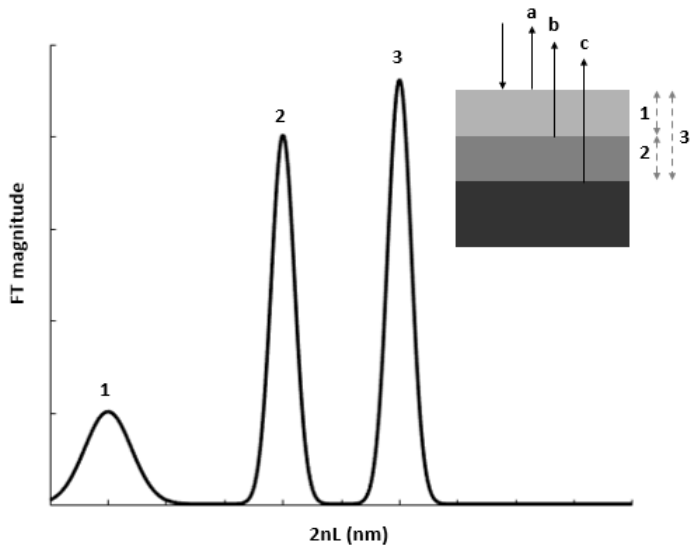

Figure 2.14: Fourier transform of the reflected light spectrum of a double - layer structure, shown schematically in the inset. The number assigned to each peak corresponds to the layer indicated in the inset. Adapted from [40]

2.3.4 Porous silicon nanostructures

By changing the applied current during the etch, it is possible to modulate the porosity and pore size of the PSi layer through its depth. Indeed, these morphological characteristics at any instantaneous point in time during an etch are a direct map of the current density. Therefore by controlling the current-time relationship, it is possible to control the porosity-depth relationship in the layer [40].

To this point, only single PSi layer was mentioned, but it is possible to achieve PSi multilayered structures. The different structures will provide a particular optical reflectance spectrum as measured using the setup shown in figure 2.13.a. The current waveforms required to form some of these structures are displayed in figure 2.15 along with the corresponding optical reflectance spectra and schematic 2D models.

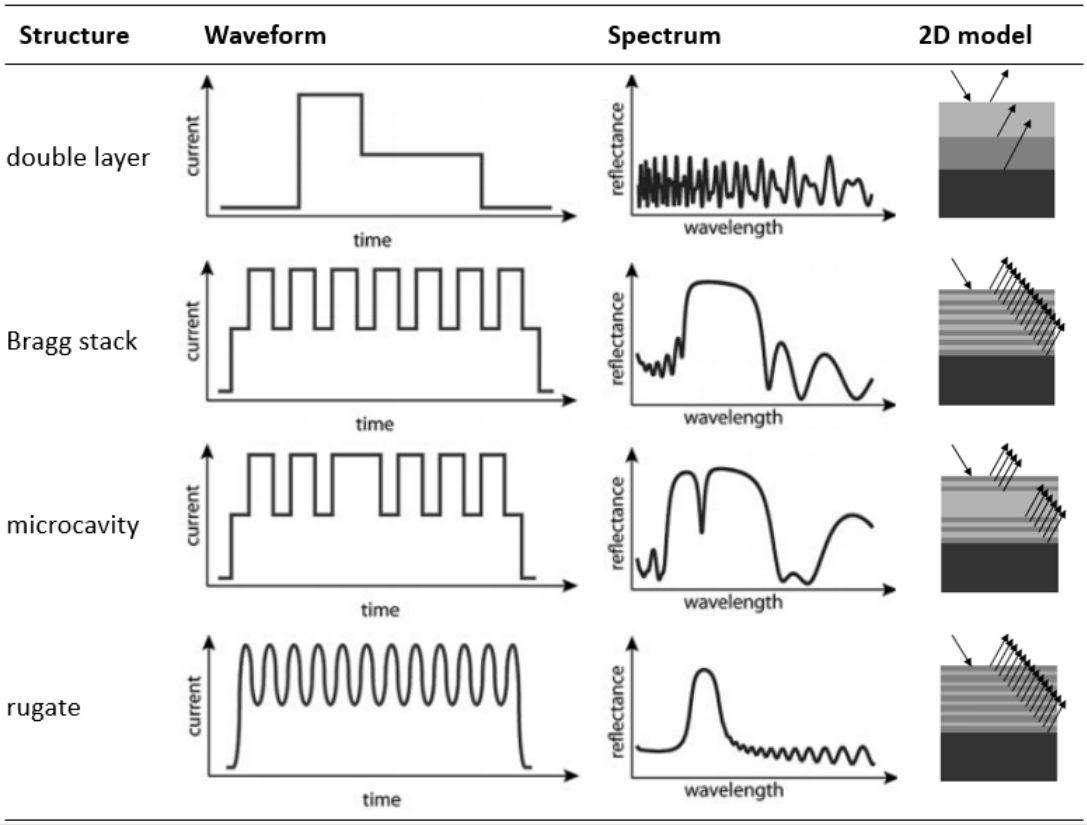

Figure 2.15: Current density waveforms used for the fabrication of PSi optical structures, their corresponding reflectance spectra, and multilayer 2D models (the bottom part represents the Si bulk, dark gray and light gray layers correspond to layers of low porosity and high porosity, respectively; arrows represent the incident light and the light specularly reflected at each interface. Adapted from [40] and [47].

The simplest structure is the single-layer PSi interferometer. Light reflecting off the top and bottom interfaces of the PSi film interfere, giving rise to characteristic Fabry−Pérot fringes. Constructive interference leading to the reflection peaks occur when the condition indicated in equation 2.1 is satisfied [39]:

$$\frac{2nL}{cos\theta} = m\lambda_0 \qquad \text{(Single layer interferometer)} \tag{2.1}$$

where n is the refractive index of the PSi film, L is the physical thickness of the porous layer, θ is the angle of incident light, m is an integer, and λ_0 is the vacuum wavelength of light.

Another structure that can be prepared is the PSi double-layer: a layer of high porosity and large pores on top of another layer of lower porosity and smaller pores [3]. This is achieved by changing the current from a higher to a lower value at some point during the etch. Such structures can be used as size exclusion matrices, to separate biomolecules [40], making them particularly interesting for biosensing applications.

Multilayer PSi films, including Bragg mirrors, microcavities, and rugate filters, can also be fabricated. The optical properties of these structures are similarly dictated by thin film interference phenomena. Bragg mirrors (or Bragg stacks) are designed with alternating layers of high and low refractive index (low and high porosity, respectively). All layers have the same EOT, corresponding to one-quarter of the target wavelength to be reflected by the mirror, as specified in equation 2.2. A high reflectance centered in the target wavelength is observed through a relatively broad range, called the stop-band [39].

$$L_{mirror} = \frac{\lambda_0}{4n} \qquad \text{(Bragg mirror)} \tag{2.2}$$

The width of the stop-band depends on the refractive index contrast between the layers, the higher the contrast, the wider the stop-band. Furthermore, the maximum reflectance of the stop-band is linked to the number of stacked layers, the higher the number of layers, the higher the maximum reflectance value. This is an interesting structure for biosensing applications because the stop-band shifts when molecules infiltrate the PSi multilayer stack and increase the effective refractive index of the PSi layers.

However, it is easier to monitor the shift of a sharper feature, the PSi microcavity and PSi rugate filter are more commonly employed for sensing applications compared to the Bragg mirror. The microcavity structure will exhibit a narrow resonance. This feature is created by inserting a PSi cavity layer with an EOT corresponding to one-half of the resonance wavelength (or an integer multiple of $\lambda_0/2n$) between two PSi Bragg mirror stacks, as specified in equation 2.3 [39].

$$L_{cavity} = \frac{\lambda_0}{2n} \qquad \text{(Microcavity)} \tag{2.3}$$

The rugate filter achieves e a narrow-width and a high contrast reflectance peak by varying the refractive index in a smooth, sinusoidal fashion, as described in equation 2.4, where x indicates the direction normal to the PSi multilayer surface, n_0 is the average refractive index of the PSi layers, Δn is the refractive index contrast, and λ_0 is the wavelength of the reflectance peak. In order to do so, a sinusoidal current waveform is delivered to the silicon wafer. The width of the reflectance peak increases with Δn, and the peak height increases with the number of periods (*i.e.,* number of repetitions of the sinusoidally varying refractive index profile). Therefore, a rugate filter with a small Δn and many periods is desirable [39].

$$n(x) = n_0 + \frac{\Delta n}{2} \sin\left(\frac{4\pi x}{\lambda_0}\right) \quad \text{(Rugate filter)} \tag{2.4}$$

2.3.5 PSi-based optical biosensors

Porous silicon optical devices are widely used to detect different biomolecules (*i.e.*, DNA, enzymes, cells, bacteria, antigen) [4]. PSi-based optical biosensors can be separated in two main categories based on their transduction methods: photoluminescence and reflectance. Many optical biosensing schemes based on porous silicon have been proposed. A full overview on the most recent techniques is summarized in Ref. [4], but a few examples will be given in the following sessions to illustrate the discussed working principles.

Photoluminescence

One important milestone in porous silicon history happened in 1990, when Leigh Canham discovered that PSi could emit efficient tunable visible photoluminescence (PL) at room temperature and attributed this effect to quantum-size effects in crystalline silicon [48]. The photoluminescent properties of PSi may be used for sensing and biosensing by exciting a sample and directly looking for the PL spectrum of the analyte or by indirectly observing changes in the PL of PSi as affected by the analyte [38]. A scheme of the optical setup for PL measurements is shown in figure 2.16.a. The detection scheme for PL-based biosensors can be based: (i) on the quench of the PL emissions, or (ii) on the shift of the PL spectra, upon exposure to the analyte [38].

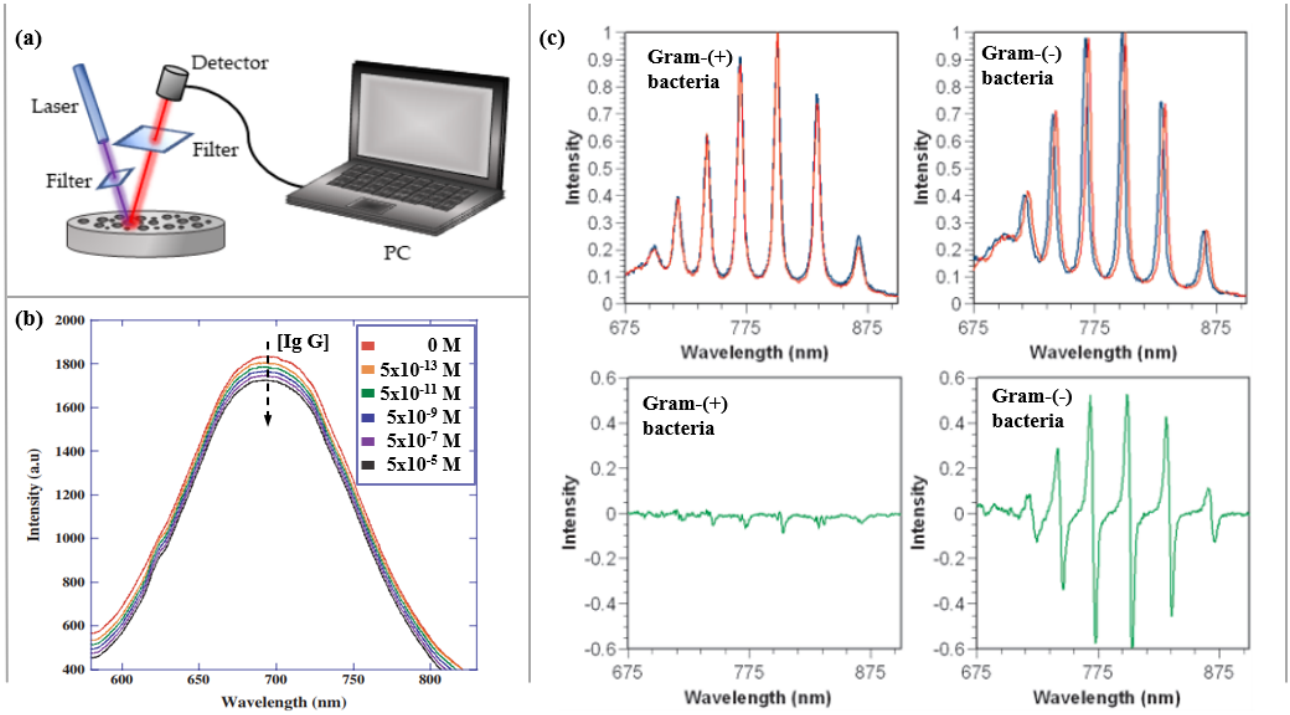

Figure 2.16: PL-based porous silicon biosensing. (a) Optical setup for photoluminescence spectroscopy, extracted from [4]; (b) quenching of PL spectra of protein A-functionalized PSi with human Ig G, adapted from [49]; (c) shift of PL spectra of PSi microcavity functionalized with bacteria lipid A-binding receptor (from blue to red) upon introduction of cell lysates: from Gram-(+) bacteria (*B. subtilis*, left) or Gram-(-) bacteria (*E. coli*, right), green spectra are the difference between spectra obtained in the presence and absence of bacterial cell lysates, adapted from [50].

The quenching of the PL may be due to binding of the molecule (*i.e.,* DNA, protein, enzyme, antibody) to the surface of the PSi nanostructure which can introduce a site for non-radiative recombination of excitons, interfacial charge, energy transfer, or modification of the dielectric constant of the surrounding medium [38]. For example, a photoluminescent porous silicon (PSi) interferometer modified with protein A was proposed for the detection of Human Immunoglobin G (Ig G). As displayed in figure 2.16.b. decrease of PL was

observed upon addition of human Ig G and a detection limit of 500 fM was obtained [49].

The second method measures the shift of the PL spectrum after binding of the target analyte. A biosensor based on a PSi microcavity (surrounded by two Bragg mirrors) was able to confine the emission of PL, creating a resonating structure resulting in sharp peaks whose position can be easily monitored [50]. This biosensor was functionalized with a highly selective bacteria lipid A-binding receptor, and achieved the selective detection of Gram-(-) bacteria. The PL spectra from Gram-(+) and Gram-(-) bacteria is shown in figure 2.16.c. and a shift is only observed for the latter, confirming the selectivity of the device.

Unfortunately, there is a greater error associated with measuring photoluminescence intensity changes when compared to sensors relying on reflectance-based interferometry. That is the main reason why PL-based biosensors are comparatively less studied [38].

Reflectance

Biosensors based on white light reflectance measurements have been widely used for the detection of different analytes, *e.g.* small molecules, DNA, proteins, enzyme activity, bacteria and mammalian cells [38]. The simplest scheme relies on perpendicular illumination of a PSi film with white light. Reflectance interference fringes are observed in the visible and near infrared, and, upon the application of a Fourier transform, the fringe maxima are determined by the effective optical thickness (EOT) of the film ($EOT = 2nL$), as shown in figure 2.17. This method was described as the Reflective Interferometric Fourier Transform Spectroscopy [51] and is similar to the procedure adopted for the SLIM method, as described in section 2.3.3. The detection is based on the increase of the refractive index when the analyte is present inside the porous matrix, producing a shift of the reflectivity spectrum to longer wavelengths (red-shift) [4].

The detection of large sized biomolecules has been achieved by using a mesoporous PSi optical biosensor funtionalized with anti-heat shock protein 70 (HSP70) antibody. The detection of HSP70 was achieved, also using the RIFTS method, through the immobilization of the antibody via 3-aminopropyltriethoxysilane (APTES)/glutaraldehyde linking chemistry, as schematically shown in figure 2.18, and a limit of detection of 1290 μg/mL was achieved. The monitoring of HSP70 levels could be useful for the early detection of this pathological condition [52].

A biosensing platform for label-free detection of bovine mastitis (BM) onset, a inflammatory disease affecting the dairy industry worldwide, has been successfully fabricated. A porous silicon Fabry−Pérot interferometer was functionalized with gelatin to specifically target N-acetyl β-D-glucosaminidase (NAGase) which has its concentration in milk influenced by two dominant BM causative pathogens (i.e., *Escherichia coli* and *Streptococcus dysgalactiae*). The presence of NAGase was monitored through the RIFTS technique, as shown in figure 2.19 and the detection limit obtained was 0.51 μM/min [53].

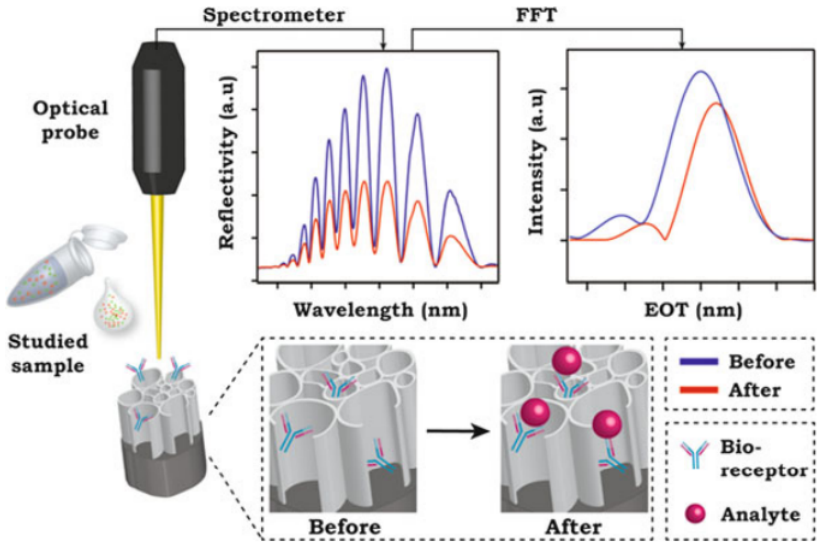

Figure 2.17: A schematic illustration of the PSi nanostructure-sensing concept. The PSi nanostructure physically separates a variety of target analytes and specific detection is facilitated by the incorporation of capture probes on the surface. Whole cells and microorganisms are excluded from the pores and may be immobilized onto the PSi surface, while moderate- and small-size molecules are captured within the pores. Extracted from [38].

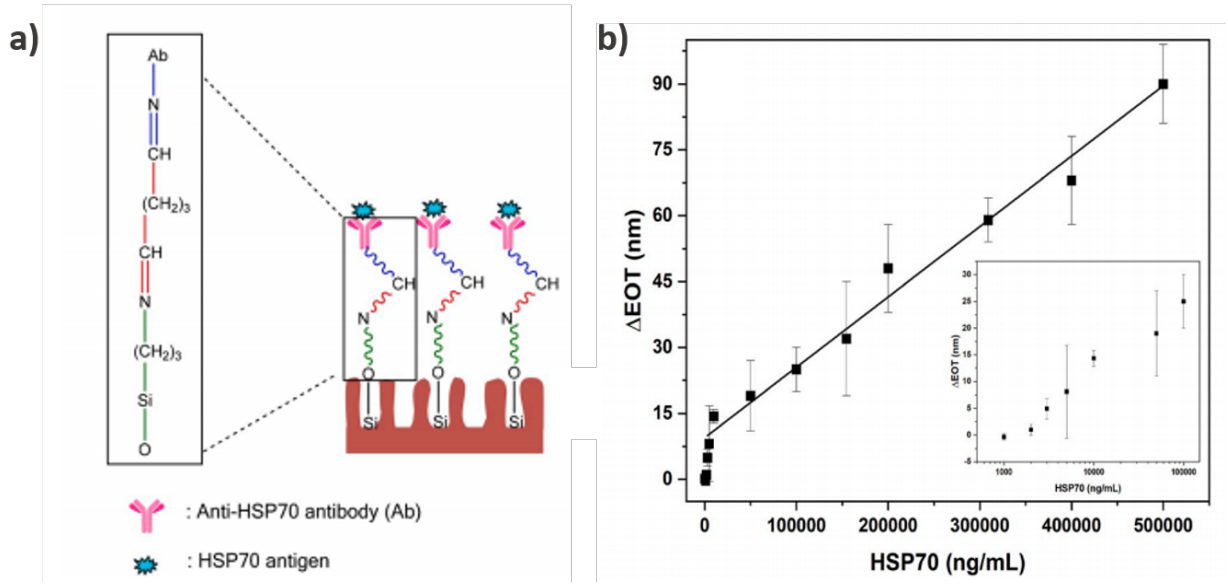

Figure 2.18: (a) Schematic representation of the label-free PSi optical biosensor surface functionalization: the oxidized surface is functionalized with APTES and GI, followed by immobilization of anti-HSP70 antibody and detection of HSP70 antigen. (b) Relationship between the concentration of HSP70 antigen and EOT shift (inset semi-log plot). Extracted from [52].

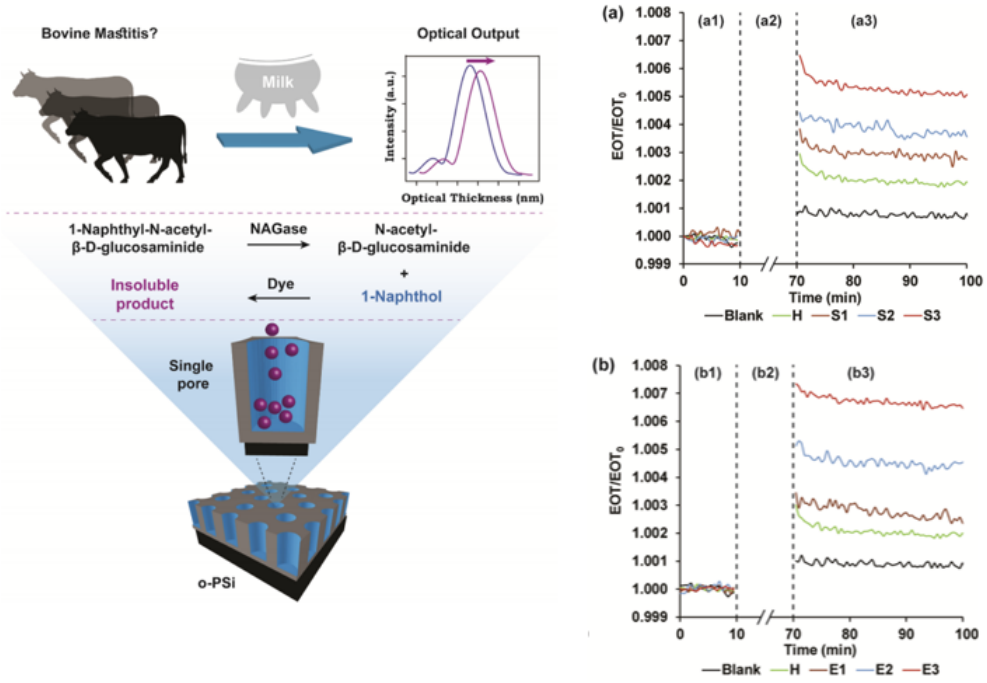

Figure 2.19: (Left): schematic representation of the gelatin-functionalized PSi biosensor for the NGAse activity detection. (a) Reflective-based response of NGAse catalytic activity in milk samples positive to *S. dysgalactiae* and (b) *E. coli*. The lines (a1, b1) are the baseline, the reaction solution and the dye are represented by lines (a2, b2) while the buffer wash is represented by lines (a3, b3). Adapted from [53].

2.3.6 PSi membranes

Porous silicon membranes (PSiMs) are formed by detaching the porous layer from the underlying bulk silicon substrate. By doing so, the pores become open-ended channels and flow-through applications are possible. There are several techniques that have been proposed to fabricate porous silicon membranes but they can be divided in two main categories: the ones relying on electrochemical etching for porosification and the ones relying only on other microfabrication techniques, as summarized in figure 2.20. Electrochemically etched porous silicon membranes can be achieve through four different routes [41]:

- **Through wafer:** anodization through an entire wafer of standard thickness [54];
- **Free-standing:** anodization of part of the silicon wafer and "lift-off" of the porous matrix by, for example, electropolishing a small cavity below the porous region [55];
- **Self-supported:** microfabrication techniques are used to create cavities before or after anodization [5];
- **Lateral:** pores parallel to the substrate surface are created through anodization and microfabrication techniques [56].

Highly controlled pore geometry can be achieved for membranes relying only on microfabrication techniques, without the use of electrochemical etching. A distinction can be made between three types of non-anodised porous membranes [41]:

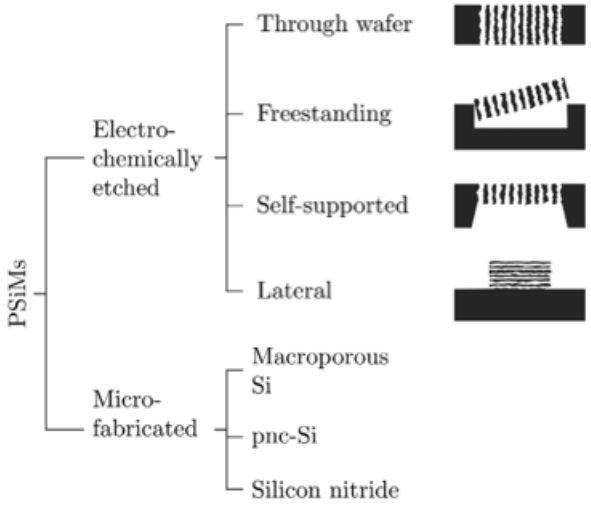

Figure 2.20: Summary of porous membranes fabrication techniques. Adapted from [41].

- **Macroporous silicon membranes:** through lithography and dry etching [57];
- **Nanoporous silicon nitride membranes:** also using lithography and dry etching [58];
- **Porous nanocrystalline silicon membranes (pnc-Si):** spontaneous creation of pores during the rapid thermal annealing of amorphous silicon due to the nucleation of nanocrystals inside the material [59].

Each fabrication strategy holds is own advantages and disadvantages. For example, anodization through whole wafer thickness is time consuming and subjected to HF concentration variations, leading to non-uniform membranes. Freestanding membranes have a straight-forward fabrication method but they are hard to handle. Lateral and self-supported membranes require the use of microfabrication techniques but they can be easily integrated into devices [41].

As previously discussed, porous silicon's main advantage is the high tunability of its properties through fabrication parameters, and that also holds for porous silicon membranes. The removal of the underlying bulk substrate has no effect on the intrinsic properties of porous silicon, but it can impact the properties of PSi-based devices. In the framework of this project, the improvement in mass transport is the main property of interest.

Mass transport properties

One of the main limitations of close-ended porous silicon layers is linked to diffusion problems. For microfluidic operations based on porous silicon layers, the devices rely on a flow-over operation. However, due to the high aspect ratio of the nanopores, the flux into an individual pore is almost exclusively governed by diffusion and can be as slow as a few molecules per pore per second [60]. Therefore, one of the main drivers of PSiMs was the

need to overcome this diffusion limitation.

For PSiMs the transport of mass is influenced by both diffusion and convection, as the analyte flows through the pores, and can be described by the convection-diffusion equation [5]:

$$\frac{\partial c}{\partial t} = \nabla \cdot (D\nabla c - c\mathbf{u}) \tag{2.5}$$

where c is the analyte concentration, D is the diffusivity and $\boldsymbol{u}$ is the flow velocity.

The improved molecular transport efficiency of PSiMs has been shown for biosesing applications. The detection of a high molecular weight analyte (streptavidin) using a porous silicon matrix showed a 6-fold improvement in sensor response time when a flow-through property of interest rater than a flow-over operation, as shown in figure 2.21 [60].

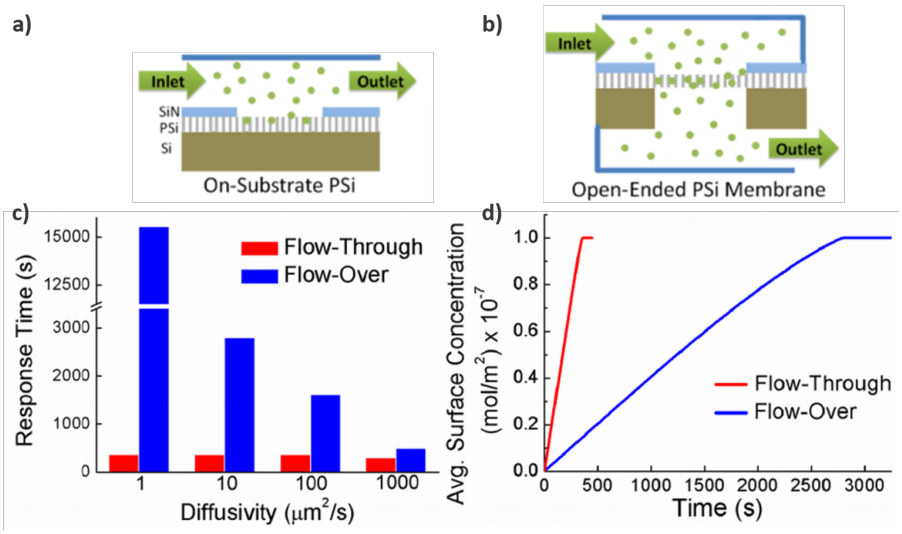

Figure 2.21: Schematic representation of: (a) a flow-over operation; (b) a flow-through operation. (c) Calculated response times of flow-over and flow-through porous sensors exposed to analytes with different diffusivities. (d) Average surface concentration of analytes with diffusivity of 10 μm^2/s that were captured by flow-over and flow-through porous sensors as a function of time. Extracted from [60].

Applications

Porous silicon membranes have been explored for different applications fully described in Ref. [41], including microfluidics, drug-delivery, scaffolds for cell culture, and sensing. However, some of the properties of PSiMs, such as mechanical stability, constitute challenges for the introduction of those devices into the market. Nevertheless, there is a growing interest in the development of PSiM-based devices.

Among microfluidics applications, size-based filtration is the most common. Usually mesoporous membranes are used, allowing only small nanometer-sized molecules to pass

through the filter. One example is the use of lateral porous silicon membranes for dead-end microfiltration. The membrane could successfully retain 300 nm diameter beads while macromolecules such as single-stranded DNA and immunoglobulin G permeate the membrane [56]. The same research group has proposed a charge-based filtration scheme that uses the permselecitivity[1] of the membranes in the presence of a charged buffer and an electric field [61].

As discussed biosensing is one important application of PSi, and PSiMs have show the advantages for this application due to increased sensitivity and shorter response time. Most PSiM-based biosensors rely on optical detection schemes [41]. The monitoring of the relative EOT has been used to track the binding of thrombin to aptamer, as shown in figure 2.22.a. thrombin-binding aptamers (TBA) was immobilized along the inner walls and thrombin in sample solution could be captured when passing through the nanochannels of PSiM integrated in a microfluidic cell [62].

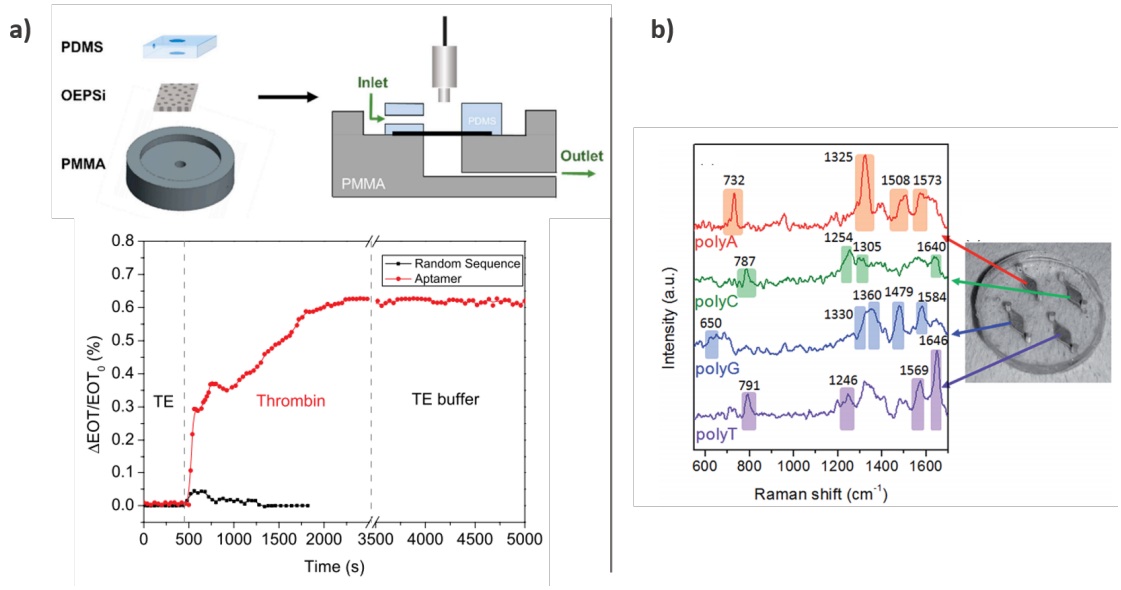

Figure 2.22: (a) Open-ended porous silicon (OEPSi) aptamer-modified optical biosensor: schematic representation on top and detection performance relying on the EOT increase upon thrombin bindig, extracted from [62]. (b) SERS spectra for multianalyte detection on four different silver nanoparticles decorated PSiMs, extracted from [63].

Surface-enhanced Raman spectroscopy (SERS) has also been applied for biomolecules detection. The Raman scattering of molecules is enhanced by the resonant excitation of surface plasmons in adjacent metal nanostructures and can be more easily measured. Underneath the metal nanoparticles, a dielectric substrate, such as PSiMs, is preferred to increase the sensor sensitivity [41]. A polydimethylsiloxane (PDMS) multichamber SERS-based microfluidic chip hosting Ag-coated porous silicon membranes (Ag-pSiM) was functonalized with a DNA probe. The fabricated biosensor was able to detect different organucleotides with a sensitivity comparable to to commercial techniques. The

[1] measure of the ability of a membrane to discriminate between anions and cations.

sensing platform was constituted by four chambers and each one was injected with a different solution: Polyadenine (polyA), polyguanine (polyG), polythymine (polyT), and polycytosine (polyC) solutions. The SERS sepctra for each chamber are shown in figure 2.22.b. and the fingerprint of each organucleotide is easily identified [63].

Chapter 3

Improving the stability of porous silicon membranes in aqueous media

Contents

Overview

This chapter exposes the problem of porous silicon reactivity in aqueous media and reviews some commonly used techniques to passivate the surface to prevent its dissolution/degradation. Porous silicon membranes are fabricated, submitted to low temperature oxidation and atomic layer deposition. Three different metal oxides are tested, namely HfO_2, TiO_2, and Al_2O_3. Finally, the membranes are characterized in terms of morphology, optical, mechanical and chemical properties. Stability tests, resistance to flow analysis, and noise level determination are also conducted.

3.1 Introduction and motivation

Porous silicon reactivity is dominated by silicon-silicon (Si-Si) and silicon-hydrogen (Si-H) bonds. Both Si-Si and Si-H are can reduce in water. In the case of Si-Si, this reduction will result in the generation of new Si-H species in addition to silicon oxides. Passivation of porous silicon, and its chemistry in general, has been developed in order to minimize this oxidation reactions [40].

In the context of biosensors based on porous silicon, one of the key limitations is the oxidation and subsequent dissolution of the mesoporous matrix in aqueous buffers, which leads to zero point drift [1] and reduces the ultimate sensitivity of the devices. Water is a competent oxidation agent for porous silicon, and the reaction with water vapor generates an oxide layer even at room temperature. If the reaction happens in aqueous solution, this oxide can be dissolved. At pH values higher than 7, hydroxide ions attack both S-H and Si-O surface species, and a complete dissolution of a microporous layer occurs within a few minutes at pH 10 [40].

The reaction follows the nucleophilic substitution mechanism. The attack by a nucleophile (OH^- in the case of basic solutions, but other nucleophiles such as amines can also perform the function) generates a 5-coordinate intermediate which then induces Si-Si bond cleavage, as seen in equation 3.1 [40].

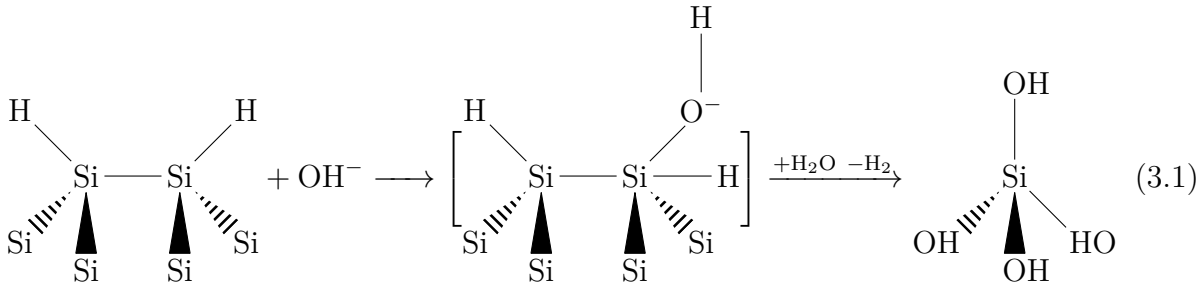

(3.1)

The reaction of the porous silicon surface with water to form silica acid, $Si(OH)_4$, is stable at low pH, but highly corrosive at high pH [41]. Because of this reaction mechanism, several solutions to improve stability of porous silicon in aqueous media have been investigate and include, among others, thermal oxidation, silanization, atomic layer deposition and thermal hydrocarbonization. These techniques are described in the following sections.

Another sensitive point linked to the intended application of the porous silicon membranes, i.e. flow-through biosensors, is the pressure required to pass the solution through. When choosing an adequate passivation technique, it is important to keep in mind that the higher the hydrophobicity of the passivated surface, the harder it is to pass the buffer solution through. However, increasing the applied pressure can cause rupture of the membrane.

[1] drift due to background oxidation by the aqueous matrix

3.1.1 Thermal oxidation

The most common approach to stabilize porous silicon is to purposely oxidize it. Temperature and humidity are important factors that influence the quality of the oxide layer [40]:

- Room-temperature oxidation (25 °C) (equation 3.2) produces a fairly thin oxide layer within a few hours, which grows over the course of several months;
- Atmospheric oxidation at temperatures below ∼200 °C (equation 3.3) also generates surface hydroxy species, and adsorbed water is observed on samples that have been exposed to humid air;
- Oxidation at 900 °C (equation 3.4) is enough to ensure complete conversion of the porous silicon skeleton to silicon oxide. The amount of time needed to accomplish this transformation depends on the type of sample (micro, meso or macroporous).

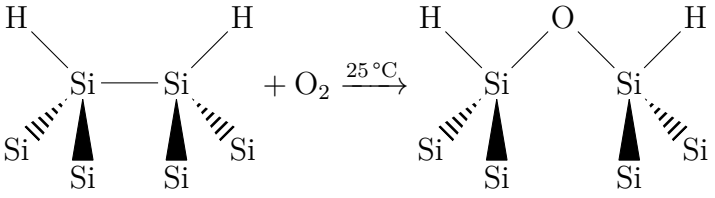

(3.2)

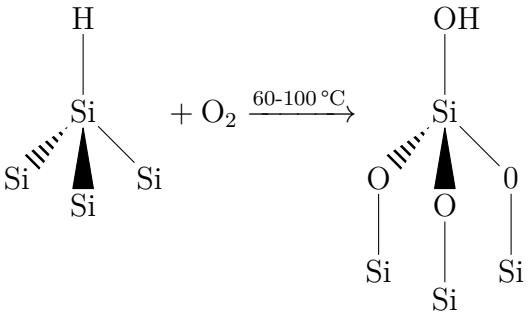

(3.3)

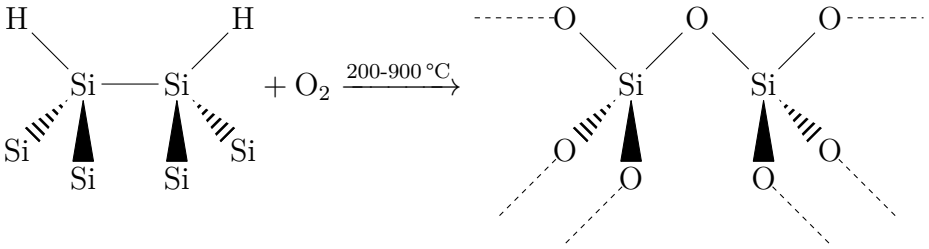

(3.4)

If a longer-lived oxide matrix is desired, silicon oxides formed at higher temperatures (> 700 °C) are significantly more stable in aqueous media than those formed at lower temperatures or by ozone oxidation. The most common approach to oxidizing porous silicon is to heat it in a tube furnace or a box oven, in air, for several minutes to several hours. The tube furnace can be fed with pure or humidified oxygen to better control the reproducibility of the process [40].

Unfortunately, thermal oxidation causes the expansion of the porous structure, and in mesoporous porous silicon membranes, leads to physical deformation and sometimes even degradation of the membranes [41]. Furthermore, the obtained interface results in a noisy signal. Indeed, due to the transformation of Si into SiO_2, the refractive index of

the material constituting the porous skeleton changes from 3.8 to 1.45. This change leads to low reflectance at the top of the interface of the porous layer when immersed in an aqueous medium, whose refractive index is about 1.4. As a consequence, the contrast is poor resulting in a noisy signal, which could prevent the detection of small changes inside the porous matrix [3].

3.1.2 Silanization

Oxidized porous silicon can be modified using conventional silanol chemistries [40], the so called silanization. It has been shown that grafting alkylsilanes through the formation of Si-O-Si bonds between silanol groups induced on the oxidized PSi surface and hydrolysed organosilane molecules of 3-aminopropyltriethoxysilane (APTES) or 3-aminopropyldimethylethoxysilane (APDMES) can be adopted as a passivation/functionalization strategy [64].

When atempting to modify a microporous structure, monoalkoxydimethylsilanes ($RO - Si(Me)_2 - R'$) can be more effective than trialkoxysilanes ($(RO)_3Si - R'$) as surface linkers. This happens because, by using trialkoxysilane reagents like APTES, crosslinking reactions are likely to happen, as shown in equation 3.5. This reactions produce large oligomers that clog micropores and limit the effective surface coverage. When using APDMES, the lack of additional Si–O bonds on the molecule eliminates the possibility of undesirable cross-linking reactions between other silanols, as shown in equation 3.6 [40].

The reactivity of porous silicon for drug delivery applications has been tested for different passivation techniques, namely oxidation, derivatization of Si-H bonds with APTES or APDMES and a combination of oxidation and derivatization. It has been found that oxidized batches have significantly lower reactivity after hydrosilylation with APDMES and the improvement is even more pronounced after hydrosilylation with APTES [65].

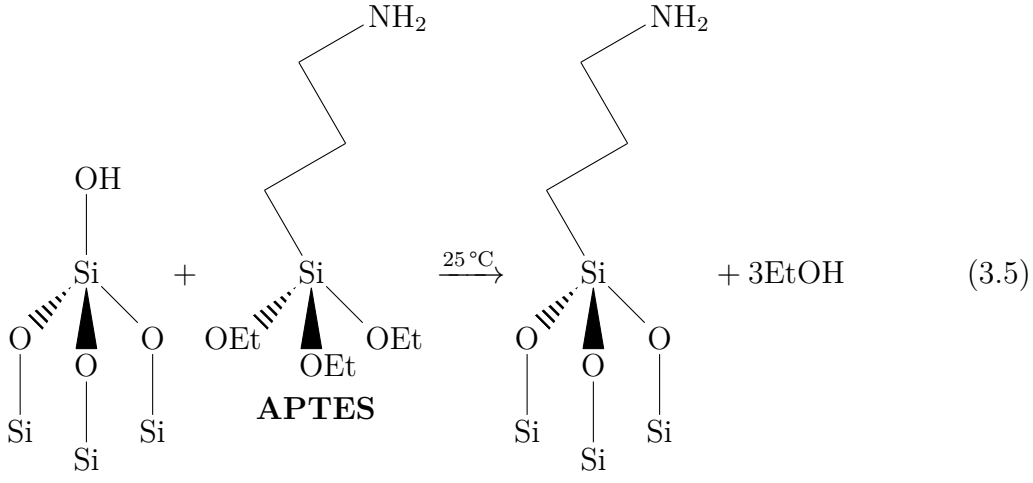

(3.5)

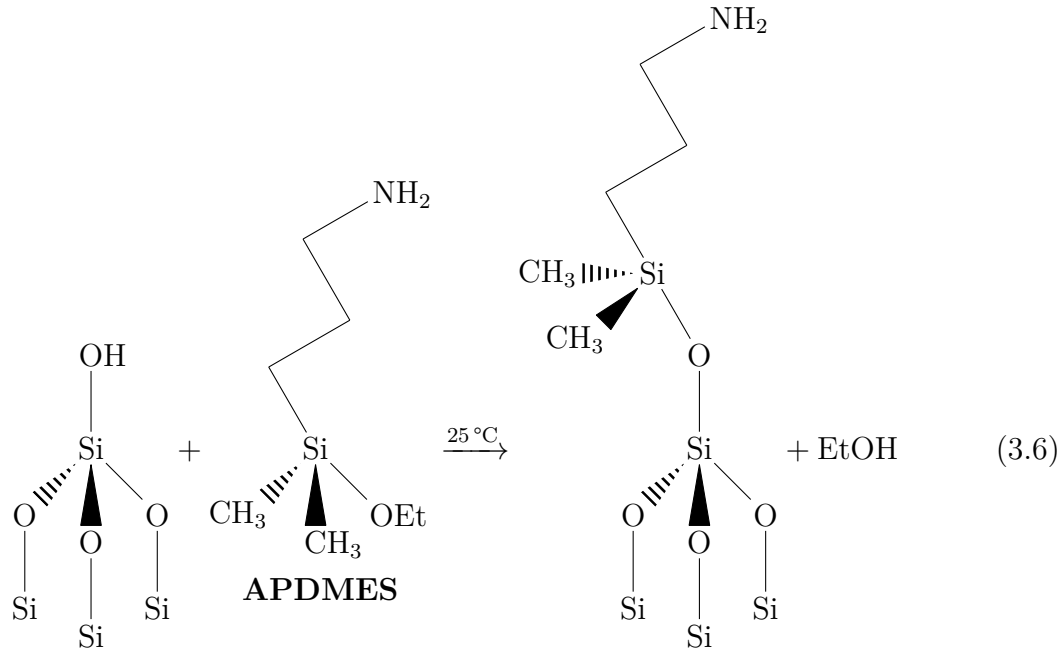

(3.6)

3.1.3 Hydrocarbonization

Carbon directly bonded to silicon yields a very stable surface species. Si-C bonded species possess greater kinetic stability relative to Si-O due to the low electronegativity of carbon. As previously reviewed, silicon can readily form 5- and 6- coordinate intermediates, and an electronegative element such as oxygen enhances the tendency of silicon to be attacked by nucleophiles, contributiong to the dissolution process.

Carbonized porous silicon can be generated by reacting the porous surface with gas phase acetylene, following equation 3.7. This can be achieved by placing a freshly etched porous silicon sample in a tube furnace, purging the tube with a constant flow of acetylene and nitrogen gas[2], and then increasing the temperature. The resulting structure is also known as "hydrocarbonized" porous silicon. Thermal oxidation studies of the treated surfaces show improvements in the stability against oxidation and the hydrocarbon termination was found to be very stable even in aqueous KOH environment [66].

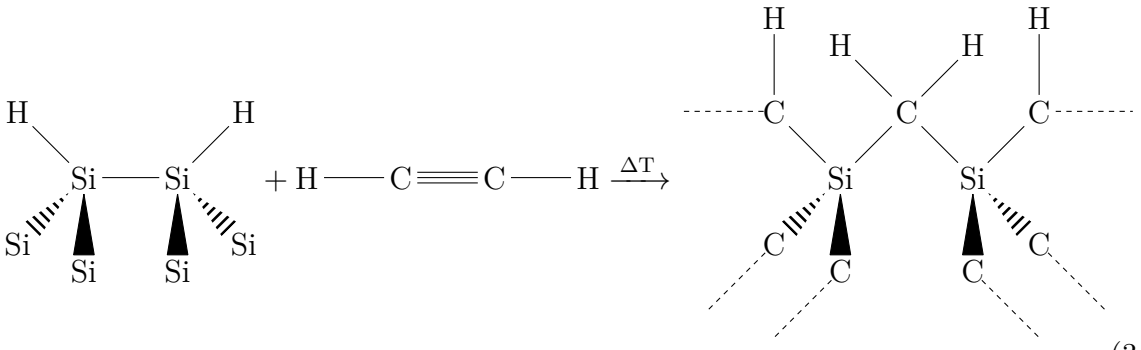

(3.7)

The temperature of the reaction plays a key role in determining the degree of hydrophobicity or hydrophilicity of the resulting "hydrocarbonized" porous film. It has been shown,

[2]acetylene gas is highly flammable, and so it is safer to dilute the gas with nitrogen

that lower temperature carbonized PS samples ($\approx$ 520 °C) are hydrophobic, as fresh PSi samples, while higher temperature carbonized samples ($>$ 730 °C) are hydrophilic [67].

As previously discussed, chemical stability in a physiologically relevant aqueous medium is an important characteristic of a biosensor. However, the surface chemistry must also allow permeation of the aqueous solutions. In order to reach both standards, functionalization of the surface by grafting carboxylic acid species has been proposed to increase hydrophilicity [68]. In this process, the radical initiator, benzoyl peroxide, is used to generate surface radicals. This initiator also decarboxylates a linker molecule, sebacic acid, that is added to the reaction mixture immediately after the initiator is added, following equations 3.8 and 3.9. Another route proposed to modify porous silicon with Si-C bounds is hydrosilylation using undecylenic acid which can be of particular interest for biosensing applications because it introduces a carboxylic acid functional group on the distal end of the molecule that can be used for further bioconjugation chemistries. The contact angle was measured directly after thermal carbonization of the porous silicon surface and corresponded to 116°(significantly hydrophobic surface). After the radical modification reaction, the contact angle decreased to 21°(large degree of hydrophilicity).

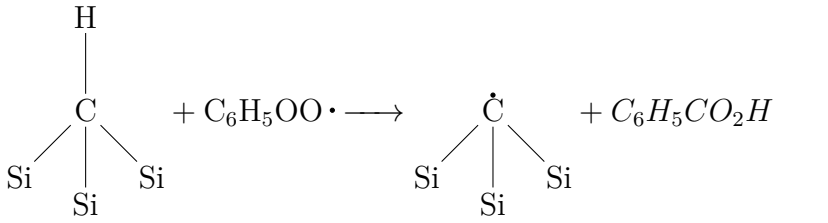

(3.8)

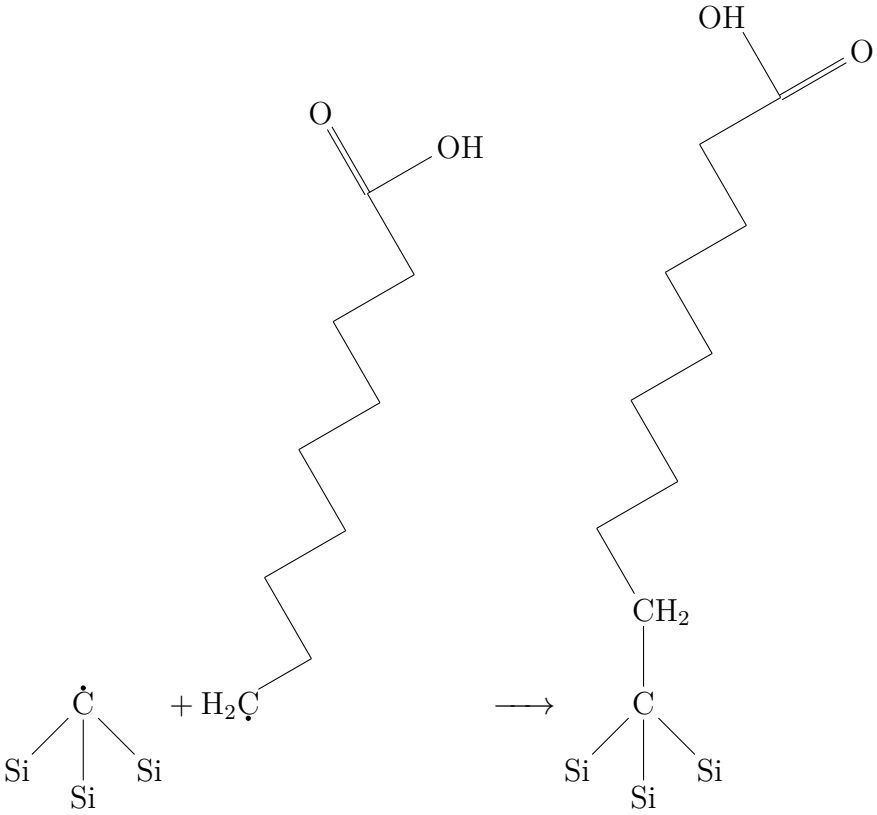

(3.9)

Stability tests were performed on porous silicon layers (not membranes) by monitoring the reflectance spectrum over time under a constant flow of phosphate buffered saline (pH

7.4) for 2h, as shown in figure 3.1. The data are presented as the fractional change in optical thickness (nL) as a function of time. The quantity $\Delta nL/nL_0\%$ is defined as the percentage change in optical thickness (product of refractive index n and physical thickness L) divided by the initial value of nL/nL_0 obtained within 10s of introduction of the PBS solution to the sample. For all chemistries studied, the optical thickness of the sample decreases upon exposure to the flowing buffer solution, indicative of slow degradation and dissolution of the porous film. However, the thermally carbonized and the sebacic acid terminated surfaces show the smallest rate of decrease in optical thickness indicating slower degradation in aqueous buffer [68].

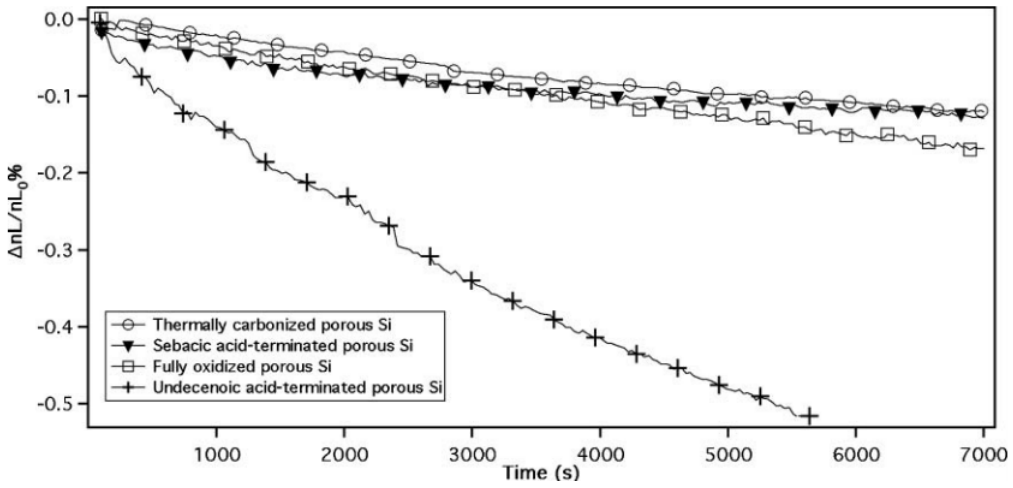

Figure 3.1: Degradation curves comparing the aqueous stability of porous Si modifications: thermally carbonized porous Si (open circles), thermally carbonized porous Si modified by radical coupling of sebacic acid (solid triangles), thermally oxidized porous Si (open squares), and porous Si hydrosilylated with undecylenic acid (crosses). Extracted from [68].

3.1.4 Atomic Layer Deposition

Atomic layer deposition (ALD) can be used to passivate the large internal surface of porous silicon layers and prevent their dissolution when in presence of aqueous media. This technique offers some advantages such as: highly conformal coating (ideal for porous silicon with its high-aspect ratio nanostructures), precise thickness control down to the Ångström level via its self-limiting mechanism, and it allows deposition of a vast array of materials [3].

ALD is also known as atomic chemical vapour deposition and it is a surface-limited reaction: one atomic layer is deposited in a single pulse of reactant gases. The first layer to react with the surface is chemisorbed (bond energies of the order of 1 eV) while additional layers are physisorbed (bond energies of the order of 0.4 eV). By correctly selecting the temperature and flush-gas pulses, it is possible to flush away the phyisisorbed layer and maintain only the atomic chemisorbed layer. By repeting the cycles it is possible to increase the layer thickness (equal to the number of pulses times the thickness of a monolayer) [69].

Stability tests were performed on porous silicon layers (not membranes) coated with

aluminium oxide (Al_2O_3) and with hafnium(IV) oxide (HfO_2) in a flow buffer solution during 120 min. Non-passivated porous silicon and thermally oxidized porous silicon were also submitted to the tests for comparison purposes. The stability is characterized as a ratio of EOT/EOT_0 between the effective optical thickness of the layer at the beginning of the experiment and after a given time [3]. As shown in figure 3.2, non-passivated porous samples exhibit a significant instability in aqueous media due to the oxidation/dissolution taking place. Passivated samples exhibit an improved stability with $PSiO_2$, PSi/Al_2O_3 and PSi/HfO_2.

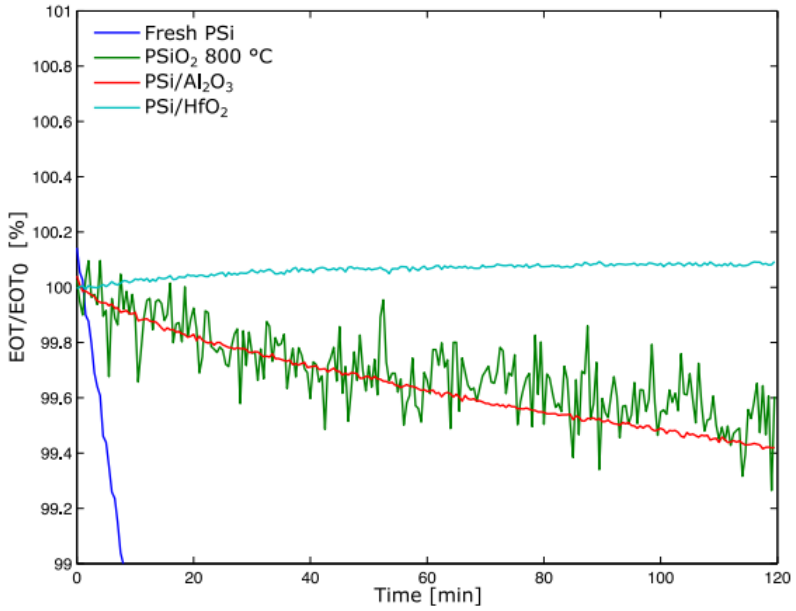

Figure 3.2: Relative EOT optical response of PSi (dark blue), $PSiO_2$ (green), PSi/Al_2O_3 (red), and PSi/HfO_2 (blue), as a function of time while exposed to a continuous PBS flow at a rate of 0.5 mL/min. Extracted from [3].

Furthermore, it has been shown that the theoretical LoD (limit of detection) for ALD oxide-covered samples is improved, by a factor 13 and 16 for PSi/Al2O3 and PSi/HfO2, respectively, compared to thermally oxidized PSiO2. This is an important parameter for sensing applications to detect small and rapid changes [3].

This chapter focuses on the use of ALD to passivate the internal surface of PSiMs and prevent their dissolution in aqueous media. The stabilization of PSiMs and its optical properties in aqueous media is demonstrated by using metal oxides ALD to conformally coat the internal surface. Three metal oxides are tested, namely HfO_2, TiO_2, and Al_2O_3. Their performance is compared to PSiMs oxidized at 200 °C.

3.2 Membranes fabrication and characterization: materials and methods

Porous silicon membranes were prepared in a clean room facility - Wallonia Infrastructure Nano Fabrication (Winfab UCLouvain). The process is illustrated in figure 3.3 and the steps are detailed in the following sections. The silicon wafers used are double-side polished, highly boron-doped p^{++}, «100» oriented, with resistivity between 0.8 and 0.9 $m\Omega.cm$, and thickness between 380 and 400 μm. They were purchased from Sil'tronix Silicon Technologies (France). Each wafer was first submitted to a standard cleaning using Piranha solution, composed of H_2SO_4 (97%) and H_2O_2 (30%) in the proportion 2:1 v:v. The wafers were immersed in this bath for 10 minutes, then plunged in a deionised water bath with a N_2 flux for another 10 minutes. The wafers were, then, plunged in a HF(2%) solution for 15 seconds and directly submerged in a second bath of deionised water. Finally the wafers were placed in a rinser-dryer for eight minutes.

3.2.1 Porous silicon masking

The first step is the deposition of a material that will act as a mask to delimit the regions that will undergo porosification. This mask must fulfill two main requirements:

1. Resist to the electrolyte (HF 49%:ethanol, 3:1 v:v) attack during electrochemical etching;

2. Electrically insulate the masked region to ensure current flows only through the unmasked areas.

Different strategies may be adopted for masking. In this work a double layer composed of silicon dioxide (electrical insulating) and polysilicon (electrolyte resistant) was used.

Silicon dioxide growth

Silicon is transformed into its oxide at high temperatures using either water vapor ("wet oxidation") or oxygen ("dry oxidation"). Water vapor is produced by combustion of hydrogen, H_2, and oxygen, O_2, in a torch. The oxidizing ambient also contains hydrochloric acid, HCl, to remove metal ions that may occur in the oxide [69].

Dry oxidation is typically slower than wet oxidation because the water solubility of silicon dioxide is four orders of magnitude larger that oxygen solubility. The oxidation rate depends slightly on crystal orientation, being higher for silicon of <111> orientation than of <100> orientation. For boron (p-type) doped silicon, the dopant incorporates into the growing oxide, weakening its bond structure and thus enabling faster diffusion through it [69].

Silicon dioxide, SiO_2, 90 nm, was grown through wet thermal oxidation, according to equation 3.10, in a vertical Koyo Thermo Systems furnace using the parameters shown

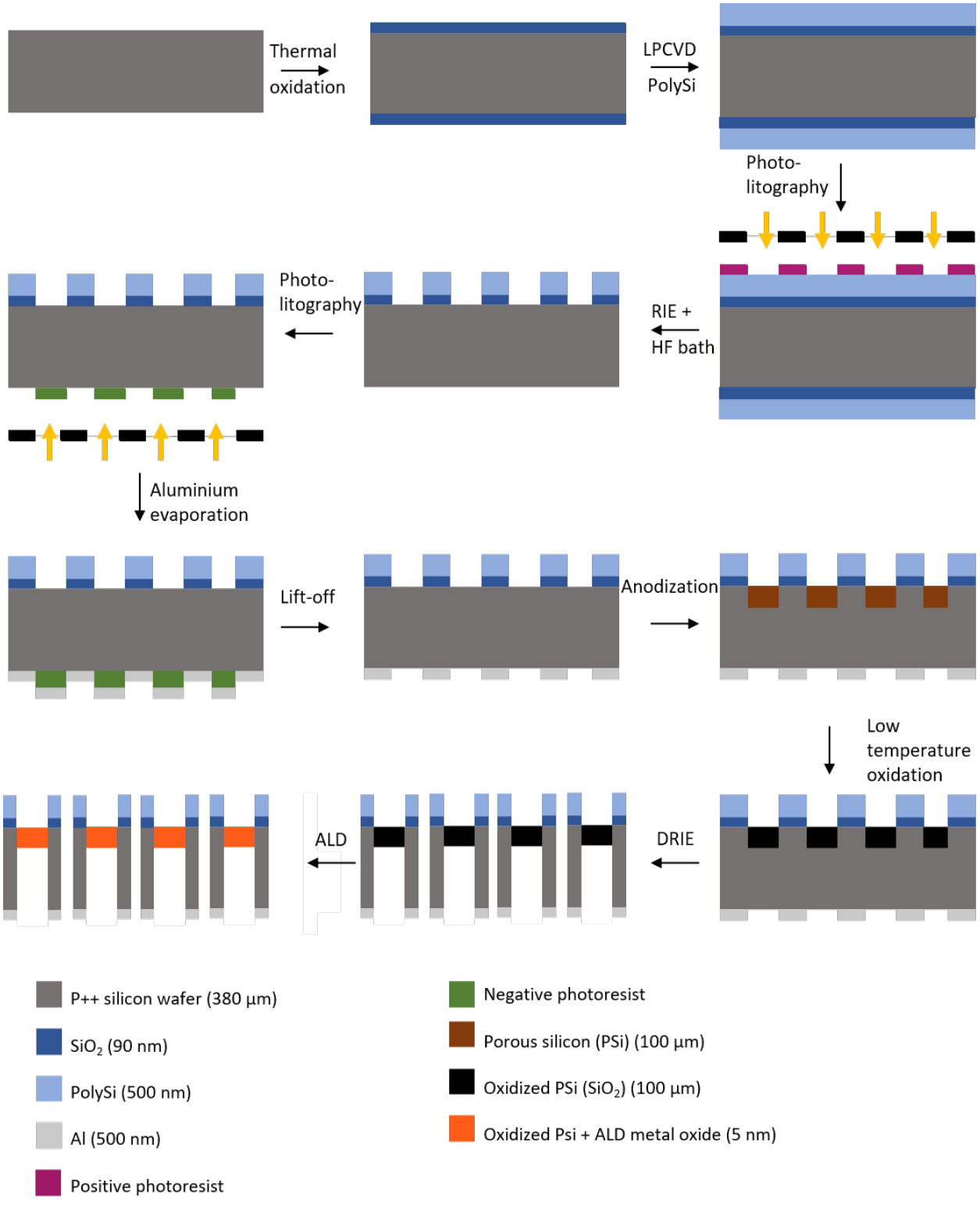

Figure 3.3: Schematic of the manufacturing process of PSi membranes.

in table 3.1. This material was chosen for electrical insulation due to its low electrical conductivity, 10^{-12} S/cm [70].

$$\mathrm{Si(s) + 2H_2O(g) \Rightarrow SiO_2(s) + 2H_2(g)} \tag{3.10}$$

Table 3.1: Parameters of thermal wet oxidation for the growth of a 90 nm thick silicon dioxide layer in a Koyo Thermo Systems.

Duration	H_2 flux	O_2 flux	HCl flux	Temperature
11 min	5.0 sccm	5.0 sccm	0.5 sccm	1000 °C

Polysilicon deposition

Polysilicon (polycrystalline silicon) is deposited through low pressure chemical vapor deposition (LPCVD). In this process, the source materials are brought into the reactor in the gas phase, they diffuse to the wafer surface, and react there to deposit a film. The byproducts are desorbed and pumped away, as shown in figure 3.4 [69]. For most CVD reactions, two temperature regimes can be observed: reaction limited and diffusion limited regime. LPCVD reactors operate in the surface reaction-controlled regime, usually resulting in uniform films with good step coverage [69].

LPCVD furnances are hot wall systems. Therefore, deposition also takes place on the walls leading to reactant depletion, and, as a consequence, the reaction rate at the entrance of the furnance is higher than near the exit. This effect can be compensated by temperature control, *i.e.,* reaction rate control, trough arrangement of heating elements in three zones, as shown in figure 3.5 [69].

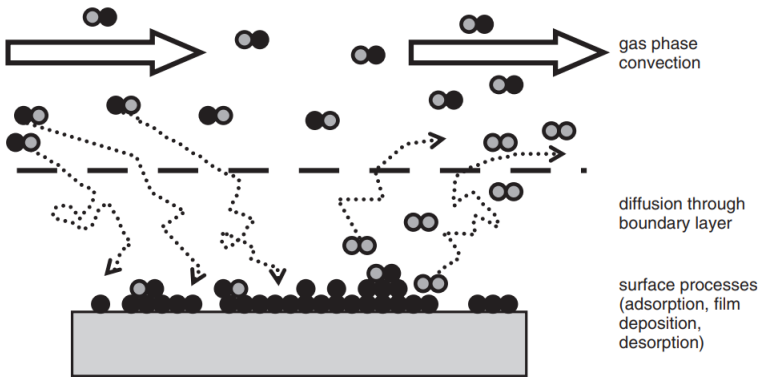

Figure 3.4: CVD process: source gas molecules adsorb and react on surface to form a film, and the reaction products are desorbed, diffused and pumped. Extracted from [69]

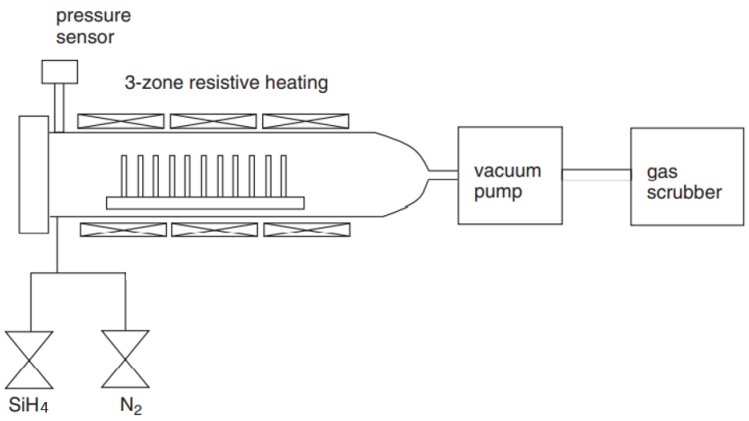

Figure 3.5: LPCVD three-zone polysilicon furnace (thermal CVD). Adapted from [69].

Polysilicon was deposited through LPCVD in a vertical Koyo Thermo Systems furnace through the thermal decomposition of silane, according to equation 3.11, using the parameters shown in table 3.2. This material was chosen due to its high resistance to HF [71].

$$SiH_4(g) \Longrightarrow Si(s) + 2H_2(g) \tag{3.11}$$

Table 3.2: Parameters for LPCVD of a 500 nm thick polysilicon layer in a Koyo Thermo Systems.

Duration	SiH_4 flux	N_2 flux	Temperature	Pressure
58 min	40 sccm	1 sccm	620 °C	35 Pa

Photolithography (positive photoresist)

Once the porous silicon masking layer is deposited, it needs to be patterned. In order to delimit the patterns, photolithography is performed. This technique uses UV lamps to expose specific areas of a photosensitive film through a photomasks to create patterns [69]. A typical process for for patterning a thin film through photolithography is shown in figure 3.6

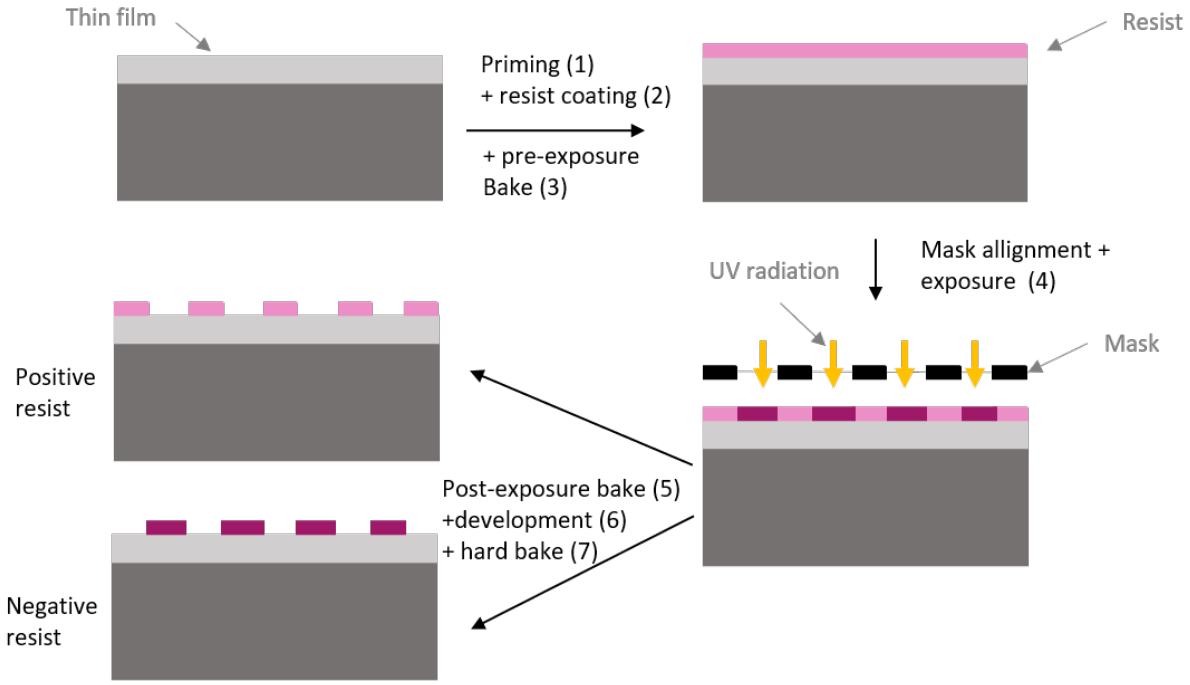

Figure 3.6: Schematic of a typical photolithography process: (1) the surface is prepared and a primer is added to improve adhesion, (2) spin-coating is performed to add an uniform layer of resist, (3) the coated wafer goes through a pre-exposure bake to remove the solvent excess from the resist, (4) the mask and the wafer are aligned, and exposed to UV light, (5) post-exposure bake is performed. For positive resists, the exposed parts release carboxylic acid and are (6) removed by an alkaline developer. For negative photoresists the exposed parts have been crosslinked and rendered stable, and the unexposed parts are (6) removed by a solvent developer. (7) Hard bake hardens the resist for following fabrication steps.

The process starts with surface preparation. First, absorbed water is removed in a furnace by degasing at 800 °C for 15 minutes under nitrogen. The next step is wafer priming, also called adhesion promotion. This is achieved by applying a primer, hexamethyl disilazane (HMDS), vapor at 120 °C for 40 minutes. This step makes the wafer slightly hydrophobic, preventing water readsorption and ensuring good wetting by photoresist [69].

The wafer is introduced in a Karl Süss Gamma 80 coater for coating and pre-exposure bake. The resist AZMIR 701 is applied by spin coating at 4000 rpm (acceleration of 1000 rpm/s) for 30 seconds to obtain a thickness of 700 nm. The pre-exposure bake to remove the solvent from the resist is performed at 90 °C for 90 seconds.

Exposure of the wafer is carried out through hard contact, to I-line 365 nm UV light during 6.9 seconds at 170 mJ/cm^2. Automatic wedge error compensation (WEC) is used to ensure that the mask and wafer are parallel. The exposure is carried out with a Karl Suss MA6 equipment, and with the mask depicted in figure 3.7.

The exposed wafer is reintroduced in a Karl Süss Gamma 80 coater for post-exposure

bake, development and hard bake. Post exposure bake at 110 °C for 90 seconds is employed to maximize process latitudes and to mitigate standing wave effects cause by monochromatic exposure [72]. The resist is developed, using the AZ 726 MIF developer (2.38% tetramethylammonium hydroxide, TMAH), for 60 seconds. Finally, a hard bake is carried out at 120 °C for 90 seconds.

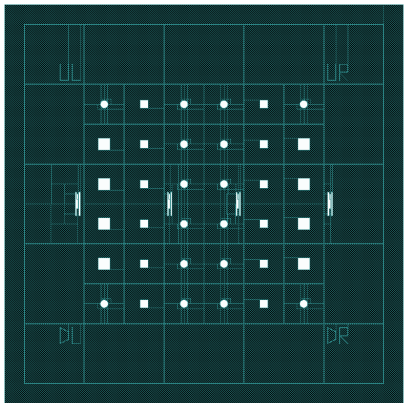

Figure 3.7: Mask used for photolithography. Large patterns (squares) and small patterns (squares and circles) are 2 and 1 mm wide respectively. Four vertical alignment and quality marks are spread in the horizontal direction.

Polysilicon and silicon dioxide etching

To transfer a pattern into a thin film, there are two steps: patterning of the resist through photolithography and subsequent etching of the underlying material. The resist protects the areas that need to remain and leave the areas to be etched opened [69].

The etching of the polysilicon within the patterns on the front-side and from the entire back-side of the wafer was performed by reactive-ion etching (RIE), also known as plasma etching. In plasma etching forced flow, boundary layer diffusion, and surface processes are enhanced by ion bombardment. On the one hand, the bombardment supplies energy to horizontal surfaces and drives vertical etching. On the other hand, sidewalls experience less ion bombardment, and therefore the etch rate in the lateral direction is reduced. The technique results in vertical walls and highly accurate reproduction of photoresist dimensions. The wafer is placed in a vacuum chamber and subjected to reactive gases excited by a radio-frequency (RF) field. In this process, both excited and ionic species play a role in reaction and bombardment, respectively. Different mechanisms take place in a plasma discharge [69]:

- Ionization: $e^- + Ar \Rightarrow Ar^+ + 2e^-$
- Excitation: $e^- + O_2 \Rightarrow O_2^* + e^-$
- Dissociation: $e^- + SF_6 \Rightarrow e^- + SF_5{}^* + F^*$

For etching to take place, chemical bonds need to be broken. Silicon can be etched by fluorine, chlorine and bromine because silicon–halogen bonds are stronger than silicon–silicon bonds. Furthermore, the volatility of reaction products is used as a criterion to select

the etchant, silicon is easily etched by halogens: the fluorides (SiF_4), chlorides ($SiCl_4$) and bromides ($SiBr_4$) of silicon are volatile at room temperature at millitorr pressures [69].

Inductive coupled plasma reactive ion etching (ICP-RIE) was conducted in an Oxford Plasmalab System 100 to etch 500 nm of polysilicon in the front and backside of the wafer, using the parameters shown in table 3.3.

Table 3.3: Parameters for ICP-RIE of a 500 nm polysilicon layer in an Oxford Plasmalab System 100.

Duration	SF_6 flux	RF power	ICP power	Temperature	Pressure
20 s	150 sccm	10 W	2000 W	15 °C	5 mTorr

The silicon dioxide within the patterns on the front-side and on the entire back-side of the wafer was removed by dipping the wafer in a 49% HF solution for a few seconds, following equation 3.12.

$$\mathrm{SiO_2} + 6\mathrm{HF} \Rightarrow \mathrm{H_2SiOF_6\ (aq)} + 2\mathrm{H_2O} \tag{3.12}$$

3.2.2 Hard masking for backside etching

After porosification, the backside of the wafer needs to be etched to remove the underlying bulk silicon substrate and create membranes. This final etching step removes over 300 μm of bulk silicon implying longer etch times. Many etching processes utilize hard masks because resists are simply not tolerant enough under harsh etch conditions [69], meaning, in this case, long etch time. Furthermore, the deposition of the hard mask was performed before porosification, as porous silicon puts constraints on further processing (no vacuum handling possible).

Aluminium was chosen as the material to be used as a hard mask due to its straight forward deposition, good electrical conductivity needed for the backside contact in the electrochemical etching step, and chemical resistance to SF_6 plasma. The deposition and patterning is possible through lift-off metallization with sacrificial resist shown in figure 3.8, going through the following steps:

1. photolithography patterning of sacrificial resist

2. metal deposition on the resist pattern

3. resist dissolution in solvent and lift off with all the metal that is not in contact with substrate being removed

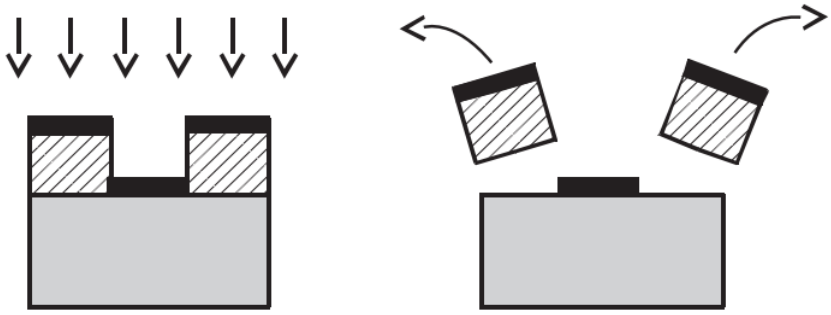

Figure 3.8: Lift-off process: left, metal deposition on resist pattern; right, resist dissolution and metal lift-off. Extracted from [69].

Photolithography (negative photoresist)

The backside surface of the wafer is first prepared by degasing under nitrogen (800 °C, 15 minutes), followed by HMDS application at 120 °C for 40 minutes.

The wafer is introduced in a Karl Süss Gamma 80 coater for coating and pre-exposure bake. The resist AZ® nLOF™ 5510 is applied by spin coating at 3000 rpm (acceleration of 1000 rpm/s) for 30 seconds to obtain a thickness of 950 nm. The pre-exposure bake to remove the solvent from the resist is performed at 110 °C for 60 seconds.

Exposure of the wafer is carried out through hard contact, to I-line 365 nm UV light at 120 mJ/cm^2, 1000 W. The exposure is carried out with a KW MA 1006 equipment, and with the mask depicted in figure 3.7.

The exposed wafer is reintroduced in a Karl Süss Gamma 80 coater for post-exposure bake and development. Post exposure bake at 110 °C for 90 seconds is required for proper imaging of AZ nLOF 5510 [73], and crosslinking of the exposed areas. The resist is developed, using the AZ 300 MIF developer (2.38% tetramethylammonium hydroxide, TMAH), for 60 seconds.

Metallization and lift-off

Aluminium is deposited through evaporation. Evaporation systems are either high vacuum (HV), pressure around 10^{-7} Torr, or ultrahigh vacuum (UHV), pressure around 10^{-9} Torr, systems. In (ultra)high vacuum systems, the atoms do not experience collisions, and they can follow a line-of-sight route from source to substrate [69]. Indeed, the mean free path of atoms, *i.e.,* the measure of collisionless transport, or the distance that an atom can travel before collision, can be increased by decreasing the pressure.

This is a low temperature process with a line-of-sight deposition and, as a consequence, evaporated films will not coat sidewalls of holes and ridges well, even though film quality on planar surfaces is good [69]. This poor step-coverage characteristic makes this method suitable for lift off metallization because it avoids the creation of a bridge between the films on the photoresist and on the subtract, allowing the etching of the underlying sacrificial

resist.

Aluminum was evaporated in an e-gun VST, at a 5 Å/s rate, using the parameters shown in table 3.4.The metal is heated by an electron-beam and vaporizes, the evaporated atoms are transported in high vacuum to the substrate wafer, as shown in figure 3.9.

Table 3.4: Parameters for evaporation of a 300 nm thick aluminium layer in an e-gun VST.

Duration	Temperature	Pressure
10 min	room T	4×10^{-7} mBar

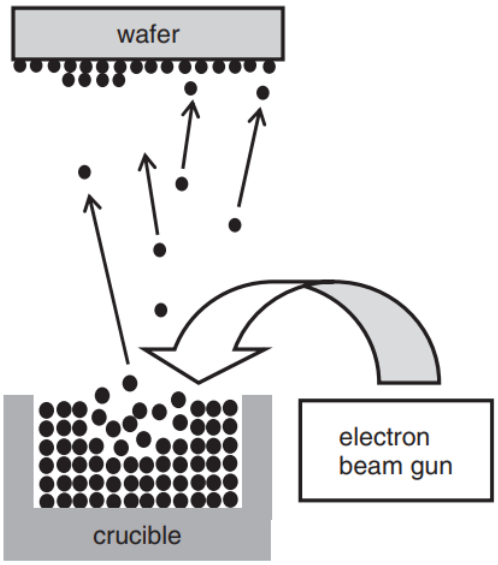

Figure 3.9: Schematic of electron beam evaporation. Extracted from [69].

The resist is finally dissolved in acetone with ultrasonic agitation, leaving only the metal in contact with the substrate.

3.2.3 Electrochemical etching

The principle of porous silicon fabrication has been described in section 2.3.1. In this work, electrochemical etching (or anodization) is performed in a single-bath Teflon etch cell, schematically shown in figure 3.10, with an HF (49%):ethanol (3:1 v:v) electrolyte. An electrical contact is made at the platinum electrode that is submerged in the electrolyte and another at the back of the wafer. The area exposed to porosification, inside the patterns, is 2.229 cm^2.

First, a sacrificial layer is etched. This method is a relatively quick and thorough cleaning procedure that provides good, reproducible surfaces [40]. This layer is etched with a current density of 200 mA/cm^2 during 30 seconds in the mentioned electrolyte.

After the etch, the electrolyte is removed and the cell is rinsed with isopropanol (IPA) and dried with a N_2 flux. The sacrificial layer is then removed by immersing the sample in a 1 mol/L potassium hydroxide (KOH) solution. Once the reaction is over, evidenced by the lack of bubbling, the KOH is removed, and the wafer is rinsed with deionised water and IPA.

The wafer was immersed in the electrolyte again to etch an stack of three layers: sensing layer, contrast layer and support layer, as shown in figure 3.11. The sensing layer (approximately 5 μm) was etched at 225 mA/cm^2 for 50 s. This was followed by a 880 s etch at 50 mA/cm^2, making a thick optical contrast layer (approximately 10 μm) characterized by lower porosity, enabling the reflection of the light required for the RIFTS method; finally, a thick mechanical support layer (approximately 100 μm) was etched at 100 mA/cm^2 for 3200 s. The current densities chosen for each layer have been optimized to guarantee a good mechanical stability and optical signal, while retaining pores large enough for the flow-through operation, according to the method proposed by Vercauteren *et al.*[5].

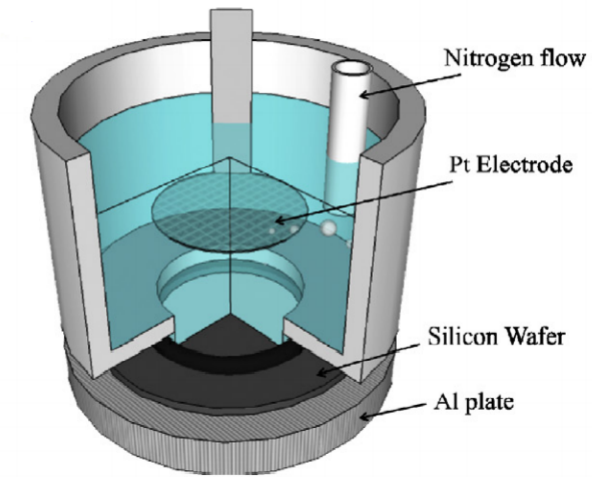

Figure 3.10: Illustration of a single-bath electrochemical etching cell: the wafer is put into contact with the aluminium plate on the bottom, the platinum electrode is introduced into the electrolyte solution in contact with the wafer's front side. One electric contact is made on the electrode and another on the aluminium plate. Extracted from [41].

For thick porous silicon layers, as is the case for the three-layers stack, the variations of HF concentration with depth cannot be neglected. These changes of the HF concentration cause a porosity gradient, which degrades the device performance and mechanical stability. To solve this problem, the method of etch stops was applied, meaning that break steps were imposed during the etching: they induce a regeneration of the HF concentration at the pore tips during the break time [74]. The current density, etch and break steps used for each layer are described in table 3.5

Table 3.5: Current densities adopted, etch and break steps duration for each layer.

	Current density $[mA/cm^2]$	Etch step duration $[s]$	Break step duration $[s]$	Total duration (etch+break) $[s]$
Sensing layer	225	50	-	50+0
Contrast layer	50	5	1	880+176
Support layer	100	10	1	3200+320

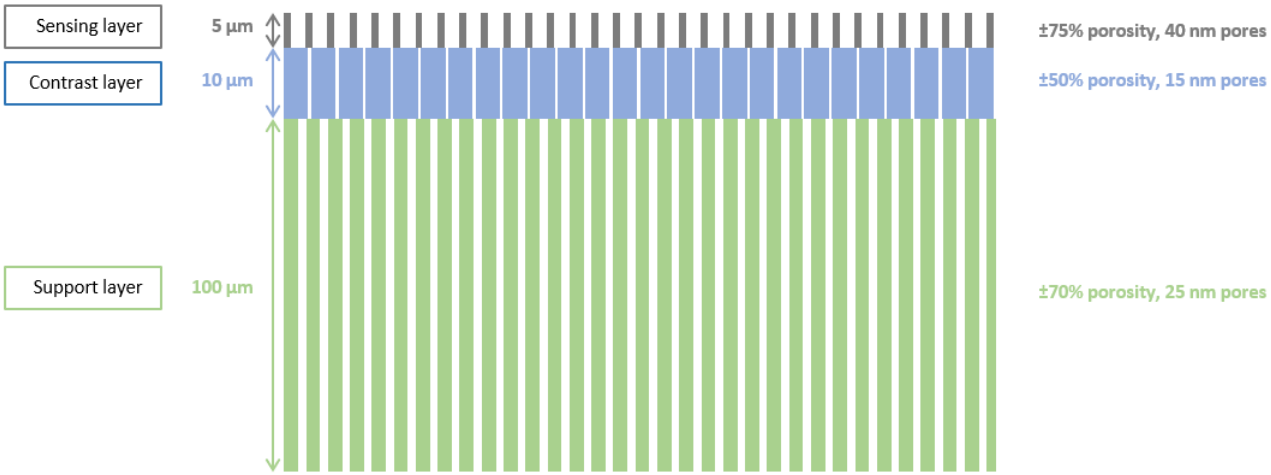

Figure 3.11: Schematic of a tri-layer porous silicon stack successively etched at 225, 50 and 100 mA/cm^2.

3.2.4 Backside etching

To obtain a membrane, the porous layer needs to be detached from the underlying bulk silicon substrate [41]. In this work, self-supported PSiMs are fabricated by first electrochemically etching the silicon wafer on the front side over a an approximately 115 μm thickness before removing 260-280 μm from the backside. This is achieved through deep reactive ion etching (DRIE), a dry etching technique.

To create an etch-stop as soon as the backside etching reaches the porous matrix, the freshly etched PSi is submitted to an oxidation at low temperature (200 °C) to avoid bending or cracking of the porous matrix. Indeed, after porosification, thin pore walls are obtained and oxidation at high temperatures can be detrimental for the mechanical stability of the membranes.

The wafer is introduced in an oven under a 1.5 L/min O_2 and 1.2 L/min N_2 flow, heated for 30 min until reaching 200 °C, and then left for 30min at 200 °C. The presence of nitrogen in the annealing environment helps to decrease the stress level on the porous matrix [75].

The DRIE used for the backside etching is an extension of RIE for deep etching, meaning higher thicknesses. The chosen process is the Bosch process that alternates SiF_6

and C_4F_8 gas pulses. The first SiF_6 pulse etches a few micrometers of silicon, but etching is not completely anisotropic. Then, a C_4F_8 pulse is applied to deposit a fluoropolymer protective film all over the wafer. The next etching pulse, SiF_6, removes the polymer film from the trench bottom by ion-assisted-etching, leaving the sidewalls protected. The alternating pulsing process is repeated leaving an undulating sidewall, shown schematically in figure 3.12 [69].

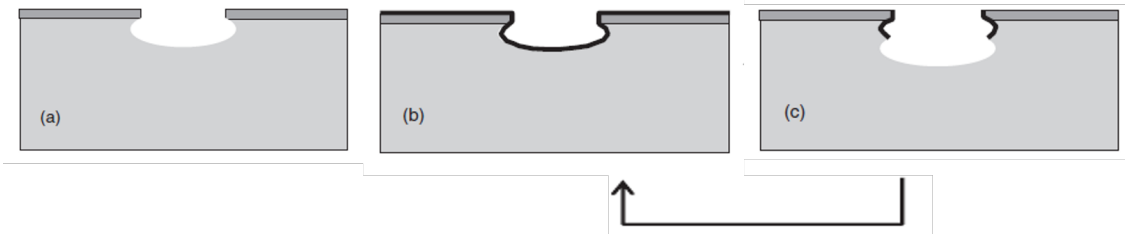

Figure 3.12: Bosch process, etch and passivation pulses repeated: (a) SF_6 isotropic etch step; (b) C_4F_8 passivation layer deposition; (c) next etch step. Adapted from [69].

The parameters of a DRIE cycle used in this work are presented in table 3.6. Around 400 cycles, performed in an Oxford Plasmalab System 100, are carried out in order to etch 260-280 μm of silicon.

Table 3.6: Parameters for DRIE of approximately 260-280 μm of silicon in an Oxford Plasmalab System 100.

	Deposition	Etch
Duration	6 s	13 s
SF_6 flux	1 sccm	120 sccm
C_4F_8 flux	150 sccm	1 sccm
RF power	30 W	30 W
ICP power	1500 W	1500 W
Temperature	-10 °C	-10 °C
Pressure	20 mTorr	20 mTorr

3.2.5 Atomic Layer Deposition

Atomic layer deposition (ALD) is a gas phase thin film deposition technique that allows the deposition of highly conformal coatings. It is characterized by exposing the substrate to an alternating sequence of vapor phase reactants. The surface reactions have a self-saturating nature allowing the control of the film thickness at the atomic scale. Typically, the ALD process is a repetition of cycles, each one with four characteristic steps. Figure 3.13 shows an schematic representation of one ALD cycle for the deposition of Al_2O_3 through the thrimethylaluminium (TMA)/H_2O process. The four steps observed are [76]:

1. The first reactant A (TMA) reacts with the $-OH$ terminated surface in a self-terminating way;

2. The excess of reactant A (TMA) and the gaseous byproducts (CH_4) are purged away;

3. The second reactant B (H_2O) is introduced in the chamber and reacts with the absorbed species (A) on the surface, also in a self-terminating way;

4. The excess of reactant B (H_2O) and the gaseous byproducts (CH_4) are purged away, and a new cycle may begin.

Al_2O_3, HfO_2 and TiO_2 atomic layer depositions were performed in different membranes. The precursors (reactant A) used were TMA, tetrakis(dimethylamido)hafnium (TDMAH), and tetrakis(dimethylamido)titanium (TDMAT), all purchased from SAFC Hightech®. After each ALD cycle, a certain amount of material (coating) is deposited on the surface, which is called the growth per cycle (GPC) and it is usually expressed in Å/cycle. Furthermore, at a given pressure, a certain minimum amount of time is required before the sample surface is fully covered with adsorbed reactant molecules and saturation is reached. The so-called reactant exposure is defined as the product of the reactant partial pressure by the pulse time, and it is expressed in Langmuir (1L =10^6 Torr.s). For high aspect ratio structures, such as the case of the porous silicon membrane fabricated in this work, much larger exposures are needed to compensate for diffusional limitations [76]. Low temperature depositions were adopted to prevent cracking and deflection of the membranes. The number of cycles was adjusted to have a similar thickness for the different metal oxides, the deposition parameters are presented in table 3.7. The oxide growths were performed in a Fiji F200 ALD reactor (Veeco/CNT, MA, USA) in exposure mode, meaning that the chamber was isolated from the pump during the precursor pulses to allow the precursors to penetrate deeply into the nanostructure to ensure a homogeneous coating throughout the depth of the porous matrix.

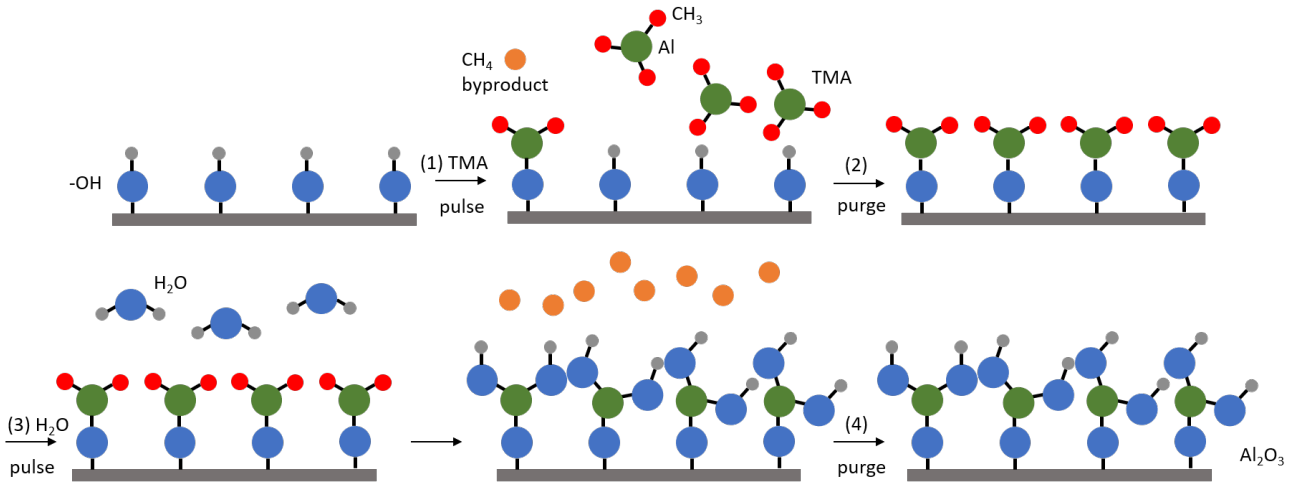

Figure 3.13: Schematic representation of one ALD cycle of the TMA/H_2O process.

3.2.6 Porous silicon membranes characterization

Porous silicon samples after different steps of the process (electrochemical etching, annealing, backside opening and ALD) are characterized using several techniques. Different

Table 3.7: Parameters for ALD of different metal oxides in a Fiji F200 ALD reactor.

	HfO_2	Al_2O_3	TiO_2
Pulse (Reactanct A)	0.3 s	0.5 s	0.2 s
Wait	120 s	120 s	120 s
Purge	360 s	360 s	360 s
Pulse (Reactanct B, H_2O)	0.1 s	0.1 s	0.2 s
Wait	120 s	120 s	120 s
Purge	360 s	360 s	360 s
Total number of cycles	20	40	50
Deposition temperature	100 °C	100 °C	150 °C

techniques are used to assess the properties of interest: porosity, thickness, pore morphology and optical signal; membranes passivation through ALD; mechanical properties and resistance to flow.

Porosity, thickness, pore morphology and optical signal

First, the reflectance spectra of the membranes are taken using the set-up shown in figure 2.13. They are optically characterized through the SLIM method, as described in section 2.3.3, to obtain the porosity and the thickness of the PSi layer. The reflectance spectra are also used to evaluate the intensity of the signal after the different steps of the fabrication process.

Scanning electron microscopy (SEM), using a Carl Zeiss Ultra 55 SEM, is the second characterization method and it is used to obtain top-view and cross-section images of the membranes. The cross-section images allow the measurement of the different layers thicknesses, while the top view images are used to obtain the pore openings. Through an image analyzer MATLAB (MathWorks) routine, developed and fully described in Ref. [3], it is possible to obtain an estimation of the porosity and pore size distribution from the top view images. The SEM top view images are loaded into the routine and their grayscale contrast is enhanced to ease the distinction between pores (in black) and surface (in white/gray). A binary image is then obtained with the black areas corresponding to the pores. The speckles are removed through operations corresponding to the erosion, dilation and filling of the pores. The diameter of the pores D is computed by assuming they are circular $D = 2\sqrt{A/\pi}$, with A being the pore area [3]. Through this same analysis, the decrease in pore size after ALD at the surface of the membrane can be assessed, giving an estimation of the thickness of the deposited layer and of the growth per cycle.

Membranes passivation

There are two main properties to be characterized after the different atomic layer depositions: homogeneity of the deposited films (through the pores depth) and chemical composition of the surface species. In order to do so, two techniques were adopted: Energy Dispersive X-Ray spectroscopy (EDX) and X-Ray Photoelectron Spectroscopy (XPS).
In the SEM the area to be examined or the microvolume to be analyzed is irradiated

with a finely focused electron beam. The electron-matter interactions produce secondary electrons, backscattered electrons, characteristic x-rays, and other photons of various energies. Each of these signals are obtained from specific emission volumes through the sample's depth and can be used to characterize different features (surface topography, crystallography, composition, etc.). Composition information can be obtained through characteristic x-rays emitted as a result of electron bombardment [77].

By adding a energy-dispersive spectrometer (EDS) to the SEM, elemental analysis or chemical characterization of the sample is possible. The principle behind the characteristic x-ray emission is shown in figure 3.14.a.: (i) an electron beam interacts with an inner shell electron of the sample; (ii) the primary electron is scattered, an orbital electron is ejected, and the atom itself is left in an excited state with a missing inner shell electron; (iii) for this example, the vacant state in the inner electron shell (K shell) is filled with an electron from the next shell out (L shell), and a x-ray is created. Thus, the energy of the x-ray produced is equal to the difference in energy between the K shell and the L shell. Since the energies of electrons in the shells (atomic energy levels) are sharply defined with values characteristic of a specific element, the energy of the x-ray produced has a value characteristic for each element. Finally, it is possible to perform elemental identification by evaluating the emitted x-ray energy [77].

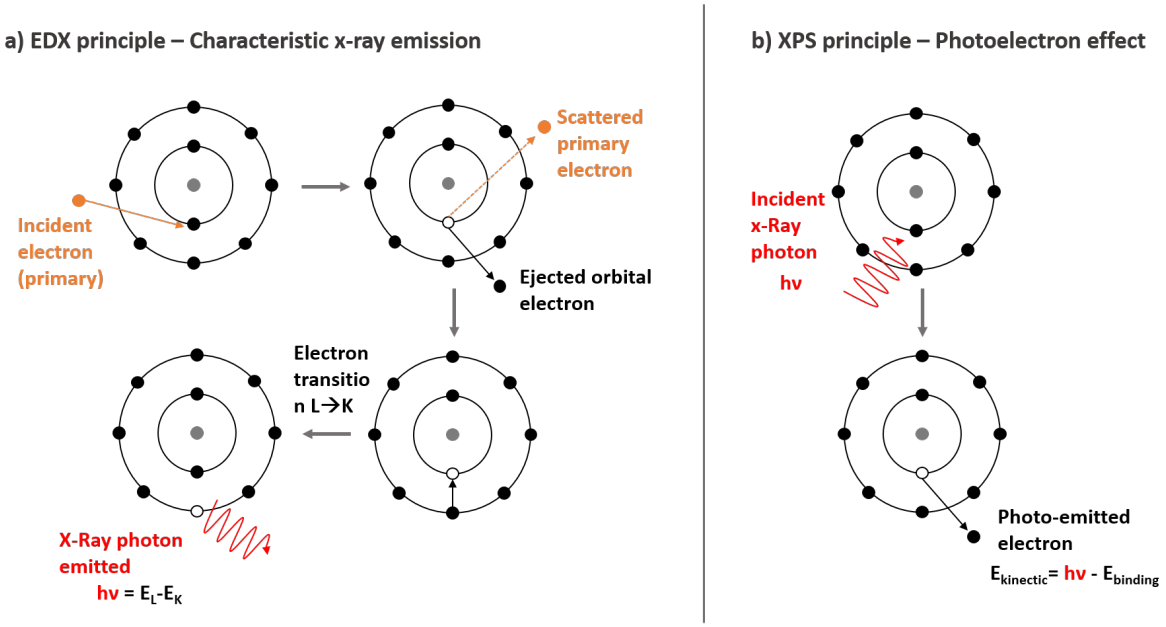

Figure 3.14: The working principle behind a) EDX and b) XPS. Adapted from [77] and [78].

XPS relies on the photoelectric effect. The principle behind this effect is shown in 3.14.b.: (i) the surface to be analyzed is irradiated with photons on the x-ray range; (ii) the irradiated atom emits electrons (photoelectrons). The photoelectrons emitted from atoms near the surface can escape into the vacuum chamber and be separated according to their energy. The kinectic energy of the photoelectron is equal to the energy of the x-ray source ($h\nu$, where h is the Planck's constant and ν is the frequency) minus the binding

energy of the electron in the atom [78]. Only core electrons are interesting to be analyzed as their binding energies are characteristic of the atomic number.

The binding energy of an electron in an atom will vary with the type of atom and the addition of other atoms bound to that atom (bound atoms will alter the electron distribution of the atom of interest). Therefore, variations will be seen in the binding energy, called the binding energy shift or chemical shifts, and they give information on the chemical content, associated with covalent or ionic bonds between atoms [78].

These techniques have several differences, revealing their strong and weak aspects, as summarized in table 3.8, namely surface sensitivity, lateral resolution, and chemical shift (possibility to assess the chemical environment).

Table 3.8: Comparison between EnergyDispersive X-Ray spectroscopy (EDX) and X-Ray Photoelectron Spectroscopy (XPS) techniques. Information extracted from [79] and [78].

	EDX	**XPS**
Excitation by	electrons	x-rays
Detection of	x-rays	electrons
Surface sensitivity	0.5-10 μm	1-10 nm
Lateral resolution	1 μm	10-15 μm
Chemical shift	No	Yes

Surface sensitivity (also called information depth) will depend on the penetration depth of the particles that bombard the sample and on the escape depth λ, also called inelastic mean free path length. The inelastic mean free path stands for the perpendicular distance from the surface at which the probability of an electron escaping without energy loss (due to inelastic scattering processes) drops to $1/e \approx 0,37$ (where e is the Euler's number) of its original value. In a depth of 3λ, 95% of all particles have lost their energy by collisions. This depth of 3λ is called the information depth [79].

For EDX, the penetration depth of the electrons is determined by the stopping power of the respective material-depending on its density and by the accelerating voltage of the electron beam, varying within a range of approximately 0.5-10 μm. As the emitted x-rays emerge from a similar range of depth, the information depth is nearly the same as the penetration depth, and the surface sensitivity will be also 0.5-10 μm [79].

For XPS, the x-rays of typically 1 keV will penetrate up to 1 μm or more inside the sample (penetration depth), however, electrons with the same energy will only be able to penetrate approximately 1 nm. Because of this difference, electrons emitted from x-ray excitation below the uppermost surface zone cannot penetrate far enough to escape from the sample and reach the detector. Therefore, the surface sensitivity will be far greater, in the order of 1-10 nm [79].

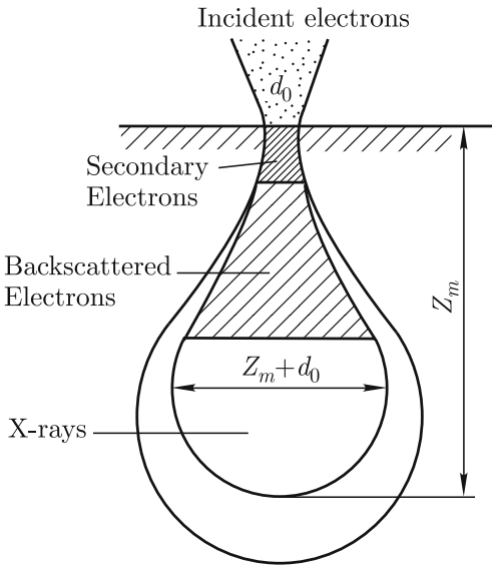

Figure 3.15: Diagram showing the interactive volume of electron beam and a sample, $Z_m \approx 1\mu m$. Extracted from [80].

The lateral resolution is the ability to recognize and analyse adjacent points on the sample's surface. The lateral resolution of the EDX is related to the electron penetration figure, which often has the shape of a pear, as shown in figure 3.15, of approximate diameter 1 μm [79].

For XPS, the best focus for x-rays that can be achieved in a conventional XPS instrument is from a few to several mm^2. Furthermore, the reduction of the x-ray spot size drastically reduces the x-ray flux and so the number of emitted photoelectrons, limiting the practical lateral resolution of this technique to approximately 10-15 μm [78].

From the above discussion, it is possible to conclude that XPS is a surface sensitive technique that allows the determination of the chemical environment surrounding the atoms. EDX is the better technique when high lateral resolution is searched. Since the membranes are approximately 100 μm thick, the ALD evaluation through depth is only possible through EDX in cross-section (the XPS spot diameter is too high, 300 μm for the available equipment). However, XPS is still a useful technique to evaluate the deposition on the surface and to assess the chemical characterization of the surface species.

The membranes cross-section chemical composition was investigated by scanning electron microscopy (Carl Zeiss Ultra 55 SEM) with the energy dispersive X-ray spectroscopy (EDX) analyzer. XPS analyses were carried out on the top and back sides of the membranes with a SSX 100/206 photoelectron spectrometer from Surface Science Instruments (USA) equipped with a monochromatized micro focused Al X-ray source (powered at 20 mA and 10 kV). The samples were fixed with double-sided tape onto a ceramic carousel. The pressure in the analysis chamber was around 10^{-6} Pa. The angle between the surface normal and the axis of the analyser lens was 55°. The analysed spot size was approximately

300 μm and the pass energy was set at 150 eV. In these conditions, the full width measured at half maximum (FWHM) of the Au $4f_{7/2}$ peak for a clean gold standard sample was about 1.6 eV. A flood gun set at 8 eV and a Ni grid placed 3 mm above the sample surface were used for charge stabilisation. The C-(C,H) component of the C1s peak has been fixed to 284.8 eV to set the binding energy scale. Data treatment was performed with CasaXPS program (Casa Software Ltd, UK), some spectra were decomposed with the least squares fitting routine provided by the software with a Gaussian/Lorentzian (85/15) product function and after subtraction of a non-linear baseline. Molar fractions were calculated using peak areas normalised based on acquisition parameters and sensitivity factors provided by the manufacturer.

Mechanical properties assessment

The introduction of nanoscale porosity into silicon dramatically lowers its stiffness and hardness, often in a tunable manner over a wide range. However, the mechanical properties of porous silicon have not received much attention, specially when compared to its other properties such as structural, luminescent, thermal, and optical properties. Nevertheless, as the research on PSi advances, the scientific field is realizing that to obtain robust devices and system performance, achieving the appropriate mechanical properties is essential [81].

Different studies evaluated the Young's modulus as a function of porosity in silicon, and the agreement between differing measurement techniques is generally good for similar material, as shown in figure 3.16. Furthermore, in the case that the hypothesis of pores with cubic symmetry stands, for mesoporous silicon, it has been shown that the Young's modulus experimental values agree with the theoretical prediction expressed in equation 3.13 [82].

$$E_p = CE_b(1-p)^2 = A(1-p)^2 \tag{3.13}$$

where E_p and E_b are the Young's moduli of the porous and bulk materials, respectively, C is a constant including all the geometric scaling factors and p is the porosity. The value of A has been calculated based on experimental data, and it was concluded that $A = 120\ GPa$ provides a good fitting, which is of the order of magnitude of the nonporous i.e., bulk silicon Young's modulus $E_b = 162\ GPa$ [82].

Another model, taking into account the influence of the pore shape on elastic parameters, has been proposed and investigated through Finite Element Methods (FEM) simulations [83]. Observations have shown that pores in PSi are not always as perfect as cylinders, but present different morphologies depending on the etching conditions and substrate properties like doping type and level, crystalline orientation, etc. Mesopores grow in <100> directions and they are usually branched with branches are at right angles to the main pore [84]. A fitting function of Young's modulus E of PSi has been proposed as a power law of the porosity defined by equation 3.14 [83]:

$$E = E_0'(1-\phi)^m \tag{3.14}$$

where E_0' is a scale factors which normally equal to the Young's modulus of crystalline silicon, and m is the fitting number depending on the pore morphology. For branched pore morphology, $m = 2.11$ and E_0' is given by equation 3.15 [83].

$$E_0' = \frac{1}{2}\frac{(c_{11}-c_{12})(c_{11}+2c_{12})}{c_{11}+c_{12}} \tag{3.15}$$

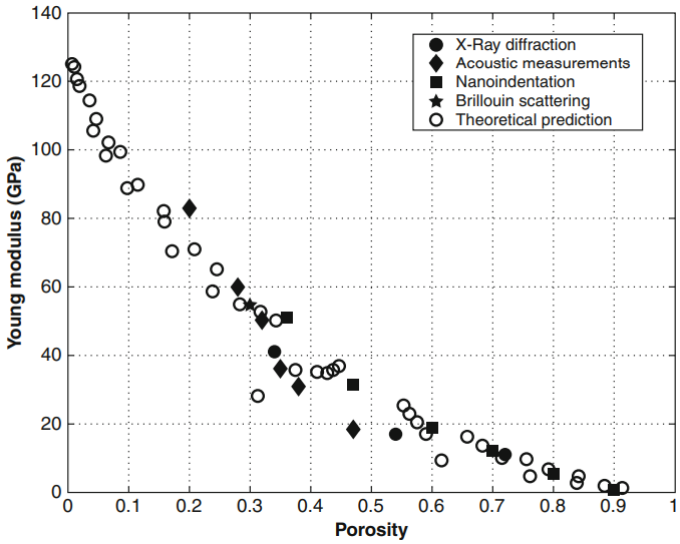

Figure 3.16: Numerical results for the Young modulus obtained for different porosities and experimental results from different sources. Extracted from [85].

One technique that allows estimating the Young's modulus of porous silicon, and, thus, quantify its stiffness, is nanoindentation. This technique relies on indenting a material of interest whose mechanical properties are unknown with another material whose properties are known, trough a nanometric penetration depth. The major goal of nanoindentation testing is to extract elastic modulus and hardness of the specimen material from experimental readings of indenter load and depth of penetration. In a typical test, the force and depth of penetration are recorded from zero to a maximum load, and then upon unloading back to zero. When load is removed from the indenter, the material tries to go back to its original shape, however, due to plastic deformation, it is prevented from doing so. Nevertheless, a degree of recovery is observed due to the relaxation of elastic strains within the material [86].

Figure 3.17 shows a schematic representation of the load versus displacement curve obtained for a nanoindentation experiment. There are four main values that must be measured from the load-displacement curves: the maximum load, P_{max}; the maximum displacement, h_{max}; the final depth, *i.e.,* the permanent depth of penetration after the indenter is fully unloaded , h_f, and the elastic unloading stiffness, S=dP/dh, defined as the slope of the upper portion of the unloading curve during the initial stages of unloading (also called the contact stiffness) [87]. Futhermore, by knowing the depth of penetration and the geometry of the indenter, the area of contact at full load, A_c, can be indirectly measured. Finally the indentation modulus and hardness can be calculated by equations 3.16 and 3.17, respectively [86].

$$E^* = \frac{1}{2}\frac{\sqrt{\pi}}{\sqrt{A_c}}\frac{dP}{dh} \tag{3.16}$$

$$H = \frac{P}{A_c} \tag{3.17}$$

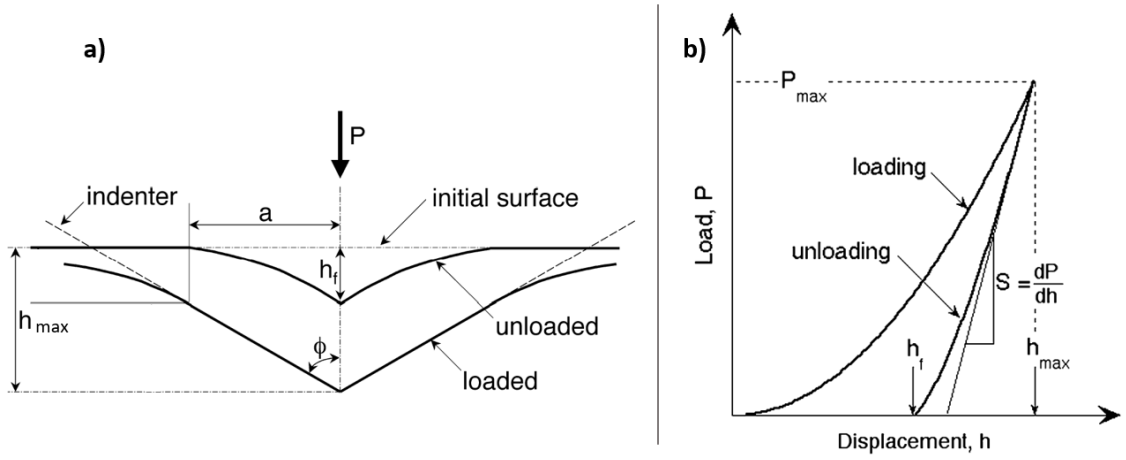

Figure 3.17: Schematic illustrations of nanoindentation's (a) unloading process showing parameters characterizing the contact geometry, and (b) load–displacement curve. Adapted from [87].

Calculation of the hardness and modulus requires the knowledge of the contact stiffness at load, which implies that these quantities can only be known at the maximum indetation depth. Since several years, the so-called continuous stiffness measurement (CSM) allows to superimpose a small oscillation on the loading curve, such that small unloads are performed continuously. Hence with a single indent modulus and hardness can be extracted for all depths until maximum indentation depth. Furthermore, the indirect measurement of the contact comes from a geometrical relation [88]:

$$A_{\mathrm{c}} = \pi \left(\tan(\theta) h_{\mathrm{c}}\right)^2 \tag{3.18}$$

where θ is is the equivalent angle of the conical indenter (for a Berkovich tip, θ= 70.32 °), and h_c is the contact depth. The calculation of the actual contact depth is very difficult because the relation between the contact depth (h_c) and the indentation depth (h) is influenced by measurement uncertainties (thermal drift, tip defect, etc.) and by material pileup or sink-in around the indent during the test. However, a lot of methods can be used to precisely determine this relation [88]. In the present case, the Oliver and Pharr model [89] is used, and it defines the contact depth as:

$$h_{\mathrm{c}} = h - \varepsilon \frac{P}{S} \tag{3.19}$$

where ε is a constant depending on the indenter geometry, equal to 0.75 for the indentations performed in this work.

The mechanical properties of PSi membranes were investigated by nanoindentation measurements performed on the XP head of an Agilent G200 nanoindenter equipped with a Berkovich diamond tip, the samples were glued to the support. The tip area function is calibrated by means of indentation in a reference material of known modulus (fused silica, E = 72 GPa). The continuous stiffness measurement mode (CSM) has been used at 45 Hz frequency with the harmonic displacement set to 2 nm. The strain rate was set to 0.05 s^{-1}. In order to reduce discrepancy, at least 16 indents were performed on each sample. Penetration depth was limited to 2 μm.

Resistance to flow analysis

In order to determine if the membranes are clogged or not, the resistance flow was measured by using an electrode integrated flow cell, as proposed by Ref. [90], as shown in figure 3.18. Each side of the membrane was put in contact with an NaCl solution, one with 1 M NaCl concentration and another 0.1 M NaCl concentration.

The current between the two electrodes was measured with a Keitley sourcemeter (0.005 mV noise level in tension). The current measured allows evaluating the resistance to flow: a high resistance to flow (clogged membranes) will lead to a low measured current and a low resistance to flow (unclogged membranes) will lead to a high measured current.

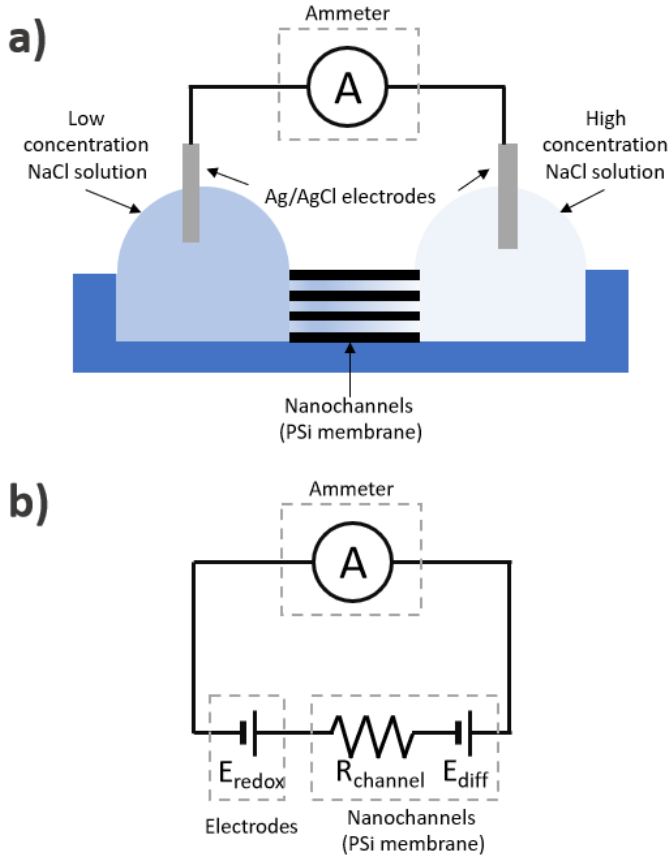

Figure 3.18: Electrode integrated flow cell: a) Schematic diagram. b) Equivalent circuit for the experimental setup. E_{redox}, E_{diff}, and $R_{channel}$ are the potential generated from redox reactions on the electrodes, the diffusion potential of the nanochannels, and the electric resistance of the nanochannels, respectively. Adapted from [90].

3.2.7 Optical stability measurements

For the stability measurements, the sample is placed inside a polycarbonate fluidic cell (figure 3.19) with a continuous flow of phosphate buffered saline (PBS, 0.01 M phosphate,

pH 7.4) for 240 min, using a Fluigent LINEUP^{TM} fluidic. The PBS was as purchased from Sigma-Aldrich (USA). PBS was chosen as a model buffer since biological interactions mostly take place in aqueous media at physiological pH.

Reflective interferometric Fourier transform spectroscopy (RIFTS) is used to evaluate the effective optical thickness (EOT) over time. A fiber coupled Ocean Optics JAZ spectrometer and a 10-mW halogen light source were used to record reflectivity spectra. The spectra are acquired over time (one spectrum every 10 s, with an integration time of 2000 ms and an average of five scans to minimize the noise), and the Fabry-Pérot fringes are then processed using a Fourier transform to obtain the $EOT = 2nL$, with n being the average refractive index of the porous layer in PBS and L being its thickness. The first 6 scans (first minute) are averaged to obtain EOT_0, the initial $2nL$ of the studied sample. The evolution over time of the effective optical thickness, *EOT(t)*, is then computed as a percentage change relative to EOT_0, as defined in equation 3.20.

$$\Delta EOT = \frac{EOT(t) - EOT_0}{EOT_0} \times 100[\%] \tag{3.20}$$

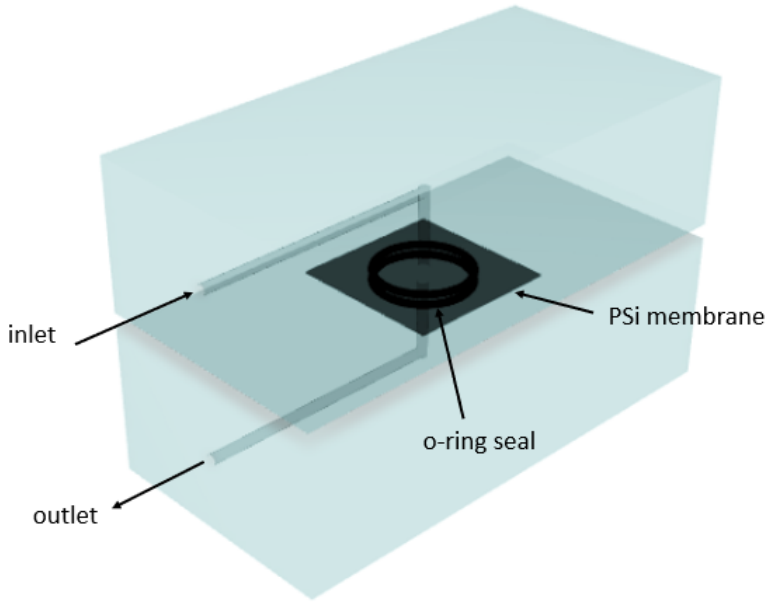

Figure 3.19: Schematic of the flow-through polycarbonate fluidic cell used for stability measurements.

3.2.8 Noise and limit of detection

The optical data was also analyzed, in parallel to the stability assessment, to evaluate the noise level related to the measurements following the RIFTS data processing. This was done through a fit using a moving average (lowpass filter with filter coefficients equal to the reciprocal of the span, $span = 0.15$) on the ΔEOT versus time data, and the difference between the actual data and the fit was computed. The mean and the standard deviation were computed for each stability measurement. Then, the noise level was determined,

as the average of the standard deviation, σ_N, for each sample of a given type (SiO_2, HfO_2, TiO_2 and Al_2O_3). Finally, the theoretical limit of detection (LoD) was calculated according to equation 3.21 [91].

$$LoD = 3\sigma_N \tag{3.21}$$

3.3 Results and discussion

3.3.1 Porous silicon membranes characterization

Porosity, thickness, pore morphology and optical signal

The passivated membranes, either by oxidation at 200 °C, or by atomic layer deposition of HfO_2, TiO_2 or Al_2O_3, as described above, were characterized by SEM and SLIM.

The porosity and thickness are computed via the Bruggeman effective medium approximation. For this approximation, the refractive index of the skeleton that makes up the porous material, $n_{skeleton}$, is needed. In order to calculate this index for the different passivation methods, the following procedure was adopted:

1. A few freshly etched porous silicon membranes (before backside etching) were characterized using the RIFTS method and their EOTs in air and ethanol were obtained;

2. The same membranes had their thickness measured through SEM;

3. Knowing the thickness and the EOTs, it was possible to obtain the freshly etched PSi $n_{skeleton} = 3.1$;

4. The EOTs in air and ethanol of all other freshly-etched membranes (before backside etching) were taken through RIFTS. This information was used to calculate the thickness and porosity using $n_{skeleton} = 3.1$ [3];

5. The membranes were characterized after oxidation and the different atomic layer depositions to obtain their EOTs in air and ethanol.

6. The thickness obtained after electrochemical etching remains constant after the different passivation treatments, as observed by Ref. [3]. Therefore, these values were used to estimate the $n_{skeleton}$ for the $SiO2$, HfO_2, TiO_2, and Al_2O_3.

Once the $n_{skeleton}$ values are known, the porosity and thickness could be estimated for all membranes after passivation, using the SLIM method. The results are shown in table 3.9. The parameters can only be evaluated for the first layer (sensing layer) for two main reasons: the second and third layers are too thick to allow the reflected light to reach the surface with sufficient intensity to be measured, and in membranes, the reflected light has lower intensity due to partial transmission, also making measurement harder.

[3] Since more than 150 membranes were produced during this project, it would have been unpractical to measure all thicknesses using SEM. That is why the SLIM method was used for this purpose.

The thickness of different membranes was measured from SEM images after oxidation ($PSiO_2$) and 3.60 ± 0.35 μm was obtained. This value is in good agreement with the thickness estimated through the SLIM method, 3.66 ± 0.35 μm. SEM images also allow measuring the contrast layer and the support layer, 16.07 ± 2.33 μm and 82.88 ± 12.78 μm, respectively. The high standard deviation between measurements can be attributed to the difficulty in visualizing the transition between the different layers, as shown in figure 3.20.

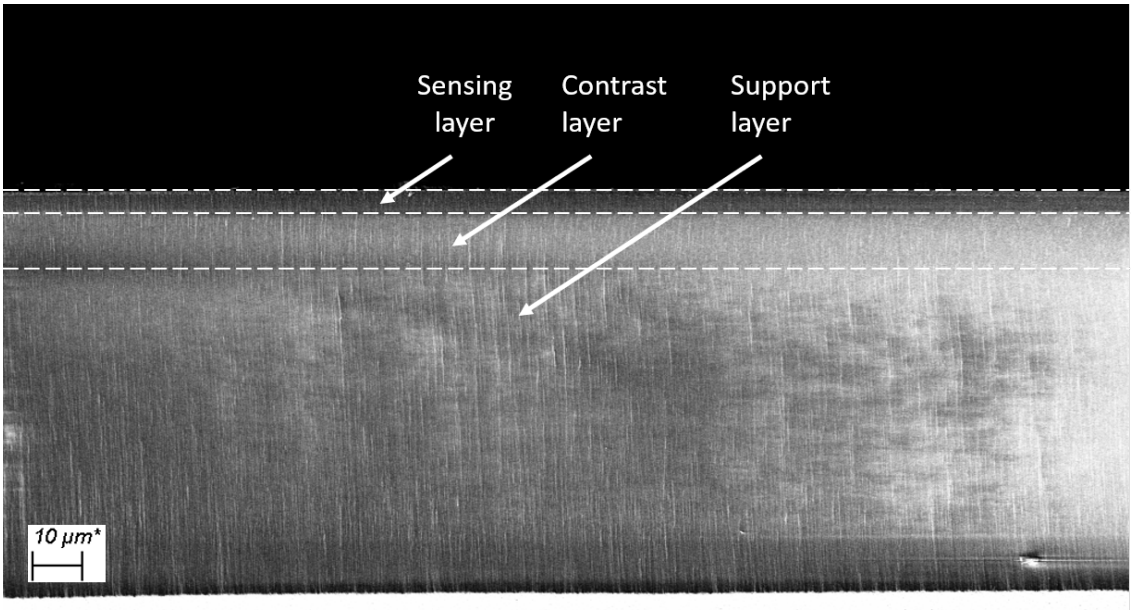

Figure 3.20: SEM cross-section image of a multi-layered porous silicon membrane. Three distinct layers can be identified, but the position of the transition is estimated.

Table 3.9: Thickness, open porosity, $n_{skeleton}$ of passivated PSi membranes, evaluated by the SLIM method. Pore size and average pore density were evaluated through SEM image analysis.

	SLIM			**SEM**	
	Thickness [μm]	Open porosity [%]	$n_{skeleton}$ [-]	pore size [nm]	average pore density [μm^{-2}]
$PSiO_2$	3.66 ± 0.35	74.7 ± 5.8	2.52 ± 0.17	30.3 ± 14.8	385.7 ± 86.0
$PSiO_2/HfO_2$	3.67 ± 0.21	56.9 ± 4.5	2.38 ± 0.20	26.4 ± 14.0	240.9 ± 44.3
$PSiO_2/Al_2O_3$	3.56 ± 0.21	62.4 ± 4.7	2.09 ± 0.17	23.2 ± 12.0	388.4 ± 55.0
$PSiO_2/TiO_2$	3.60 ± 0.13	62.1 ± 6.1	2.57 ± 0.25	25.5 ± 11.4	437.0 ± 29.2

When comparing the porosity of the samples before and after ALD of metal oxides, a large decrease of porosity is observed. As previously discussed, SLIM method allows measuring the open porosity. Therefore, the large decrease in porosity can be attributed to the closure of the top part of smaller pores during the metal oxide deposition and

thus the creation of closed porosity, which is not accessible to ethanol. It has been pointed out that liquids, in general, may be excluded from the pores due to physical closing (sintering and pore fusion that occurs during the ALD), or due to the surface tension of the liquid that may be too high to adequately wet or infiltrate the smallest pores [92].

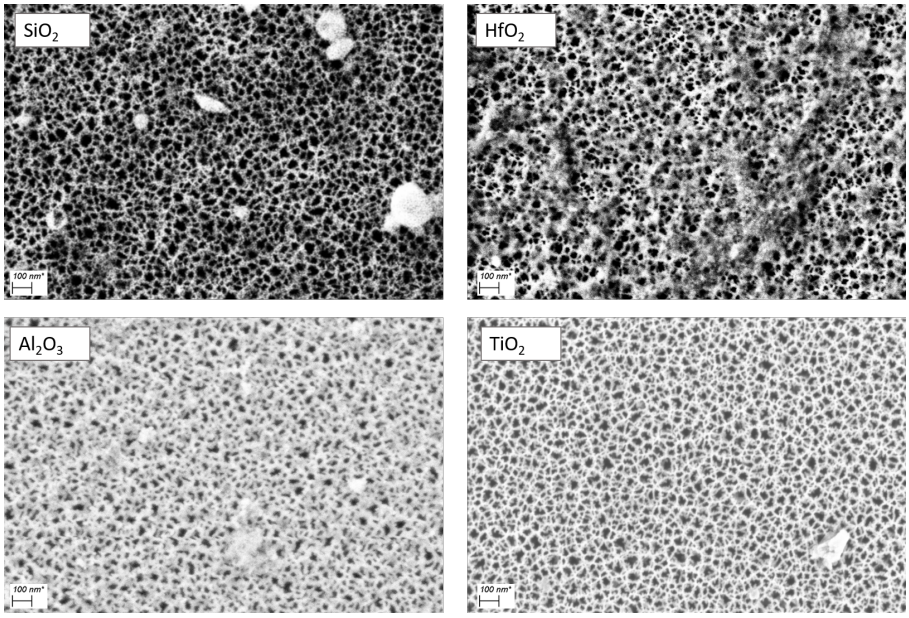

Figure 3.21: SEM images of the surface of porous silicon membranes: $PSiO_2$, $PSiO_2/HfO_2$, $PSiO_2/Al2O_3$ and $PSiO_2/TiO_2$.

The SEM images from the top layer, shown in figure 3.21, confirm the porosity decrease observed through the SLIM results. A MATLAB routine was used to analyze the images and extract data regarding the average pore density as well as their average diameter, as fully described in Ref. [3]. The average pore density for $PSiO2$ (porous silicon oxidized) is estimated to be 385.7 pores/μm^2, and this value does not change much for Al_2O_3 deposition, 388.4 pores/μm^2 , indicating a conformal deposition. For the HfO_2 deposition, a decrease to 240.9 pores/μm^2 is observed, indicating the closure of the smaller pores. Indeed, it has been shown that the micropores are the first to be closed in ALD, due to conformal deposition, and that the surface area decreases gradually after the micropores coverage, indicating a steady decrease in pore size for the mesopores [93]. Furthermore, the evaluated pore size indicates that all samples are in the mesoporous range.

For TiO_2, the average pore density appears to increase, up to 437.0 pores/μm^2, which does not make sense since the material is deposited on the top of the pore walls. However, SEM image analyzing is very susceptible to image quality and charging effect. Indeed, when high-energy beams land on an insultaing material (such as metal oxides) electrons are trapped and a local electrical potential is formed that can modify the microscopy around the irradiated spot of the sample, the so called charging effect, leading to distortion and abnormal contrast in micrographs, undesirable and unpleasant view of the images, shift of spectra, and other unusual phenomena [94]. The difference in image quality between the samples makes it hard to establish any reliable comparisons.

Additionally, silicon wafers were introduced in the deposition chamber during ALD and thickness of the oxide deposited was measured on top of the samples by ellipsometry to assess the quantity of oxide deposited on and inside the porous layers. Thicknesses of 2.85 nm, 3.22 nm and 3.59 nm were measured for HfO_2, Al_2O_3 and TiO_2. The number of cycles was adjusted to obtained an uniform thickness between the different depositions, thus, 20 cycles, 40 cycles and 50 cycles were performed for HfO_2, Al_2O_3 and TiO_2, respectively. The grow per cycle is estimated to be to be 1.425 Å/cycle, 0.805 Å/cycle and 0.718 Å/cycle for HfO_2, Al_2O_3 and TiO_2, respectively. However, these results are subjected to error, because the ellipsometry measurement is based on a determined density, but this value might be different from the actual density of the layer due to the low temperature adopted for deposition. Moreover, deposition on different materials, bulk silicon and $PSiO_2$, can also change the growth mechanisms, hence the first few nanometers may have a different GPC. Furthermore, from figure 3.21, it appears that the highest deposited thickness can be attributed to Al_2O_3 and the lowest to TiO_2, while the ellipsometry results suggest otherwise.

Some porous silicon samples were also fabricated and imaged using SEM to evaluate the pore morphology. The mesopores are expected to have a branched morphology [84], as schematically shown in figures 3.22.a. and 3.22.b. This morphology was observed in the microscopy images and are shown for the sacrificial (figure 3.22.c.), sensing and contrast layers (figure 3.22.d.).

The optical signal intensity of the interferometric spectra was also evaluated on the Fabry-Pérot fringes region (wavelength range of 400-800 nm). The ALD of metal oxides provided signal enhancement, as shown in figure 3.23. This was attributed to the fact that the relative permittivities (or dielectric constants) of the metal oxides (9 for Al_2O_3, 80 for TiO_2 and 25 for HfO_2, approximate values) are superior to the one of $SiO2$, approximately 3.9 [95], thus, the reflectance is enhanced by the metal oxides and the signal is, therefore, increased.

Membranes passivation

As previously discussed, to ensure that no silicon is in contact with the buffer solution during detection, and prevent its oxidation/dissolution, the ALD needs to provide a uniform (or conformal) coverage inside the pore walls. To evaluate the metal oxides coating, $PSiO_2/HfO_2$, $PSiO_2/TiO_2$ and $PSiO_2/Al_2O_3$ membranes were observed in cross section by SEM and the chemical composition of the porous layers was characterized by EDX. Three zones were initially evaluated to assess the uniformity of the deposition: top, middle and bottom, as shown in figure 3.24.

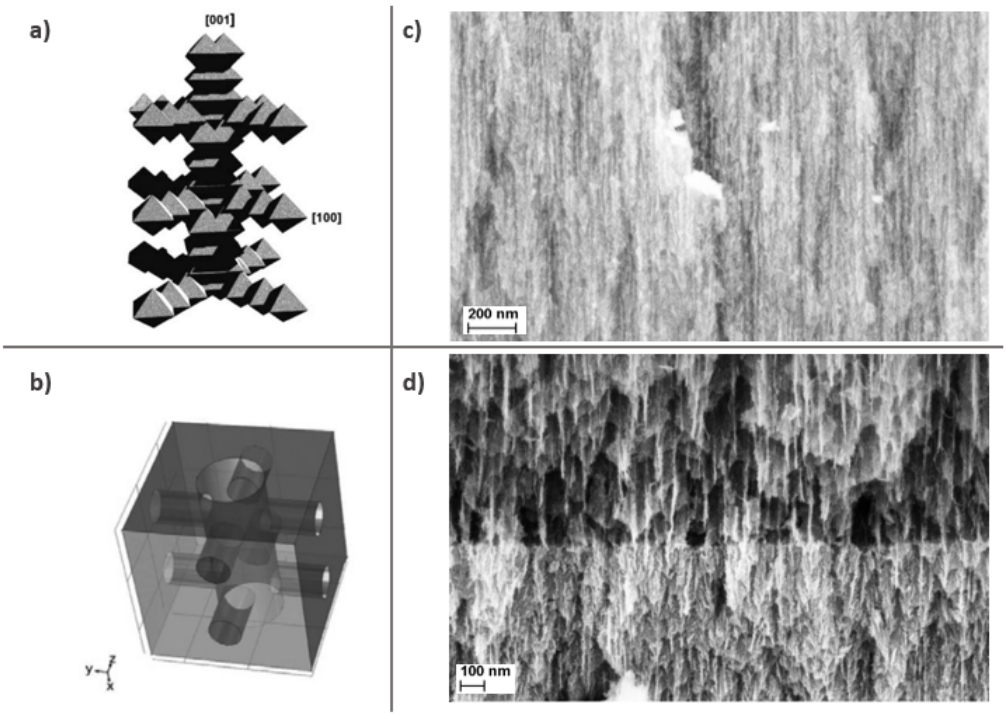

Figure 3.22: Branched pore morphology: (a) schematic view of a mesopore [84], (b) morphological models implemented in a FEM simulation [83], (c)SEM image of sacrificial layer, etched at 200 mA/cm2, (d) SEM image of sensing layer, top, etched 200 mA/cm^2, and contrast layer, bottom, etched at 50 mA/cm^2.

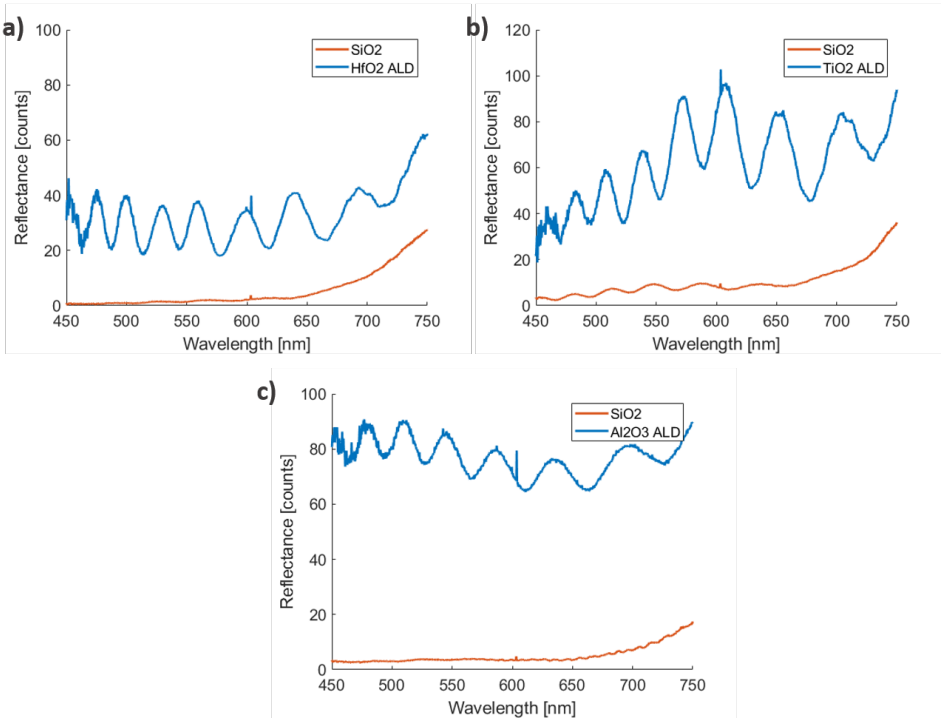

Figure 3.23: Interferometric spectra obtained for (a)$PSiO_2/HfO_2$, (b)$PSiO_2/TiO2$, and (c)$PSiO_2/Al_2O_3$, before and after the ALD, at same integration time ($\Delta t = 1s$).

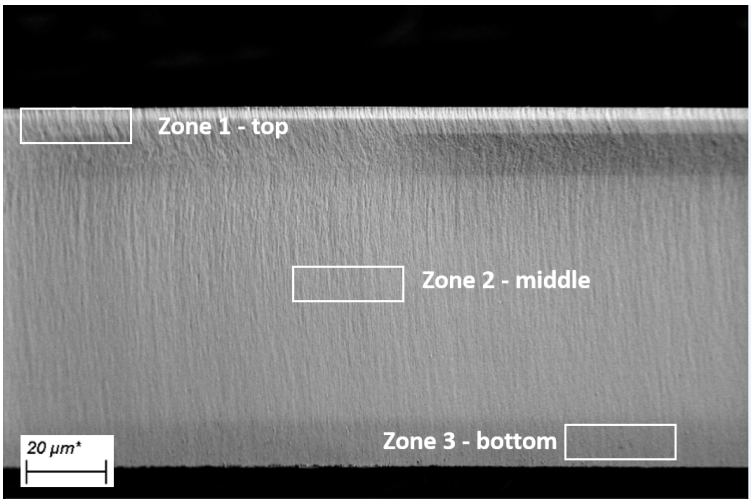

Figure 3.24: SEM image showing the zones defined for EDX analysis.

The $PSiO_2/HfO_2$ EDX spectra for the three zones are shown in figure 3.25. As expected, the peak corresponding to the Kα band of oxygen, at 0.525 keV, can be easily observed. Some aluminium contamination at the Kα band, 1.486 keV, is also observed, probably due to the backside hard mask used for DRIE. Hafnium is represented by two peaks, 7.898 keV (Lα) and 1.644 keV (M), and the silicon Kα band is at 1.739 keV. It can be seen, that the Lα band from Hf and the Kα band from Si overlap in the spectra. Furthermore, the peak is more dislocated to the Hf Lα band for the top layer, to the Si Kα band for the bottom layer and split between the two for the middle layer. This observation suggests that the deposition is generally uniform, covering the whole membrane, but some material may accumulate on the top layer. When zooming on the 1.644 keV (M) peak, one can see that the signal loses intensity through the membranes depth but Hf is, nevertheless, present from top to bottom. To evaluate the deposition though the entire depth, a line scan was performed, as shown in figure 3.28.a. for $PSiO_2/HfO_2$. The signal intensity is slightly higher for the top and bottom of the membrane, which is expected since the membranes where lifted inside the chamber to allow precursor flow from both sides.

Results for $PSiO_2/TiO_2$ are shown in figures 3.26 and 3.28.b. The Kα band for silicon (1.739 keV) can be clearly distinguished. Some aluminium contamination can be seen (Kα, 1.486 keV,), as observed for $PSiO_2/HfO2$. The titanium is also represented by two peaks 4.508 keV (Kα) and 0.452 keV (Lα), and the oxygen Kα band is at 0.525 keV. An overlap can be seen between the signal from Ti (Lα) and O (Kα). The second peak for Ti can be clearly distinguished at 4.508 keV (Kα), and, upon amplification, signals of similar intensity can be seen for the top and middle layer, but no signal is comes from the bottom layer. The line scan in figure 3.28.b., shows an uniform deposition until a steep decrease at 50 µm depth, followed by an increase after 75 µm depth. This behaviour is probably an artifact, because the sample cutting is not perfect, resulting in a non flat cross section.

All peaks can be clearly distinguished in the $PSiO_2/Al_2O_3$ EDX spectra, shown in figure 3.27. The Kα bands for silicon, oxygen, and aluminium are located at 1.739 keV, 0.525 keV and 1.486 keV, respectively. The aluminium signal is higher for the top layer, but also present in the middle and bottom layers. The line scan is shown in 3.28.c., a

higher signal can be seen on the top and on the bottom, as expected, and the metal oxide is present through the whole depth.

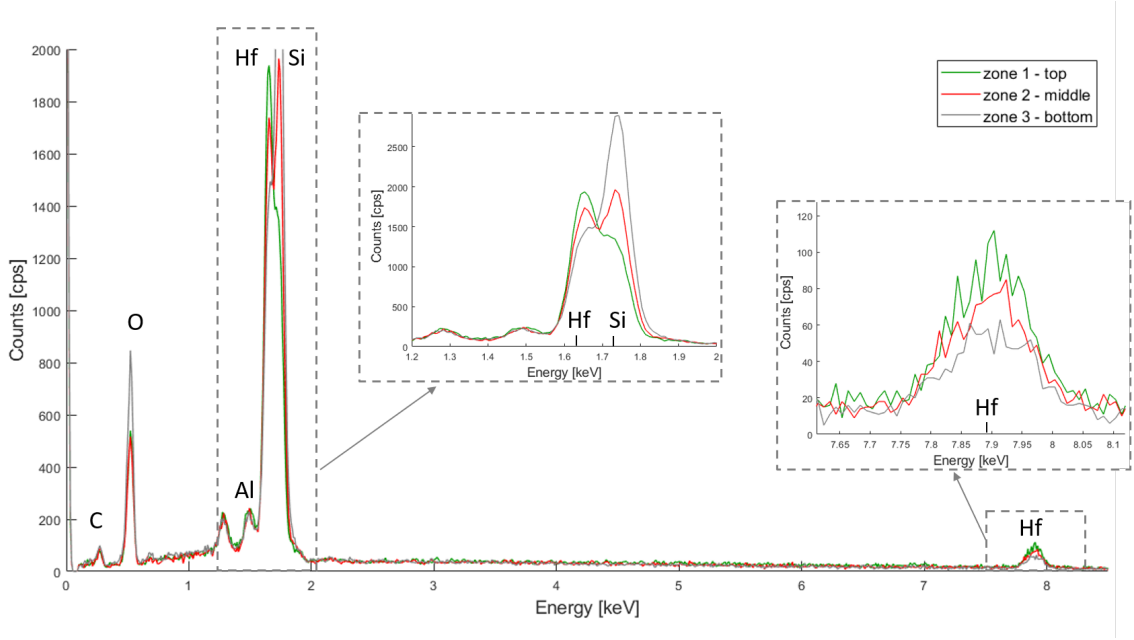

Figure 3.25: $PSiO_2/HfO_2$ EDX spectra for the top, middle and bottom of the porous membrane.

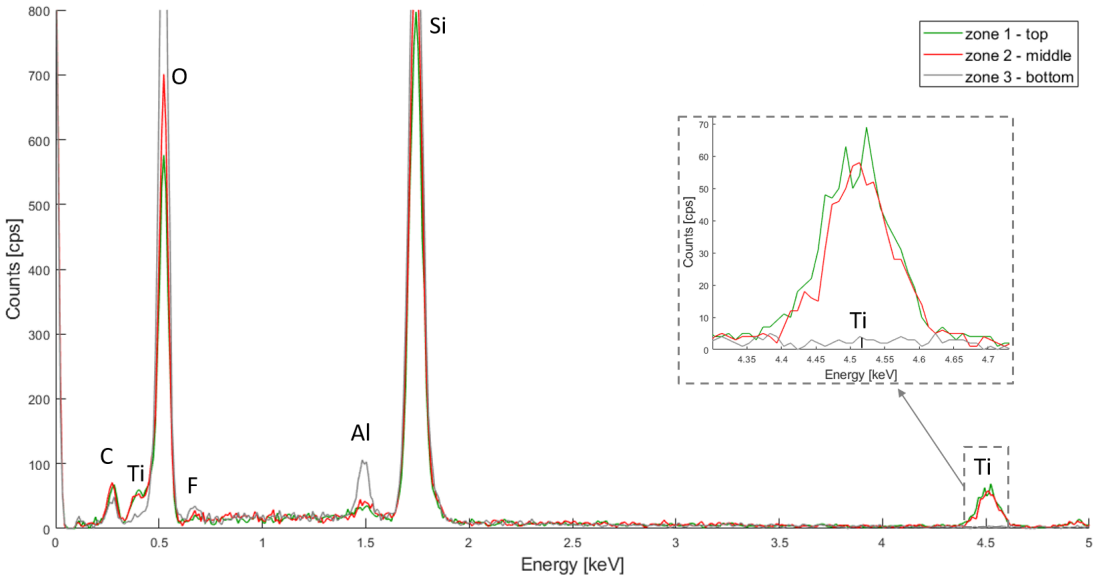

Figure 3.26: $PSiO_2/TiO_2$ EDX spectra for the top, middle and bottom of the porous membrane.

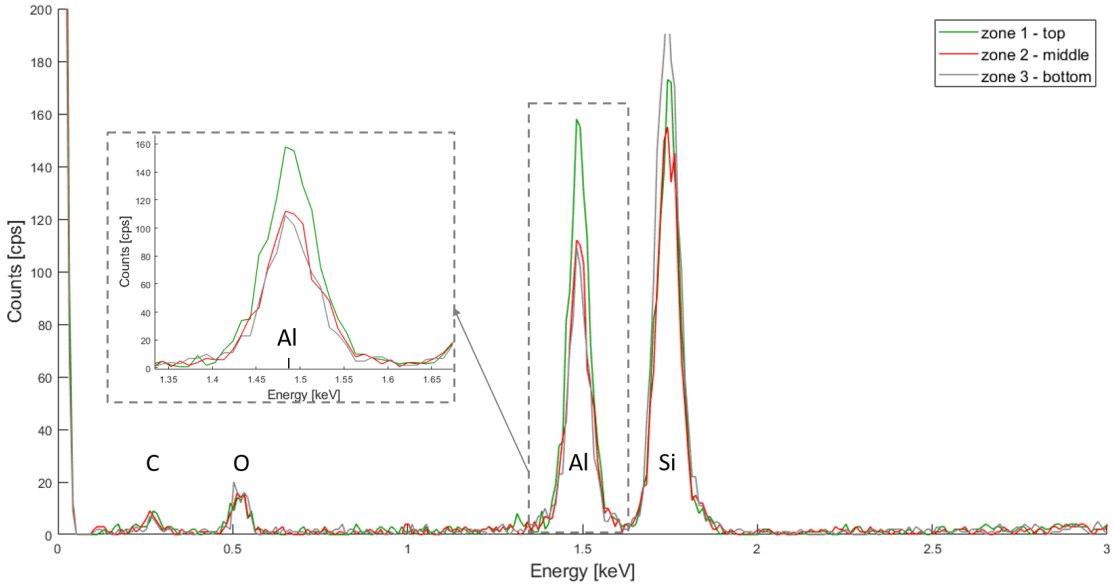

Figure 3.27: $PSiO_2/Al_2O_3$ EDX spectra for the top, middle and bottom of the porous membrane.

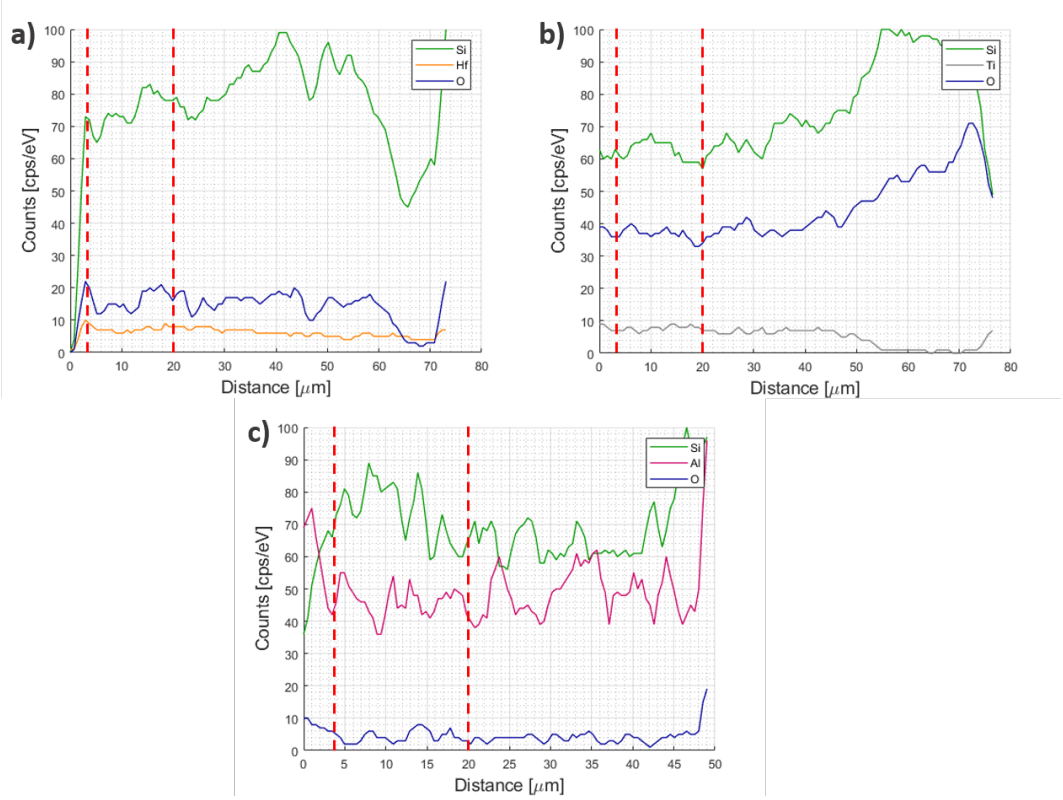

Figure 3.28: EDX line scan showing deposition on the full depth of the membrane: (a)$PSiO_2/HfO_2$, (b)$PSiO_2/TiO_2$, (c)$PSiO_2/Al_2O_3$. The red dotted lines indicate the approximate location of the interfaces between first/second and second/third layers.

In order to determine the chemical composition of the membrane surfaces, XPS measurements were performed for each type of deposition ($PSiO_2/HfO_2$, $PSiO_2/TiO_2$, and $PSiO_2/Al_2O_3$). The XPS survey spectra for $PSiO_2/HfO_2$ are presented in figure 3.29. The spectra taken on the front and the back present mainly Hf, O, and C but also Si, F, and P. The presence of fluorine could be explained by contamination due to the DRIE of the backside, and the phosporus signal comes from an unknown source of contamination. When comparing to the backside, the fluorine concentration increases from 7.0% on the front to 20.3 % on the back, revealing the presence of the C_4F_8 passivation layer. Furthermore, the signal from the backside does not come only from the membrane. Indeed, due to the large spot size available for XPS analysis, and the distance of the back of the membrane from the back of the wafer (about 300 μm), the photoelectrons analyzed may come also from the sidewalls of the etched backside. This imprecision would explain the fluorine presence, because this material is deposited on the sidewalls, as a consequence of the Bosch process (see section 3.2.4).

The $PSiO_2/HfO_2$ survey spectrum on the front indicates many peaks at 17 eV, 99 eV, 102 eV, 134 eV, 285 eV and 685 eV which correspond to the binding energy of Hf 4f, Si 2p, P 2p, C 1s, O 1s, and F 1s, respectively. Figures 3.32.a. and b. show the Hf 4f spectra for the front and the back of the membrane. After curve fitting, two peaks are observed at 17 eV and 19 eV which correspond to the binding energies of Hf $4f_{7/2}$ and Hf $4f_{5/2}$, respectively, indicating a valence state of +4 for hafnium. These results indicate that the product after the ALD process is HfO_2.

The survey spectrum on the back indicate peaks at similar places. Furthermore, curve fitting of the C 1s peak, showed a peak at 292 eV, attributed to C-F_2, C-F_3 bonds. The same procedure was applied to the F 1s peak, peaks at 685 eV and 689 eV were obtained and attributed to F^-/ F-Me and F-C bonds, respectively. These observations corroborate the hypothesis that the fluorine contamination comes from the C_4F_8 passivation layer.

The XPS survey spectra for $PSiO_2/TiO_2$ are presented in figure 3.30. The spectra taken on the front and the back present mainly Ti, O, and C but also Si, and F. The presence of fluorine is probably from the same contamination source discussed before. The survey spectrum on the front indicates many peaks at 103 eV, 283 eV, 459 eV, 533 eV, and 689 eV which correspond to the binding energy of Si 2p, C 1s, Ti 2p, O 1s, and F 1s, respectively. Peaks at similar positions are seen on the back. The Ti 2p spectra from the front and the back are shown in figures 3.32.c. and d. The amplification of the Ti 2p spectra reveals two peaks at 459 eV and 464 eV, attributed to Ti $2p_{3/2}$ and Ti $2p_{1/2}$, respectively, also indicating a valence state of +4 for titanium. Once again, the desired product TiO_2 is obtained after ALD.

Finally, the XPS survey spectra for $PSiO_2/Al_2O_3$ are presented in figure 3.31. Both front an back spectra indicate the presence of mainly Al, O, and C, but also F contamination. The survey spectrum on the front indicates many peaks at 74.5 eV, 103 eV, 285 eV, 532 eV, and 686 eV which correspond to the binding energy of Al 2p, Si 2p, C 1s, O 1s, and F 1s, respectively. Similar position peaks are observed on the back. The Al 2p peaks, shown for the front and back in figures 3.32e. and f., indicate a valence of +3 for

aluminium. The ALD also resulted in the desired product for this metal oxide.

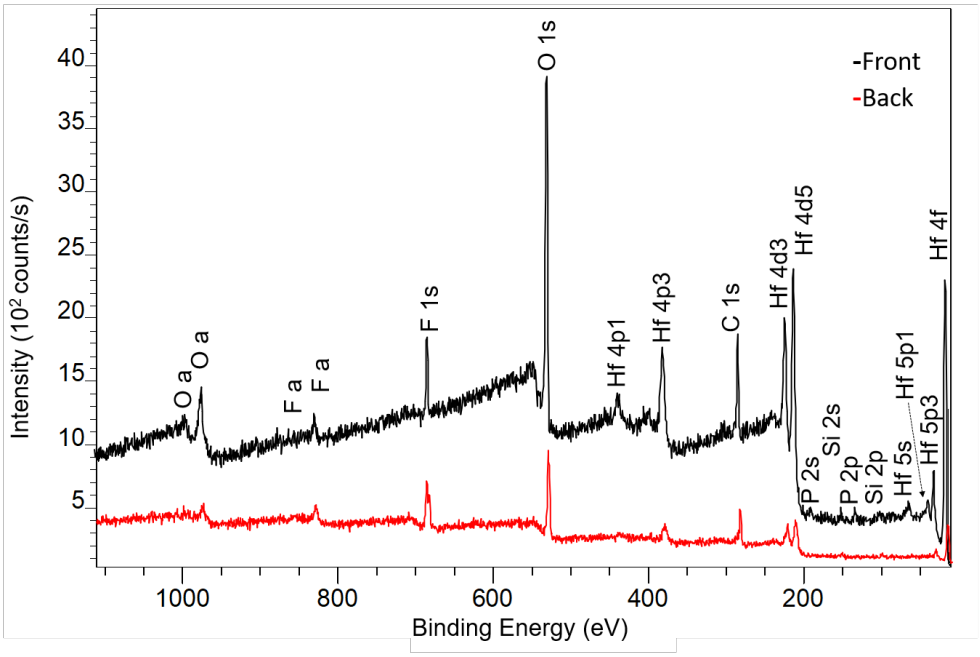

Figure 3.29: XPS survey spectra of the $PSiO_2/HfO_2$ membrane front (black) and back (red). The main core levels are labeled. The data are normalized to each C-(C,H) component of the C 1s peak and separated vertically.

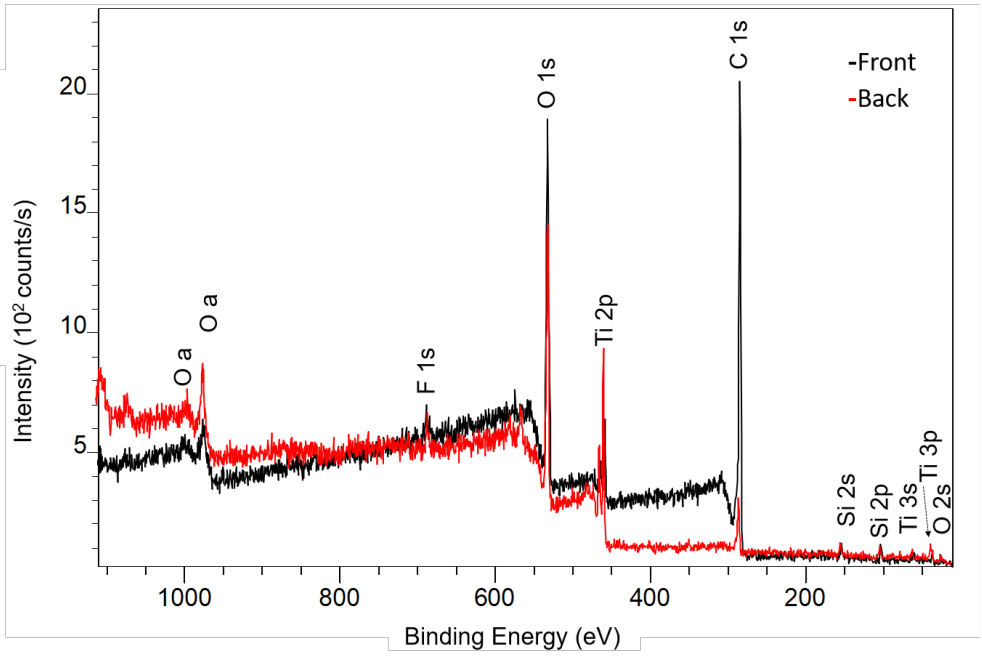

Figure 3.30: XPS survey spectra of the $PSiO_2/TiO_2$ membrane front (black) and back (red). The main core levels are labeled. The data are normalized to each C-(C,H) component of the C 1s peak and separated vertically.

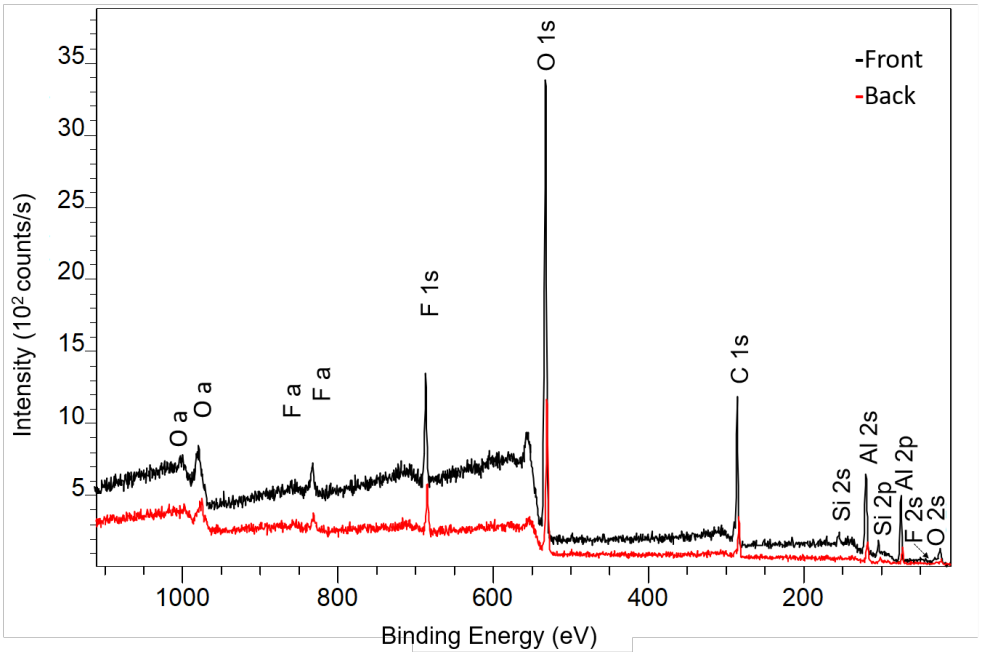

Figure 3.31: XPS survey spectra of the $PSiO_2/Al_2O_3$ membrane front (black) and back (red). The main core levels are labeled. The data are normalized to each C-(C,H) component of the C 1s peak and separated vertically.

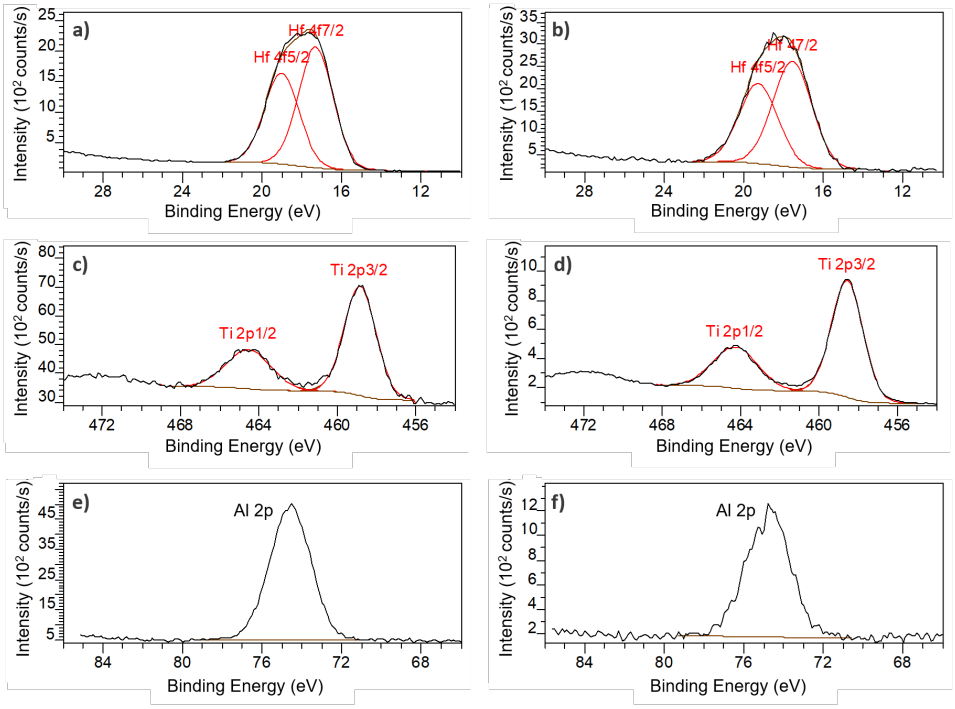

Figure 3.32: High resolution XPS core level spectra: Hf 4f on $PSiO_2/HfO_2$ membrane (a) front, and (b) back; Ti 2p on $PSiO_2/TiO_2$ membrane (c) front, and (d) back; Al 2p on $PSiO_2/Al_2O_3$ membrane (c) front, and (d) back.

Mechanical properties assessment

Nanoindentation trials were performed on the front and the back of the passivated membranes. Figures 3.33.a. and 3.33.b. illustrate the mean evolution of Young's modulus (E) for the front and the back, respectively, as a function of penetration depth for the samples. The mean value was calculated based on all the indents made on each sample. The hardness (H) evolution with the penetration depth is also presented for the front and the back in figures 3.34.a. and 3.34.b. The summarized results are depicted in table 3.10[4]. Since the upper layer (sensing layer) is 4 μm thick, the effect of the stiffer layer (contrast layer) below increases the measured Young's modulus and hardness starting from 0.4 μm indentation depth (1/10 Bückle rule of thumb [96]). Therefore the hardness and Young's modulus values were taken between 0.3 and 0.4 μm depth to avoid the effect of the underlying layer. To be consistent, the values on the back were taken at the same depth.

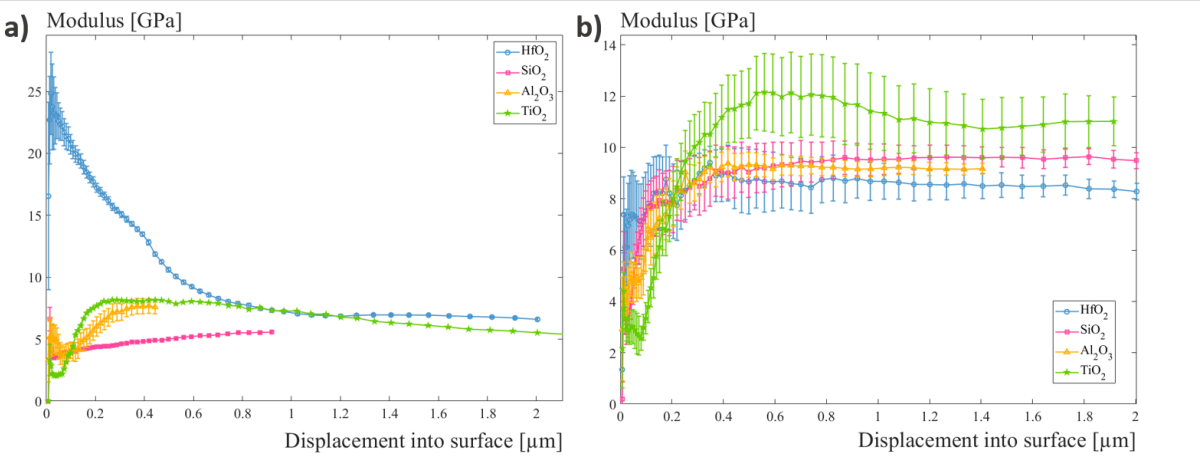

Figure 3.33: Mean Young's elastic modulus with respect to nanoindentation depth of passivated porous silicon membranes. Nanoindents made on (a) front, and (b) back of the samples.

The model proposed, in equation 3.14 [83], to calculate the Young's modulus of porous silicon samples can be used to estimate this property as a function of porosity. For the $PSiO_2$ membrane, the open porosity of the sensing layer can be estimated by the SLIM method and, as previously discussed, and the calculated value is 74.7 %. The value of E'_0 for crystalline silicon equals 130 GPa [83] and it can be estimated to be 57 GPa for silicon dioxide [97]. The degree of oxidation of the porous matrix was not assessed, but to have an idea of the order of magnitude of the expected modulus for the $PSiO_2$ sample, the modulus was estimated using a fully oxidized sample (E'_0=57 GPa) as a lower boundary and a non-oxidized one (E'_0=130 GPa) as an upper boundary. The calculated moduli are 3.1 GPa and 7.2 GPafor the lower and upper boundaries respectively. The measured value through nanoindentation is 4.8 $\pm$ 0.1 GPa which is in between the estimated range. This estimative has its limitations not only due to the unknown degree of oxidation but also because the Young's modulus of SiO_2 changes with the oxidation parameters (wet/dry, temperature, pressure, etc). Furthermore, the model proposed is highly sensitive to porosity changes,

[4]only one indent was made on the $PSiO_2/TiO_2$ front sample due to instrumentation problems.

since $E \propto (1-p)^2$, and the SLIM method only allows measuring the open porosity, while the closed porosity remains unknown but certainly has an impact on the mechanical properties.

Estimating the Young's modulus analytically becomes even harder for the samples that go through ALD, due to the unknown value of E_0'. The nanoindentation results show an increase in the modulus upon metal oxide deposition, for the front analysis, however, it is difficult to determine if this effect is due to the decrease in porosity or to better mechanical properties of the ALD layers themselves. Nevertheless, when comparing the front results with the back ones, it can be seen that the measured Young's modulus increases for the latter, except for $PSiO_2/HfO_2$. This increase could be associate to the lower porosity of the (back) compared to the sensing layer (front). The decrease observed for $PSiO_2/HfO_2$ could be attributed to the observation of an unetched layer of C_4F_8 passivation film from DRIE.

Table 3.10: Hardness and Young's modulus measured through nanoindentation for the passivated PSi membranes

	Front		**Back**	
	Young's modulus [GPa]	**Hardness [GPa]**	**Young's modulus [GPa]**	**Hardness [GPa]**
$PSiO_2$	4.8 ± 0.1	0.42 ± 0.08	9.1 ± 1.0	0.15 ± 0.01
$PSiO_2/HfO_2$	14.3 ± 0.2	0.37 ± 0.10	8.9 ± 1.0	1.13 ± 0.03
$PSiO_2/Al_2O_3$	7.57 ± 0.6	0.31 ± 0.04	9.0 ± 0.6	0.20 ± 0.01
$PSiO_2/TiO_2$	8.1 ± (-)	0.24 ± (-)	11.2 ± 1.3	0.22 ± 0.01

Hardness of a material is usually defined as the resistance to local deformation. The hardness of the non-porus silicon substrate was assessed through nanoindentation and H=12.37 ± 11 GPa was obtained. A model has been proposed for predicting the hardness of porous silicon samples as a function of porosity (p): H=$H_0(1-p)^{2/3}$, where H_0 is the crystalline, non-porous silicon hardness [98]. However, it has been also observed that at 70%-80% porosity, the measured hardness deviates from the proposed proportionality which is linked to large increase in pore size at high porosities, as the pore walls become stand-alone structures and pores coalesce. Since hardness is invertially proportional to the contact area, an increase in surface area results in a decrease in hardness [98]. Therefore, estimating the hardness based on the proposed model is not possible. However, hardness has been measured through nanoindentation for 73% and 79% mesoporous silicon layers (pore size 5-40 nm) and the resulting values were 0.7 GPa, 0.4 GPa , respectively. This study prepared porous silicon from p+ wafers (resistivity of 1–2 × $10^{-2}\Omega$ cm) using 80 and 100 mA/cm^2 to obtain 73% and 79% mesoporous layers, respectively [99]. As described in section 3.2.3 the porous silicon membranes were fabricated from a p++ wafer (resistivity of 0.08–0.09 × $10^{-2}\Omega$ cm) with 250 mA/cm^2 current density for the sensing layer (front) and 100 mA/cm^2 for the support layer (back).

The values of 0.42 ± 0.08 and 0.15 ± 0.01 GPa were obtained for the front and back sides of $PSiO2$ membranes, respectively. The hardness value for the front is within the range proposed by [99], with open porosity of 74.7 %. For the backside, the estimated porosity (based on the fabrication parameters) is 70% but the obtained hardness value is bellow 0.4 GPa measured for 79% porosity by [99]. Some explanations can justify this value difference: first, larger pores are formed at higher current densities, leading to thinner pore walls and a decrease in the mechanical properties; second, the estimated porosity through the SLIM method does not include the closed porosity. For the mentioned reasons, the comparison of the results has its limitations. Even so, all values are in the same order of magnitude. For the backside, hardeness follows the same behavior of Young's modulus, increasing upon ALD deposition. For the front side, a decrease is observed.

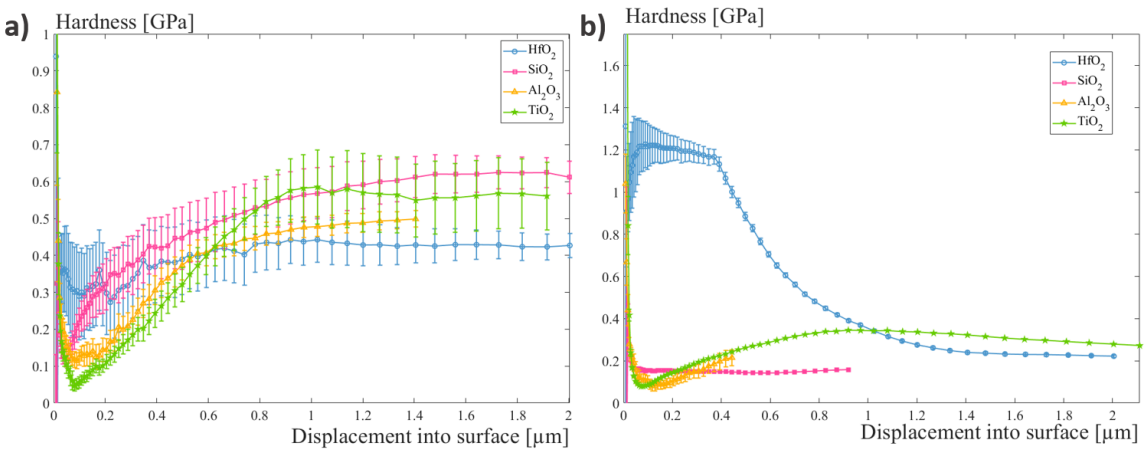

Figure 3.34: Mean hardness with respect to nanoindentation depth of passivated porous silicon membranes. Nanoindents made on (a) front, and (b) back of the samples.

It is important to highlight that nanoindentation of porous silicon comes with its challenges related to a large remanent displacement at the end of the loading–unloading cycle, which can be described as a dislocation-related plasticity. This effect is mainly linked to the crumbling of the cellular structure that can induce compaction of porous silicon upon loading. Therefore the measured elastic response can be influenced by the compacted layer previously created under the indenter, leading to an overestimation of the Young's modulus [82]. Nevertheless, the observed behavior suggests that ALD can improve the mechanical properties of the porous matrix, but further investigation is needed to determine precisely to which extent the deposition is responsible for the improved parameters and the reasons behind the unexpected behaviors for the exceptions mentioned.

Resistance to flow analysis

The current was measured in short-circuit (by connecting the two electrodes) and the obtained values are depicted in table 3.11. The measured current for the $PSiO_2$ membrane was the highest, as expected. Indeed, the sensing layer porosity of the membranes before ALD is 74.7%, as measured by the SLIM method, thus, a lower resistance to flow is expected. As the porosity decreases upon ALD to 56.9%, 62.4% and 62.1% for $PSiO_2/HfO_2$ (20 ALD

Table 3.11: Current measured in the electrode integrated flow cell in short-circuit for the passivated PSi membranes

	Short-circuit current
$PSiO_2$	5.1 μA
$PSiO_2/HfO_2$	0.04 μA
$PSiO_2/Al_2O_3$	3.21 μA
$PSiO_2/TiO_2$	3.3 μA

cycles), $PSiO_2/Al_2O_3$ (40 ALD cycles), and $PSiO_2/TiO_2$ (50 ALD cycles), respectively, the measured current also decreases. The current measurements showed that the ALD indeed leads to an increase in the resistance to flow which follows the decrease in porosity and pore size. The $PSiO_2/HfO_2$ (20 ALD cycles) membrane exhibited a short-circuit current very inferiors to the other membranes, suggesting that either the pores are a lot smaller or that more pores are clogged. Additionally, another $PSiO_2/HfO_2$ membrane was tested after undergoing 40 ALD cycles (45.66 $\pm$ 2.30% evaluated through SLIM method), and no current was measured above the noise level, leading to the conclusion that pores are too small to allow ionic flow.

3.3.2 Stability in aqueous media

The optical readout stability of the porous membranes in a flow of PBS is assessed over a period of 240 min. The stability is characterized by the relative EOT over time, $(EOT - EOT_0)/EOT_0$ %, where EOT_0 is the average of the EOTs taken during the first minute of the experiment. Figure 3.35 illustrates the observed behavior for the changes in the relative EOT as a function of time for $PSiO_2$, $PSiO_2/HfO_2$, $PSiO_2/Al_2O_3$, and $PSiO_2/TiO_2$ membranes. Stability tests were performed for five membranes of each type and the results were averaged to obtain the general behavior.

An increase in EOT is observed for $PSiO_2/TiO_2$, up to +0.19% (after 135 minutes) and $PSiO_2$ up to +0.44% (after 240 minutes) which is an unexpected result. The literature has mainly reported a decrease in the EOT due to oxidative degradation or dissolution of the porous matrix, resulting in a decrease in the value of the refractive index (n) [100]. However, the stability for porous silicon membranes is not a topic that has received attention during the past years, the majority of the studies only review this topic for close-end porous silicon matrices [68, 100, 101, 102]. Therefore, the increase in optical thickness observed could be related to mechanical instability of the membranes when subjected to pressure, being a possible consequence of deflection. When observing the curve for $PSiO_2/TiO_2$, one can see that the membrane is stable until around 15 minutes, staying in a plateau, a steep increase in EOT is observed, up to +0.135% at 50 minutes, and then stability is reached again, with an EOT increase up to +0.190% (135 minutes) and then down to +0.143% (240 minutes) . This behaviour may be related to a gradient liquid penetration into the different membrane layers and, once the membrane is completely wet, a more stable behaviour is observed.

The steep change in the EOT is also observed for $PSiO_2/Al_2O_3$ that presents a fast relative EOT decrease in the first 10-15 minutes, down to -0.28% and then a more stable behaviour that decreases only down to -0.38% . A gradual decrease is observed for $PSiO_2/HfO_2$ through the whole test, down to -0.22% after 240 minutes.

The test in PBS showed that the atomic layer deposition of metal oxides improves the membranes chemical stability in all cases. If the transition zones are neglected, namely the first 10-15 minutes for $PSiO_2/Al_2O_3$ and the first 50 minutes for $PSiO_2/TiO_2$, the relative EOT change is only of -0.08% (after 240 min) and of +0.05% (after 135 minutes), for each membrane respectively.

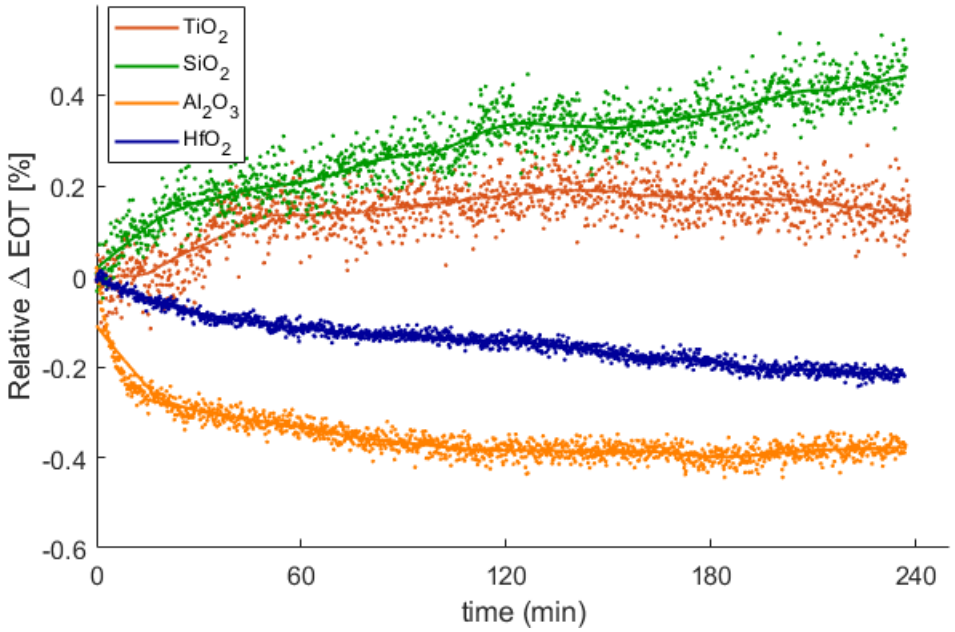

Figure 3.35: Relative EOT optical response of passivated membranes as a function of time while exposed to a continuous PBS flow.

3.3.3 Noise level analysis and limit of detection

Five stability tests were performed per type of membranes and the normalized noise distributions was plotted for each one of them. The distributions were fit using a Gaussian function and the noise level was extracted. Finally, the noise level for the five measurements was averaged to obtain σ_N and calculate the theoretical limit of detection $3\sigma_N$, as schematically shown in figure 3.36. The obtained results are shown in table 3.12.

The highest noise noise level is obtained for $PSiO_2/TiO_2$, followed by $PSiO_2$, 0.089 and 0.080, respectively. The $PSiO_2/Al_2O_3$ and $PSiO_2/HfO_2$ membranes present a noise level of 0.030 and 0.019, respectively. The reduction in the noise level obtained with these two atomic layer depositions leads to an improved limit of detection when compared to $PSiO_2$. The improvement of the LoD results in a greater reliability regarding

Table 3.12: Noise level and theoretical limit of detection for the passivated PSi membranes

	σ_N [%]	LoD [%]
$PSiO_2$	0.080	0.241
$PSiO_2/HfO_2$	0.019	0.056
$PSiO_2/Al_2O_3$	0.030	0.090
$PSiO_2/TiO_2$	0.089	0.267

the accuracy of the measured shifts. Indeed, both the stability evaluation and bacteria detection through the EOT shift over time become more significant when the LoD value is reduced [3]. The reduction in noise is again linked to the higher reflectivity of the ALD layers that leads to higher intensity Fabry-Pérot fringes and results in an better fit.

3.4 Conclusion

In this chapter, successful deposition of metal oxide ALD layers on porous silicon membranes was demonstrated. The homogeneity of the coating was verified through the depth of the porous matrix, together with the surface chemical composition, morphology, optical and mechanical properties of the porous matrix. The ALD leads to a decrease in porosity and pore size that, on one hand, results in improved mechanical properties, but, on the other hand, leads to an increased resistance to flow, which can be detrimental for biosensing purposes.

For a more precise assessment of porosity, pore size distribution, and morphology nitrogen adsorption methods could be used, such as BET (Brunnauer–Emmett–Teller). These methods are especially sensitive to small pore structures, in particular micropores, but they are relatively insensitive to macropores. Therefore, a more complete picture of the pore morphology can be extracted by combining both electron microscopy and the BET method [40]. Furthermore, the fabrication parameter can be tuned to compensate for the porosity decrease upon ALD. Most likely, the resistance to flow increase comes from the partial clogging of the low porosity contrast layer. Therefore, this layer could be etched at a higher current density to increase its porosity prior to ALD.

The ALD oxide-coated PSiMs were compared to low temperature oxidized membranes and presented improved stability. Particularly, Al_2O_3 and TiO_2 membranes are highly stable after the first 10 minutes, and 50 minutes of incubation in PBS, respectively. Al_2O_3 and HfO_2 coated PSiMs showed a reduced noise level which resulted in a reduction of the limit of detection by a factor of 3 and 4, respectively. Effects of pressure and deflection remain not fully understood. In order to do so, a more complete microfluidics study should be performed.

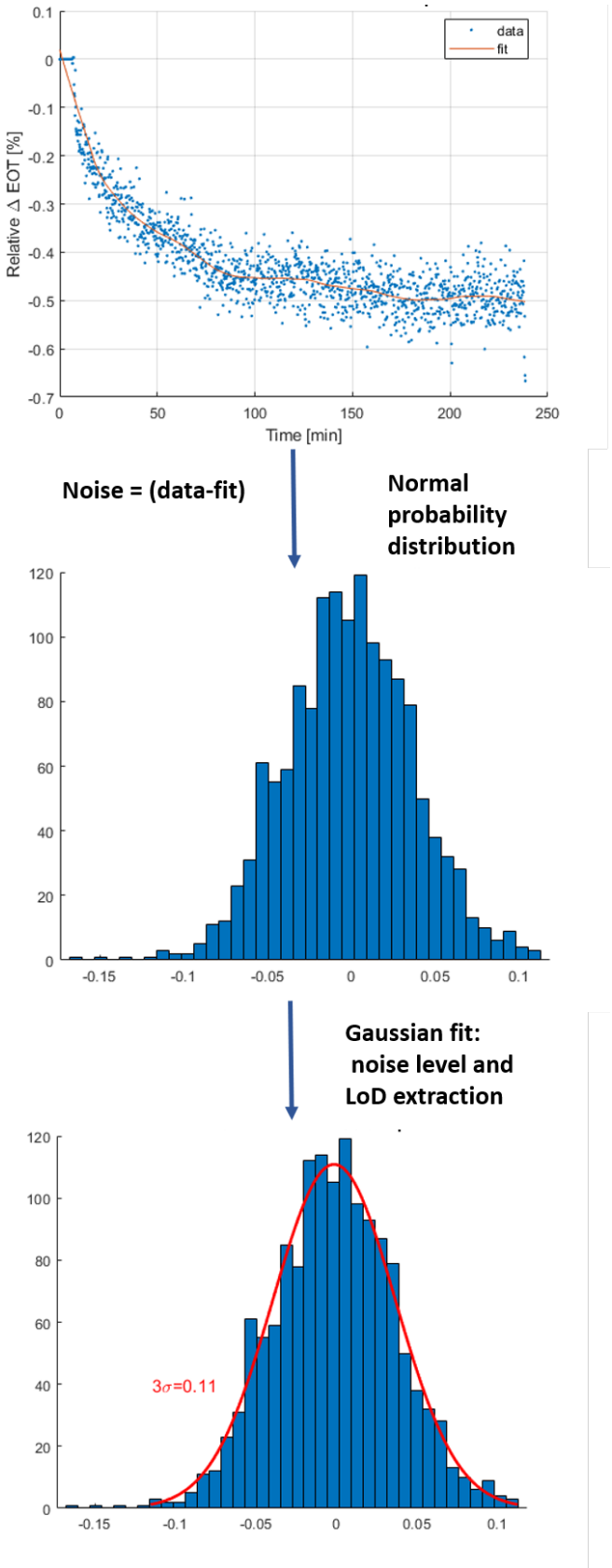

Figure 3.36: Schematic representation of the noise level analysis procedure: (1) the data is fit using a moving average (low pass filter with coefficient equal to the reciprocal of the span, span=0.15), (2) the noise is calculated by taking the difference between the data and the fit, (3) a normal probability distribution is plotted from the calculated noise, (4) a Gaussian fit is applied to the distribution, allowing to extract the noise level σ_N and the theoretical limit of detection LoD=$3\sigma_N$.

Chapter 4

Selective bacteria detection using lytic enzimes

Contents

Overview

This chapter reviews some detection schemes for PSi-based bacteria biosensing. A distinction is made between direct and indirect bacteria detection and some important concepts are elucidated. Al_2O_3 passivated porous silicon membranes are used to demonstrate the selective bacteria detection through their lysate for B. *cereus*. The results are discussed in terms of limit of detection and response time.

4.1 Porous silicon for bacteria detection

Porous silicon biosensors for bacteria detection can be classified in two main categories: indirect and direct bacterial detection, as schematically shown in figure 4.1. In indirect detection, the sensing is achieved by monitoring only fractions of the secreted bacteria cells or protein/DNA fragments. In the direct case, detection is achieved by directly binding the entire bacterium cell to the PSi surface via appropriate capture probes [12]. Some optical schemes for bacteria detection are described in the following sections. The examples given focus mainly on the developments from 2014 to the present date, scientific advancements before 2014 are reviewed elsewhere [12]. Table 4.1 summarizes the detection of different bacteria, both directly and indirectly, using PSi devices.

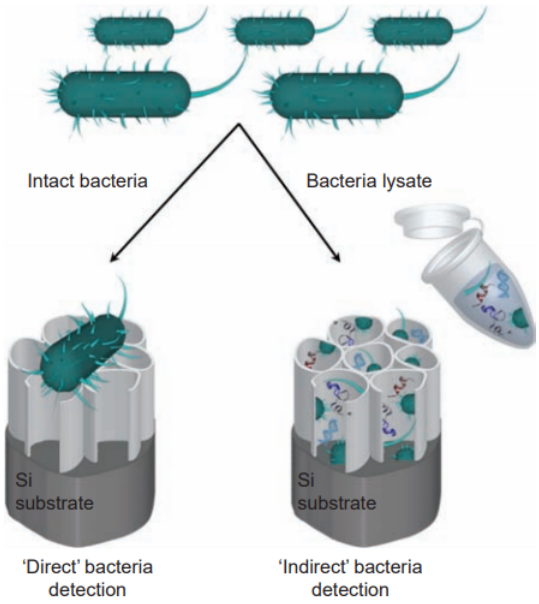

Figure 4.1: Schematic outline of the concepts of indirect and direct bacteria detection by PSi-based biosensors. In the direct detection the whole bacterial cell is capture and detected on the surface of the PSi layer, while in the indirect detection, the sample containing the target bacteria is lysed before the detection, the lysate is thus detected upon penetration in the PSi layer (the bacteria are not always lysed, sometimes their secretions are the target analyte). Extracted from [12].

4.1.1 Indirect bacteria detection

The indirect detection scheme is based monitoring only a fraction of the bacteria cell or their secreted cells fragments (such as specific proteins or DNA sequences). Pre-treatment of the target bacteria, such as enzymatic treatment, heating or sonication, is required, demanding laboratory set-up and longer total assay [12].

For example, S-layer protein (SLP) is a surface protein present in many bacteria, and a PSi-based microfluidic biosensor has been developed for its detection. A porous silicon layer was prepared from a p-type silicon wafer by electrochemical etching and thermally oxidized at 500 °C. To further enhance the stability, the matrix was coated by using a sol-gel

solution of TiO_2. The as-obtained sensor was then integrated in a microfluidc system, in which, first protein A, and then, anti-SLP was pumped into the cell. Protein A, acted as a spacer to reduce the steric hindrance and improve the antigen–antibody interaction. The biosensor exhibited one of the lowest detection limits reported for PSi-based reflecometric biosensors for protein detection, being able to detect 3.2 μg/mL (0.7 pM). The high sensitivity was attributed to the high enriching capability, high refractive index of the TiO_2-coated PSi biosensor and the dynamic sampling system [103].

Other detection systems rely on electrochemical transduction for bacteria sensing. A freestanding PSiM biosensor deposited on a gold slide was proposed for the detection of lipopolysaccharides (LPS), also known as endotoxins, present in the outer cells of Gram-negative bacteria and some cyanobacterias, that are constantly released during active cell growth and upon cell death. The membrane was functionalized with polymyxin B (PmB) due to its strong affinity to LPS. The sensing strategy exploited the nanochannel blockage that occurs upon binding of the analyte with the substrate. The blockage hindered the diffusion of electroactive species present in the solution to the gold slide, which resulted in a decrease in the current intensity, measured in differential pulse voltammetry (DPV), as schematically shown in figure 4.2. The platform showed excelent analytical performance, being able to detect LPS released from bacteria (*P. aeruginosa* and *E. coli*) at the level of 1 CFU/mL [104].

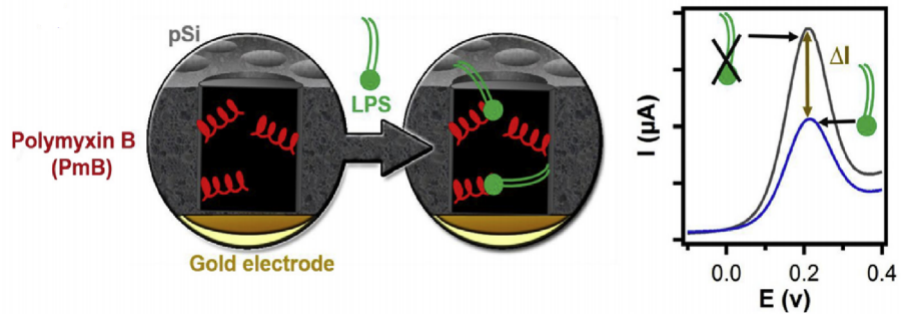

Figure 4.2: Sensing principle of a voltametric PSiM-on-gold biosensor, and corresponding differential pulse voltammetry (DPV) traces before and after the binding of lipopolysccharides (LPS) bacterial toxins. Extracted from [104].

An aptamer-conjugated PSi biosensors has been proposed for the detection of lipase from *Geobacillus stearothermophilus*. Aptamers are oligonucleotides (single-stranded DNA or RNA) that can bind their targets with high affinity and specificity. The biosensor was exposed to the target proteins as well as to complex fluids (i.e., bacteria lysates containing target proteins) and real-time identification of aptamer-protein binding events was achieved through monitoring of the optical interference spectrum, as schematically shown in figure 4.3. Detection experiments were successfully conducted down to 10μM lipase concentration [105].

4.1.2 Direct bacteria detection

Direct detection takes place when the target analyte is the entire bacterial cell, which is directly captured on the PSi surface, but is not able to penetrate into the pores due to its

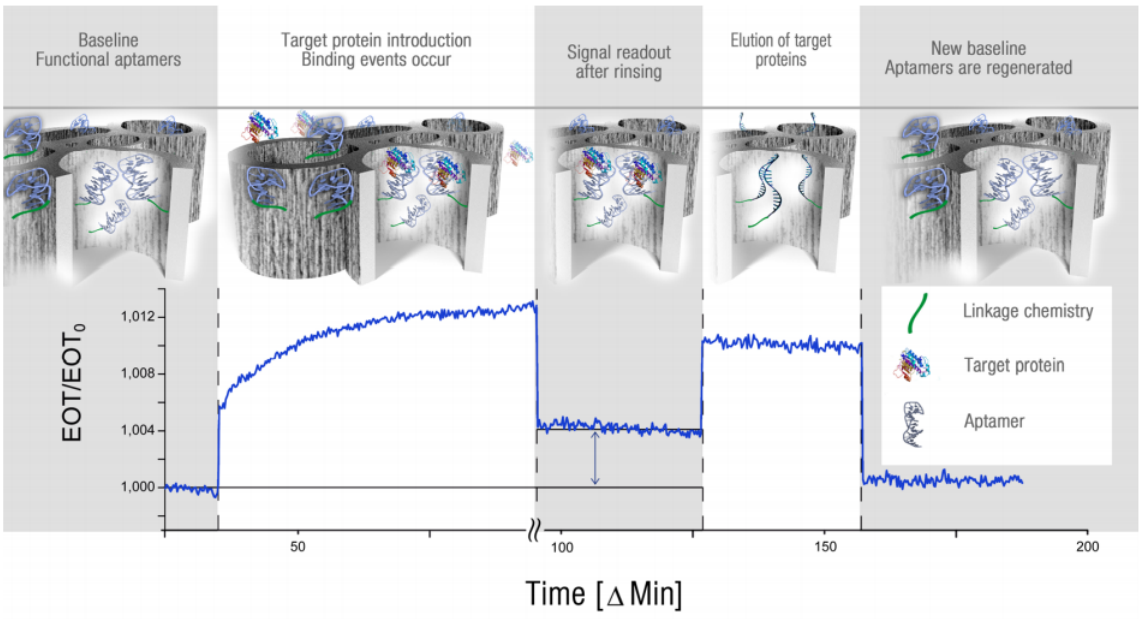

Figure 4.3: Relative EOT value vs. time of 6H7-functionalized $PSiO_2$ during a typical biosensing experiment. Extracted from [105]

dimensions. This can be achieved through the use of specific recognition probe, as already stated or via nonspecific interactions [12].

A PSi-based biosensor functionalized with lectins (ConA, WGA) was proposed for the direct detection of *Escherichia coli* (*E. coli*) and *Staphylococcus aureus*(*S. aureus*) through RIFTS. The advantage of using lectins is that they have specifc carbohydrate-binding properties and are inexpensive compared to popular antibodies. Oxidized porous silicon samples were dipped into ethanolic APTES solution, incubated in glutaraldehyde and finally dipped in lectin solution. The intensity of the peaks obtained in the fast Fourier transform (FFT) spectra was monitored and a limit of detection of 10^3 CFU/mL obtained.

A nonspecific direct detection scheme was proposed for surface enhanced Raman scattering (SERS), as briefly discussed in section 2.2.1. Plasmonics silver and palladium bimetallic alloy nanoparticles ((Ag@Pd)NPs) within gradient porosity silicon (GPSi) layer were prepared and investigated. The SERS active substrates were prepared by dynamic etching the gradient porous silicon matrix and adding the nanoparticles by simple immersion plating. The SERS enhancement factor exhibited were 2.1×10^3, 8.6×10^4, 2.3×10^5, and 5.4×10^4 with 60, 120, 180, and 240 s immersion time, respectively for detecting an ultra-low concentration of about 1 CFU/mL [106].

Table 4.1: Recent advances in porous silicon biosensors for bacteria detection

Detection type	PSi structure	Transduction mechanism	Capture probe	Target	LoD	Ref.
Indirect	$PSiO_2$ double-layer membrane	Optical (reflectivity)	-	Lysate: *B. cereus*, *S. epi*	10^5 CFU/mL	[5]
	TiO_2/$PSiO_2$ single layer	Optical (reflectivity)	Anti-SLP	S-layer protein (SLP): *L. acidophilus*	0.70 ± 0.37 pM	[103]
	Hydrosilylated PSi membrane	Electrochemical (amperometric)	Polymyxin B (PmB)	Lipopolysaccharides (LPS): *E. coli*/*P. aeruginosa*	1 CFU/mL	[104]
	PSi-THC single-layer	Electrochemical (amperometric)	Hyal methacrylate (HYAMA)	Hyal enzime: *S. aureus*	1 microg/mL	[107]
	$PSiO_2$ - Double Bragg mirror	Optical (reflectivity)	DNA	DNA: AOB	27.1 nM	[108]
	$PSiO_2$ single layer	Optical (reflectivity)	His-tag binding aptamer (6H7)	T6 lipase: *G. stearothermophilus*	10 micoM	[105]
	$PSiO_2$ single layer	Optical (reflectivity)	antimicrobial sequence (K7α12)	Lysate: *E.coli*	10^3 cells/mL	[109]
Direct	(Ag@Pd)NPs/GPSi	Optical (SERS)	-	*E. coli*	1 CFU/mL	[106]
	$PSiO_2$ single layer	Optical (reflectivity)	Lectin (ConA and WGA)	*E. coli*/*S. aureus*/ *K. aerogenes*/*B. subtilis*	10^3 cells/mL	[110]
	$PSiO_2$ single layer	Optical (reflectivity)	Aptamer	*L. acidophilus*	10^6 cells/mL	[111]
	$PSiO_2$ single layer	Optical (reflectivity)	*E. coli* antibody(IgG)	*E. coli*	10^3 cells/mL	[112]
	$PSiO_2$ single layer	Optical (reflectivity)	*E. coli* antibody	*E. coli*	10^3 - 10^7 CFU/mL	[113]

4.2 Bacteria detection through their lysate: Materials and methods

4.2.1 Bacteria strain growth

For bacteria detection, *B. cerus ATCC 10987* was used as reference strain. The bacteria were grown overnight (O/N) in Lysogeny Broth (LB) or LB-agar plates at 30 °C. Concisely, 20 mL of LB were inoculated with 200 μL of culture and incubated for 3 h at 30 °C. The cultures were then centrifuged at 10,000× g for 5 min at room temperature and the supernatants were resuspended in 20 mL of PBS. This washing step was repeated once over and the optical density (OD_{600}) was adjusted to $OD_{600} = 0.2$ (10^6 CFU/mL). Additionaly, the *B. cerus* suspension was diluted ten times for a 10^5 CFU/mL detection experiment.

4.2.2 Real-Time Detection of *B. cereus* lysate on $PSiO_2/Al_2O_3$ membranes

The $PSiO_2/Al_2O_3$ membranes were used for bacteria detection. Due to time constraints, only one type of membrane could be tested and the choice of the Al_2O_3 passivated one was mainly based on the reduced noise level, and thus low theoretical limit of detection exhibited in stability testing, when compared to the other alternatives. The detection protocol is illustrated in figure 4.4.

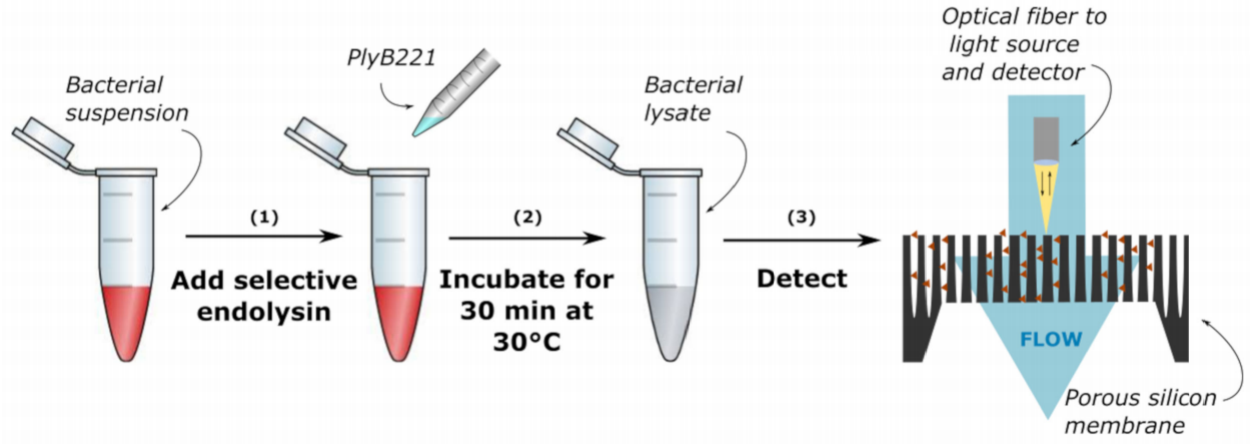

Figure 4.4: Protocol of bacteria detection through their lysate: (1) lysis of the bacteria using a selective endolysin, (2) incubation for 30 min and (3) optical detection on a porous silicon membrane. Extracted from [5].

First, 250 μL of non-purified PlyB221 endolysin (with glycerol added to preserve it) were added to 4.75 mL of exponential phase *B. cereus* re-suspended in PBS, so as to reach a final protein concentration of 50 μg/mL. The detailed procedure for extraction and purification

of PlyB221 endolysin can be found elsewhere [6], here the protein concentration was adjusted to 1 mg/mL. The total volume obtained, 5 mL, was sufficient for at least 4 detections.

The suspension was then incubated for 30 min at 30 °C. Before flowing the bacterial lysate, PBS solution was injected for 10 min and reference measurements were performed. The choice of flowing PBS for 10 min is based on the transition region observed for the $PSiO_2/Al_2O_3$ passivated membrane which exhibted stable behaviour only after this time mark. *B. cereus* lysate suspensions were injected at the same flow speed as the PBS solution. Optical measurements were carried out every 10 s for 60 min. The relative EOT was then extracted from these measurements. A control test, with only the PlyB221 endolysin at the same concentration was also performed, following the same protocol described previously. For all tests, measurements were performed at least 3 times.

4.2.3 Experimental Setup and optical reflectivity measurements

As for the stability tests, the $PSiO_2/Al_2O_3$ membrane is placed inside a polycarbonate fluidic cell (figure 3.19). A fiber coupled Ocean Optics JAZ spectrometer and a 10-mW halogen light source were used to record reflectivity spectra. The reflectivity spectra are acquired overtime (one spectrum every 10 s, with an integration time of 1 s), and the Fabry-Pérot fringes are then processed using a Fourier transform to obtain the EOT. The evolution over time of the effective optical thickness, *EOT(t)*, is then computed as a percentage change relative to EOT_0, as defined in equation 4.1.

$$\Delta EOT = \frac{EOT(t) - EOT_0}{EOT_0} \times 100[\%] \tag{4.1}$$

4.3 Results and discussions

The performance of the $PSiO_2/Al_2O_3$ membrane is illustrated in figure 4.5. Three different tests were performed: in a PlyB221 endolysin suspension, and in a *B. cereus* lysate for two concentrations, 10^6 CFU/mL and 10^5 CFU/mL. The theoretical limit of detection (LoD) was calculated as described in section 3.3.3 from the stability test in PBS. For $PSiO_2/Al_2O_3$ membranes, the calculated LoD is 0.09 %. Due to the resistance to flow, only a flow speed of 0.3-0.5 μm/min at 3 bar pressure was attained.

The control test with only the PlyB221 endolysin showed a decrease in relative EOT of -0.36% in one hour. Upon the penetration of bacterial lysate, at 10^6 CFU/mL concentration, inside the membrane, a significant increase of relative EOT was measured, exceeding the LoD after 9 min and reaching an average +0.25% after 1 h. For the bacteria lysate at 10^5 CFU/mL concentration, a lower increase of relative EOT is observed, exceeding the LoD after 39 min and reaching an average +0.13% after 1 h.

The observed shift upon penentration of bacteria lysate at 10^6 CFU/mL concentration is much lower than the one observed by Vercauteren *et al.* [5] of +2.43% after 1 h. This can be attributed to different factors. First, the porosity decrease in ALD induces a loss in sensitivity that translates into a lower shift in the relative EOT, when compared

to a higher porosity membrane. Second, the same loss in porosity and probable pore clogging (specially in the contrast layer) have an impact in flow which is detrimental for the molecular transport efficiency of the membranes. Indeed, as discussed in section 2.3.6, the mass transport of the analyte is influenced by both diffusion and convection, the latter being enhanced for higher flow velocities. The flow speed applied could not exceed 0.5 μm/min which is 30 to 40 times lower to the one obtained by Vercauteren *et al.* [5] (15-20 μm/min). Third, the endolysin seems to accelerate dissolution/degradation of the porous matrix (decrease in relative EOT of -0.36% in one hour). The reasons behind this accelerated degradation are still not fully understood, but it might be linked to the presence of glycerol in the endolysin solution to aid its conservation. In any case, further investigation is required to comprehend the reasons between this decrease in relative EOT and ways to prevent it.

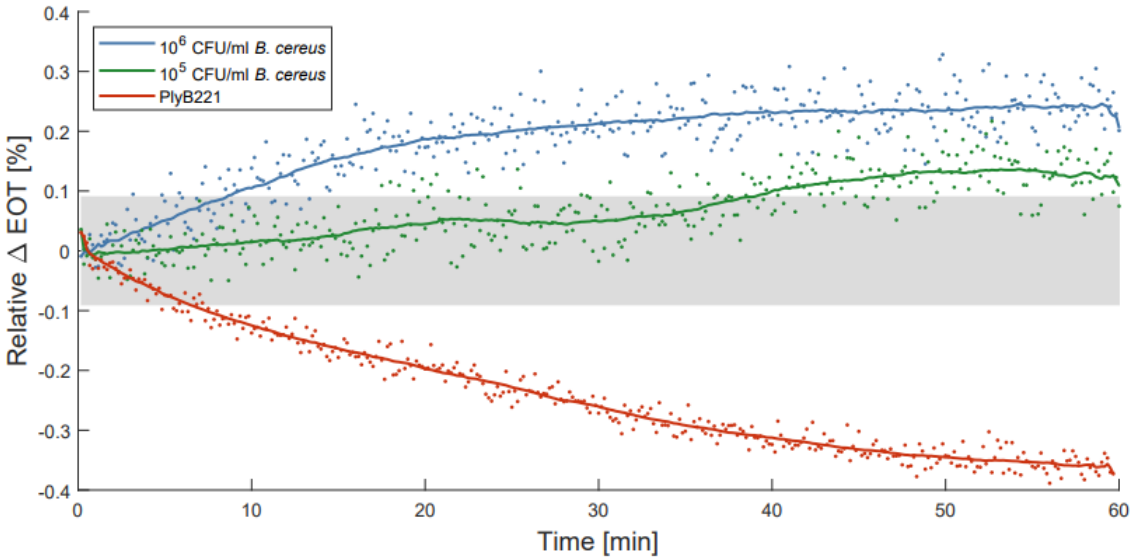

Figure 4.5: Relative effective optical thickness (EOT) shift measured on a PSi membrane for 1 h in in PlyB221 endolysin suspension (red), and in a *B. cerus* lysate at 10^6 CFU/mL (blue) and at 10^5 CFU/mL (green) concentrations.

Nevertheless, the reduced limit of detection obtained with Al_2O_3 ALD, allowed exceeding the LoD in 9 min, similarly to the performance obtained by Vercauteren *et al.* [5], even if the flow speed is much lower in the present case. This result shows that, although there is definitely room for improvement, real-time optical bacteria detection using the $PSiO2/Al_2O_3$ membrane is possible.

For the determination of the limit of detection in terms of bacteria concentration, a decreased concentration of *B. cereus* was used. Results are displayed in figure 4.6. The shift observed in PBS solution is also plotted and it is taken from the stability test after 15 min of flow, when the Al_20_3 passivated membrane becomes more stable. As previously discussed, an average relative EOT shift of +0.13% after 1 h is observed for a 10^5 CFU/mL concentration. This value is just above the theoretical LoD of 0.09% and can be interpreted as the LoD in terms of bacteria concentration. The detection of 10^5 is, however, not a

100% reproducible. The three detection led respectively to +0.165%, +0.118%, +0.089% shifts, thus the last detection was just below the theoretical LoD. More tests should be made to quantify the reproducibility of the detection.

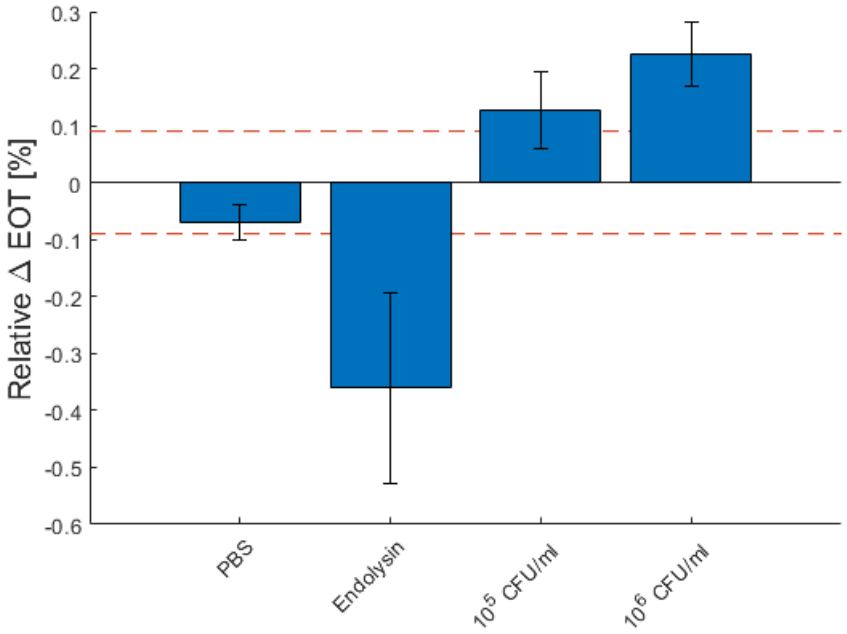

Figure 4.6: Characteristic relative effective optical thickness (EOT) shift measured on a PSi membrane after 1 h in PBS, in a PlyB221 endolysin suspension and in different concentrations of *B. cereus* lysate. The dashed red line represents the noise level, fixed as 3σ of the signal measured in PBS. The detection limit is 10^5 CFU/mL of *B. cereus*.

These results can be discussed in terms of: response time, and limit of detection. The response time obtained in this work is comparable to other functionalized PSiMs [60, 114, 115]. The total detection time (which includes both lysis and optical monitoring) is less than 2 h. In terms of bacterial concentration, a limit of detection of 10^5 CFU/mL remains high compared to other PSi bacteria sensors [109, 110, 112, 113], yet tuning the ALD parameters to adjust porosity and ensure a better flow, together with a deeper investigation of the reasons behind increased degradation by the endolysin solution could significantly help to improve this value.

4.4 Conclusion

In this chapter, the proof-of-concept of an $PSiO_2/Al_2O3$ membrane biosensor for the detection of bacteria through their lysate is demonstrated. Promising results in terms of sensitivity and time of response, with a detection of 10^5 CFU/ml of *B. cereus* lysate in less than one hour.

While most of the biosensors investigated in the literature rely on functionalization to capture the analyte [109, 110, 112, 113], the biosensor studied in this work bases

the capture on a size exclusion effect. This detection scheme offers several advantages: reduced production time and no requirements on the storage and detection conditions, due to the lack of functionalization. Furthermore, the presented biosensor is compatible with all standard fabrication techniques used in microelectronic cleanrooms which could facilitates its mass production and packaging, for a very low cost. Additionally, since no functionalization agent is used, sensors from the same batch could be applied for the detection of different strains of bacteria, as long as a selective endolysin is available [5].

The reduced porosity resulting from atomic layer deposition indeed had a detrimental effect both to the maximum flow speed attainable and to the EOT shift upon bacteria penetration. The fabrication parameters need to be revisited in order to adjust the porosity and increase the sensitivity.

Chapter 5

Conclusions and perspectives

Master thesis conclusions

In this master thesis, two main subjects have been investigated towards the development of a porous silicon membrane-based biosensor or the selective detection of bacteria lysate:

- The passivation of porous silicon membranes for their use in aqueous media for biosensing in a microfluidic set-up. The passivation method proposed was atomic layer deposition of different metal oxides (Chapter 3);
- The passivated biosensor performance for the detection of *B. cerus* lysate (Chapter 4) as well as its response to the endolysin suspension.

The study of porous silicon membranes passivation through ALD contributed to important scientific findings. First, the conformal deposition of the species on the porous silicon matrix was demonstrated. Second, the use of porous silicon membranes rather than substrates allows a homogeneous distribution of the passivation layer from top to bottom. Third, low temperature depositions were achieved without inducing cracking or collapsing of the membranes. However, the ALD passivation resulted in a significant decrease in porosity due to the clogging of small pores which has a positive effect in terms of mechanical properties, as confirmed with nanoindentation, but a negative one in terms of increased resistance to flow, as confirmed by current measurements in ionic solution. Nevertheless, even if the flow speed and sensitivity are compromised, the average pore diameter is still large enough for the penetration of the target analytes. Furthermore, ALD passivation is linked the stability of the porous samples in aqueous media. The passivated samples exhibited a similar or improved stability compared to thermally oxidized samples, while resulting in a significant reduction of noise for HfO_2 and Al_2O_3 coatings. A reduction of the limit of detection by a factor of 4 and 3 for $PSiO_2/HfO_2$ and $PSiO_2/Al_2O_3$ passivations, respectively, was obtained.

The detection of *B. cerus* lysate using a $PSiO_2/Al_2O_3$ passivated membrane was possible at a 10^5 CFU/mL concentration in less than one hour. The reduced porosity caused by the ALD passivation had an impact in flow and sensitivity. Nevertheless, detection of 10^6 CFU/mL of the bacteria lysate in less than 9 min was achieved due to the decrease in the noise level obtained after ALD. Additionally, an enhanced degradation of the passivated

porous matrix was observed in endolysin suspension and the reasons behind this finding still require further investigation.

In conclusion, this master thesis was successful towards the goal of improving porous silicon membranes stability in aqueous media. Further adjustment of fabrication parameters to compensate the reduced porosity are needed in order to translate the stability improvements into a lower limit of detection for the biosensor in terms of bacteria concentration. The results corroborate the possibility of using porous silicon membranes for bacteria detection through their lysate while the limit of detection still needs to be driven down to achieve a truly competitive biosensor ($<10^3$ CFU/mL).

Perspectives

Even though the proof of concept for bacteria detection on an $PSiO_2/Al_2O_3$ membrane was successfully demonstrated, there are many aspects that can still be improved. In each chapters conclusions, some suggestions to improve results and performance have already been briefly discussed. This section focuses on suggestions regarding both stability and signal enhancement to push the bacteria biosensor towards higher sensitivity.

Stability

Atomic layer deposition was the chosen technique both for the highly conformal coating that it offers and for the possibility to control the thickness with an Ångstrom precision. This study proved that an ALD thickness of 3-5 nm, three times thinner than the ones proposed by Rasson *et al.*, can significantly improve the membranes stability when compared to simple oxidation. However, in an effort to maintain a highly porous matrix for microfluidic applications, even thinner layer could be studied and characterized in terms of their stability.

Annealing of the ALD passivated membranes could also be used as an strategy to enhance stability. For example, the Al_2O_3 surface passivation was found to depend strongly on the annealing temperature and the annealing atmosphere. The measured lifetime values increased with higher annealing temperatures (~400 °C) in muffle furnace [116, 117] . Most likely, annealing at such a high temperature is not possible for the porous silicon membranes for mechanical stability reasons that prevent high temperature post-processing. However, annealing at lower temperatures (~300 °C) could be tested. Furthermore the ALD temperature could also be increased to obtain denser and better quality films, up to 150-200 °C, but the effect on mechanical stability needs to be taken into consideration.

As previously discussed, the porosity of the contrast layer (estimated at 50%) could be increased before the atomic layer deposition. The contrast layer is more likely the major source of clogging due to its lower porosity and smaller pores (15 nm). That suggestion is, however, not valid for the sensing and support layers which are already highly porous (~75% and 70% respectively). Increasing too much the porosity and pore size leads to thinner pore walls which can become very fragile, making the whole structure mechanically

unstable.

Another passivation technique that might not compromise porosity as much as ALD is hydrocarbonization. This strategy could replace the oxidation step and even act as a stop layer for the deep reactive ion etching, eliminating one process step. Furthermore, this has been reported as the go to technique when thermal oxidation is not enough to ensure stability [40] and has been adopted in other biosensing studies [107, 118]. As discussed in section 3.1.3, the surface could be further modified by grafting carboxylic acid species to increase the hydrophilicity and, as a consequence, the wettability [68], hence decrease the pressure needed to obtain the desired flow.

Finally, the Al_2O_3 passivated membranes showed increased degradation in the endolysin suspension. This is an unexpected behaviour that was not previously observed for SiO_2 passivated membranes by Vercauteren *et al.* [5]. This may be due to the fact that in this other study the endolysins were purified before use, in the case of this master thesis, they were previously conserved in glycerol and not purified. Since the effect of glycerol in stability was not assessed, the easiest way to confirm this hypothesis is to eliminate this component from the endolysin suspension through purification. If the membranes show improved stability in the absence of glycerol, the limit of detection could be significantly improved.

Signal enhancement

The improved reflectivity of the porous silicon membranes upon ALD contributed for a significant increase in the signal. However, the proposed deposition method may eventually not be viable for a flow-through biosensing scheme at low limits of detection due to the observed porosity decrease. One further perspective for porous silicon biosensors is a detection scheme based on surface enhanced Raman scattering (SERS). As briefly discussed in section 2.2.1, this technique uses specific molecules that are adsorbed on the surface (in the proposed case, porous silicon matrix) to enhance Raman scattering. This can be achieved by using nanostructured noble metal surfaces supporting localized surface plasmons [63]. A PSi biosensor using adsorbed plasmonics silver and palladium bimetallic alloy nanoparticles for direct bacteria detection was able to bring the limit of detection down to 1 CFU/mL [106].

SERS detection could be the next step to achieve a biosensor with three competitive features: sensitivity, selectivity and low response time. As discussed in this work, the sensor already exhibits selectivity combined with versatility by adding the endolysin suitable for the bacteria strain of interest. Furthermore, low response time is obtained by the flow-through set up that brings the analyte to the surface faster than on a flow-over scheme due to the contribution of convection. The final aspect to be improved is the limit of detection and that could be decreased to really competitive levels by further investigations towards SERS.

Bibliography

[1] Jim O'Neill. Tackling drug-resistant infections globally: final report and recommendations - the review on antimicrobial resistance, 2016.

[2] Umer Farooq, Qiaoli Yang, Muhammad Wajid Ullah, and Shenqi Wang. Bacterial biosensing: Recent advances in phage-based bioassays and biosensors. *Biosensors and Bioelectronics*, 118:204–216, October 2018.

[3] Jonathan Rasson. Stable porous silicon-based optical sensing platform towards detection of bacterial lysis. 2018. PhD thesis, Univeristé Catholique de Louvain. Prom. : Francis, Laurent.

[4] Rosalba Moretta, Luca De Stefano, Monica Terracciano, and Ilaria Rea. Porous silicon optical devices: Recent advances in biosensing applications. *Sensors*, 21(4):1336, February 2021.

[5] Roselien Vercauteren, Audrey Leprince, Jacques Mahillon, and Laurent A. Francis. Porous silicon biosensor for the detection of bacteria through their lysate. *Biosensors*, 11(2):27, January 2021.

[6] Audrey Leprince, Manon Nuytten, Annika Gillis, and Jacques Mahillon. Characterization of PlyB221 and PlyP32, two novel endolysins encoded by phages preying on the bacillus cereus group. *Viruses*, 12(9):1052, September 2020.

[7] WHO World Health Organization. Antimicrobial resistance, 2020. Available at https://www.cdc.gov/drugresistance/pdf/threats-report/2019-ar-threats-report-508.pdf. Accessed on 20/04/2021.

[8] CDC. Antibiotic resistance threats in the united states, 2019. Department of Health and Human Services, CDC.Atlanta, GA: U.S.

[9] Linda Váradi, Jia Lin Luo, David E. Hibbs, John D. Perry, Rosaleen J. Anderson, Sylvain Orenga, and Paul W. Groundwater. Methods for the detection and identification of pathogenic bacteria: past, present, and future. *Chem. Soc. Rev.*, 46:4818–4832, 2017.

[10] Olivier Lazcka, F. Javier Del Campo, and F. Xavier Muñoz. Pathogen detection: A perspective of traditional methods and biosensors. *Biosensors and Bioelectronics*, 22(7):1205 – 1217, 2007.

[11] Christopher D. Doern and Susan M. Butler-Wu. Emerging and future applications of matrix-assisted laser desorption ionization time-of-flight (maldi-tof) mass spectrometry in the clinical microbiology laboratory: A report of the association for molecular pathology. *The Journal of Molecular Diagnostics*, 18(6):789 – 802, 2016.

[12] N. Massad-Ivanir and E. Segal. 12 - porous silicon for bacteria detection. In Hélder A. Santos, editor, *Porous Silicon for Biomedical Applications*, pages 286–303. Woodhead Publishing, 2014.

[13] Neelja Singhal, Manish Kumar, Pawan K. Kanaujia, and Jugsharan S. Virdi. Maldi-tof mass spectrometry: an emerging technology for microbial identification and diagnosis. *Frontiers in Microbiology*, 6:791, 2015.

[14] Jackson O. Lay Jr. Maldi-tof mass spectrometry of bacteria*. *Mass Spectrometry Reviews*, 20(4):172–194, 2001.

[15] Thermo Fischer Scientific. Invitrogen School of molecular biology: PCR Basics.[Online; accessed 22-January-2021].

[16] J.M. Willey, L. Sherwood, L.M. Prescott, and C.J. Woolverton. *Prescott, Harley, and Klein's Microbiology*. McGraw-Hill Higher Education. McGraw-Hill Higher Education, 2008. (Chapter 35 - Clinical Microbiology and Immunology).

[17] MBL life science.

[18] Dmitri Ivnitski, Ihab Abdel-Hamid, Plamen Atanasov, and Ebtisam Wilkins. Biosensors for detection of pathogenic bacteria. *Biosensors and Bioelectronics*, 14(7):599–624, 1999.

[19] Parinaz Babaie, Arezoo Saadati, and Mohammad Hasanzadeh. Recent progress and challenges on the bioassay of pathogenic bacteria. *Journal of Biomedical Materials Research Part B: Applied Biomaterials*, 109(4):548–571, 2021.

[20] Leland C. Clark Jr. and Champ Lyons. Electrode systems for continuous monitoring in cardiovascular surgery. *Annals of the New York Academy of Sciences*, 102(1):29–45, 1962.

[21] Anbuthiruselvan Solaimuthu, Ane Nishitha Vijayan, Padmaja Murali, and Purna Sai Korrapati. Nano-biosensors and their relevance in tissue engineering. *Current Opinion in Biomedical Engineering*, 13:84–93, 2020.

[22] Luis Castillo-Henríquez, Mariana Brenes-Acuña, Arianna Castro-Rojas, Rolando Cordero-Salmerón, Mary Lopretti-Correa, and José Roberto Vega-Baudrit. Biosensors for the detection of bacterial and viral clinical pathogens. *Sensors*, 20(23), 2020.

[23] Pawan Jolly Nello Formisano Pedro Estrela, Nikhil Bhalla. Introduction to biosensors. 60:1–8, 2016.

[24] Niina J. Ronkainen, H. Brian Halsall, and William R. Heineman. Electrochemical biosensors. *Chem. Soc. Rev.*, 39:1747–1763, 2010.

[25] Momna Rubab, Hafiz Muhammad Shahbaz, Amin N. Olaimat, and Deog-Hwan Oh. Biosensors for rapid and sensitive detection of staphylococcus aureus in food. *Biosensors and Bioelectronics*, 105:49–57, 2018.

[26] Vijayalakshmi Velusamy, Khalil Arshak, Olga Korostynska, Kamila Oliwa, and Catherine Adley. An overview of foodborne pathogen detection: In the perspective of biosensors. *Biotechnology Advances*, 28(2):232–254, 2010.

[27] Yung-Tsan Chen, Ya-Chu Lee, Yao-Hsuan Lai, Jin-Chun Lim, Nien-Tsu Huang, Chih-Ting Lin, and Jian-Jang Huang. Review of integrated optical biosensors for point-of-care applications. *Biosensors*, 10(12), 2020.

[28] Alessandra Camarca, Antonio Varriale, Alessandro Capo, Angela Pennacchio, Alessia Calabrese, Cristina Giannattasio, Carlos Murillo Almuzara, Sabato D'Auria, and Maria Staiano. Emergent biosensing technologies based on fluorescence spectroscopy and surface plasmon resonance. *Sensors*, 21(3), 2021.

[29] Kyle C. Bantz, Audrey F. Meyer, Nathan J. Wittenberg, Hyungsoon Im, Özge Kurtuluş, Si Hoon Lee, Nathan C. Lindquist, Sang-Hyun Oh, and Christy L. Haynes. Recent progress in sers biosensing. *Phys. Chem. Chem. Phys.*, 13:11551–11567, 2011.

[30] Christoph Fenzl, Thomas Hirsch, and Otto S. Wolfbeis. Photonic crystals for chemical sensing and biosensing. *Angewandte Chemie International Edition*, 53(13):3318–3335, 2014.

[31] Giorgio Quaranta, Guillaume Basset, Olivier J. F. Martin, and Benjamin Gallinet. Recent advances in resonant waveguide gratings. *Laser & Photonics Reviews*, 12(9):1800017, 2018.

[32] Pankaj K. Sahoo, Swagato Sarkar, and Joby Joseph. High sensitivity guided-mode-resonance optical sensor employing phase detection. *Scientific Reports*, 7(1), 2017.

[33] Jules L. Hammond, Nello Formisano, Pedro Estrela, Sandro Carrara, and Jan Tkac. Electrochemical biosensors and nanobiosensors. *Essays in Biochemistry*, 60(1):69–80, 2016.

[34] Tomas Bertok, Alena Sediva, Jaroslav Katrlik, Pavol Gemeiner, Milan Mikula, Martin Nosko, and Jan Tkac. Label-free detection of glycoproteins by the lectin biosensor down to attomolar level using gold nanoparticles. *Talanta*, 108:11–18, April 2013.

[35] Ying Chen, Zhenzhen Wang, Yingxun Liu, Xin Wang, Ying Li, Ping Ma, Bing Gu, and Hongchun Li. Recent advances in rapid pathogen detection method based on biosensors. *European Journal of Clinical Microbiology & Infectious Diseases*, 37(6):1021–1037, March 2018.

[36] Vivek Pachauri and Sven Ingebrandt. Biologically sensitive field-effect transistors: from ISFETs to NanoFETs. *Essays in Biochemistry*, 60(1):81–90, June 2016.

[37] Raffaele Campanile, Emanuela Scardapane, Antonio Forente, Carmine Granata, Roberto Germano, Rocco Di Girolamo, Antonio Minopoli, Raffaele Velotta, Bartolomeo Della Ventura, and Vincenzo Iannotti. Core-shell magnetic nanoparticles for highly sensitive magnetoelastic immunosensor. *Nanomaterials*, 10(8):1526, August 2020.

[38] Giorgi Shtenberg and Ester Segal. Porous silicon optical biosensors. In *Handbook of Porous Silicon*, pages 857–868. Springer International Publishing, 2014.

[39] Sofia Arshavsky-Graham, Naama Massad-Ivanir, Ester Segal, and Sharon Weiss. Porous silicon-based photonic biosensors: Current status and emerging applications. *Analytical Chemistry*, 91(1):441–467, November 2018.

[40] Michael J. Sailor. *Porous Silicon in Practice*. John Wiley Sons, Ltd, 2013.

[41] Roselien Vercauteren, Gilles Scheen, Jean-Pierre Raskin, and Laurent A. Francis. Porous silicon membranes and their applications: Recent advances. *Sensors and Actuators A: Physical*, 318:112486, 2021.

[42] Gilles Scheen. Metal electrode integration and palladium nanoparticule functionalization on a miniaturized macroporous silicon chemiresistor. 2015. PhD thesis, Univeristé Catholique de Louvain. Prom. : Francis, Laurent.

[43] Ghenadii Korotcenkov, editor. *Porous Silicon: From Formation to Application: Formation and Properties, Volume One*. CRC Press, April 2016.

[44] O. Bisi, Stefano Ossicini, and L. Pavesi. Porous silicon: a quantum sponge structure for silicon based optoelectronics. *Surface Science Reports*, 38(1-3):1–126, April 2000.

[45] J. Rouquerol, D. Avnir, C. W. Fairbridge, D. H. Everett, J. M. Haynes, N. Pernicone, J. D. F. Ramsay, K. S. W. Sing, and K. K. Unger. Recommendations for the characterization of porous solids (technical report). *Pure and Applied Chemistry*, 66(8):1739–1758, January 1994.

[46] Farid A. Harraz, Said M. El-Sheikh, Tetsuo Sakka, and Yukio H. Ogata. Cylindrical pore arrays in silicon with intermediate nano-sizes: A template for nanofabrication and multilayer applications. *Electrochimica Acta*, 53(22):6444–6451, September 2008.

[47] Andrew Jane, Roman Dronov, Alastair Hodges, and Nicolas H. Voelcker. Porous silicon biosensors on the advance. *Trends in Biotechnology*, 27(4):230–239, April 2009.

[48] L. T. Canham. Silicon quantum wire array fabrication by electrochemical and chemical dissolution of wafers. *Applied Physics Letters*, 57(10):1046–1048, September 1990.

[49] Bomin Cho, Seongwoong Kim, Hee-Gweon Woo, Sungsoo Kim, and Honglae Sohn. Detection of human ig g using photoluminescent porous silicon interferometer. *Journal of Nanoscience and Nanotechnology*, 15(2):1083–1087, February 2015.

[50] Selena Chan, Scott R. Horner, Philippe M. Fauchet, and Benjamin L. Miller. Identification of gram negative bacteria using nanoscale silicon microcavities. *Journal of the American Chemical Society*, 123(47):11797–11798, November 2001.

[51] Claudia Pacholski, Marta Sartor, Michael J. Sailor, Frédérique Cunin, and Gordon M. Miskelly. Biosensing using porous silicon double-layer interferometers: reflective interferometric fourier transform spectroscopy. *Journal of the American Chemical Society*, 127(33):11636–11645, August 2005.

[52] Nalin H. Maniya and Divesh N. Srivastava. Fabrication of porous silicon based label-free optical biosensor for heat shock protein 70 detection. *Materials Science in Semiconductor Processing*, 115:105126, August 2020.

[53] D. Nanda Kumar, Nofar Pinker, and Giorgi Shtenberg. Porous silicon fabry–pérot interferometer forN-acetyl--d-glucosaminidase biomarker monitoring. *ACS Sensors*, 5(7):1969–1976, June 2020.

[54] J. Zheng, M. Christophersen, and P. L. Bergstrom. Thick macroporous membranes made of p-type silicon. *physica status solidi (a)*, 202(8):1402–1406, June 2005.

[55] B. Bardet, S. Desplobain, J. Billoué, L. Ventura, and Gaël Gautier. Integration of low-loss inductors on thin porous silicon membranes. *Microelectronic Engineering*, 194:96–99, July 2018.

[56] Thierry Leïchlé and David Bourrier. Integration of lateral porous silicon membranes into planar microfluidics. *Lab on a Chip*, 15(3):833–838, 2015.

[57] B. Graczykowski, A. El Sachat, J. S. Reparaz, M. Sledzinska, M. R. Wagner, E. Chavez-Angel, Y. Wu, S. Volz, Y. Wu, F. Alzina, and C. M. Sotomayor Torres. Thermal conductivity and air-mediated losses in periodic porous silicon membranes at high temperatures. *Nature Communications*, 8(1), September 2017.

[58] Barrett J. Nehilla, Nakul Nataraj, Thomas R. Gaborski, and James L. McGrath. Endothelial vacuolization induced by highly permeable silicon membranes. *Acta Biomaterialia*, 10(11):4670–4677, November 2014.

[59] Steven R. Gillmer, David Z. Fang, Sarah E. Wayson, Joshua D. Winans, Niaz Abdolrahim, Jon-Paul S. DesOrmeaux, Jirachai Getpreecharsawas, Jonathan D. Ellis, Philippe M. Fauchet, and James L. McGrath. Predicting the failure of ultrathin porous membranes in bulge tests. *Thin Solid Films*, 631:152–160, June 2017.

[60] Yiliang Zhao, Girija Gaur, Scott T. Retterer, Paul E. Laibinis, and Sharon M. Weiss. Flow-through porous silicon membranes for real-time label-free biosensing. *Analytical Chemistry*, 88(22):10940–10948, October 2016.

[61] Yingning He, David Bourrier, Eric Imbernon, and Thierry Leichle. Lateral porous silicon membranes with size and charge selectivity. April 2017.

[62] Neng Yu and Jianmin Wu. Rapid and reagentless detection of thrombin in clinic samples via microfluidic aptasensors with multiple target-binding sites. *Biosensors and Bioelectronics*, 146:111726, December 2019.

[63] Chiara Novara, Andrea Lamberti, Alessandro Chiadò, Alessandro Virga, Paola Rivolo, Francesco Geobaldo, and Fabrizio Giorgis. Surface-enhanced raman spectroscopy on porous silicon membranes decorated with ag nanoparticles integrated in elastomeric microfluidic chips. *RSC Advances*, 6(26):21865–21870, 2016.

[64] M. Terracciano, L. De Stefano, I. Rendina, G. Oliviero, G. Piccialli, N. Borbone, and I. Rea. Aminosilane-modified mesoporous oxidized silicon for in situ oligonucleotides synthesis and detection. *2014 Fotonica AEIT Italian Conference on Photonics Technologies*, pages 1–4, 2014.

[65] Q. Shabir, K. Webb, D. K. Nadarassan, A. Loni, L. T. Canham, M. Terracciano, L. De Stefano, and I. Rea. Quantification and reduction of the residual chemical reactivity of passivated biodegradable porous silicon for drug delivery applications. *Silicon*, 10(2):349–359, April 2017.

[66] J. Salonen, E. Laine, and L. Niinistö. Thermal carbonization of porous silicon surface by acetylene. *Journal of Applied Physics*, 91(1):456–461, 2002.

[67] M. Björkqvist, J. Paski, J. Salonen, and V.-P. Lehto. Temperature dependence of thermally-carbonized porous silicon humidity sensor. *Physica Status Solidi (a)*, 202(8):1653–1657, 2005.

[68] Beniamino Sciacca, Sara D. Alvarez, Francesco Geobaldo, and Michael J. Sailor. Bioconjugate functionalization of thermally carbonized porous silicon using a radical coupling reaction. *Dalton Trans.*, 39:10847–10853, 2010.

[69] S Franssila. *Introduction to Microfabrication*. John Wiley Sons, Ltd, 2010.

[70] Michelle M. Gauthier, editor. *Engineered Materials Handbook Desk Edition*. ASM International, 1995.

[71] K.R. Williams, K. Gupta, and M. Wasilik. Etch rates for micromachining processing-part II. *Journal of Microelectromechanical Systems*, 12(6):761–778, December 2003.

[72] Merck KGaA, Darmstadt, Germany. *AZ® MiR™ 701 Series*, 3 2016. Available at: https://www.microchemicals.com/micro/tds_az_mir701_photoresist.pdf.

[73] Merck KGaA, Darmstadt, Germany. *AZ® nLOF™ 5510*, 5 2016. Available at: https://www.microchemicals.com/micro/tds_az_nlof5510_photoresist.pdf.

[74] S Billat, M Thönissen, R Arens-Fischer, M.G Berger, M Krüger, and H Lüth. Influence of etch stops on the microstructure of porous silicon layers. *Thin Solid Films*, 297(1-2):22–25, April 1997.

[75] Han-Su Kim, Eric C. Zouzounis, and Ya-Hong Xie. Effective method for stress reduction in thick porous silicon films. *Applied Physics Letters*, 80(13):2287–2289, April 2002.

[76] Véronique Cremers, Riikka L. Puurunen, and Jolien Dendooven. Conformality in atomic layer deposition: Current status overview of analysis and modelling. *Applied Physics Reviews*, 6(2):021302, June 2019.

[77] Joseph I. Goldstein, Dale E. Newbury, Patrick Echlin, David C. Joy, Charles E. Lyman, Eric Lifshin, Linda Sawyer, and Joseph R. Michael. Generation of x-rays in the SEM specimen. In *Scanning Electron Microscopy and X-ray Microanalysis*, pages 271–296. Springer US, 2003.

[78] Buddy D. Ratner and David G. Castner. Electron spectroscopy for chemical analysis. In *Surface Analysis– The Principal Techniques*, pages 47–112. John Wiley & Sons, Ltd, 2009.

[79] H. Hantsche. Comparison of basic principles of the surface-specific analytical methods: AES/SAM, ESCA (XPS), SIMS, and ISS with x-ray microanalysis, and some applications in research and industry. *Scanning*, 11(6):257–280, 1989.

[80] Wei Han, Huisheng Jiao, and Daniel Fox. Scanning electron microscopy. In *Springer Tracts in Modern Physics*, pages 35–68. Springer Singapore, 2018.

[81] Leigh Canham. Mechanical properties of porous silicon. In *Handbook of Porous Silicon*, pages 213–220. Springer International Publishing, 2014.

[82] D. Bellet, P. Lamagnère, A. Vincent, and Y. Bréchet. Nanoindentation investigation of the young's modulus of porous silicon. *Journal of Applied Physics*, 80(7):3772–3776, October 1996.

[83] Xiaoyue Gong, Julien Bustillo, Laurianne Blanc, and Gaël Gautier. FEM simulation on elastic parameters of porous silicon with different pore shapes. *International Journal of Solids and Structures*, 190:238–243, May 2020.

[84] H. Föll, M. Christophersen, J. Carstensen, and G. Hasse. Formation and application of porous silicon. *Materials Science and Engineering: R: Reports*, 39(4):93–141, November 2002.

[85] Hélène Magoariec and Alexandre Danescu. Modeling macroscopic elasticity of porous silicon. *physica status solidi (c)*, 6(7):1680–1684, July 2009.

[86] Anthony C. Fischer-Cripps. Nanoindentation testing. In *Nanoindentation*, pages 21–37. Springer New York, 2011.

[87] W.C. Oliver and G.M. Pharr. Measurement of hardness and elastic modulus by instrumented indentation: Advances in understanding and refinements to methodology. *Journal of Materials Research*, 19(1):3–20, January 2004.

[88] Gaylord Guillonneau, Guillaume Kermouche, Sandrine Bec, and Jean-Luc Loubet. Determination of mechanical properties by nanoindentation independently of indentation depth measurement. *Journal of Materials Research*, 27(19):2551–2560, August 2012.

[89] W.C. Oliver and G.M. Pharr. An improved technique for determining hardness and elastic modulus using load and displacement sensing indentation experiments. *Journal of Materials Research*, 7(6):1564–1583, June 1992.

[90] Dong-Kwon Kim, Chuanhua Duan, Yu-Feng Chen, and Arun Majumdar. Power generation from concentration gradient by reverse electrodialysis in ion-selective nanochannels. *Microfluidics and Nanofluidics*, 9(6):1215–1224, June 2010.

[91] Stefano Mariani, Laura Pino, Lucanos M. Strambini, Lorena Tedeschi, and Giuseppe Barillaro. 10000-fold improvement in protein detection using nanostructured porous silicon interferometric aptasensors. *ACS Sensors*, 1(12):1471–1479, December 2016.

[92] E. Segal, L. A. Perelman, F. Cunin, F. Di Renzo, J.-M. Devoisselle, Y. Y. Li, and M. J. Sailor. Confinement of thermoresponsive hydrogels in nanostructured porous silicon dioxide templates. *Advanced Functional Materials*, 17(7):1153–1162, April 2007.

[93] Shannon Mahurin, Lili Bao, Wenfu Yan, Chengdu Liang, and Sheng Dai. Atomic layer deposition of TiO2 on mesoporous silica. *Journal of Non-Crystalline Solids*, 352(30-31):3280–3284, September 2006.

[94] W. Z. Wan Ismail, K. S. Sim, C. P. Tso, and H. Y. Ting. Reducing charging effects in scanning electron microscope images by rayleigh contrast stretching method (RCS). *Scanning*, 33(4):233–251, May 2011.

[95] J. Robertson. High dielectric constant oxides. *The European Physical Journal Applied Physics*, 28(3):265–291, December 2004.

[96] Hans Conrad and Jack Hall Westbrook. In *American Society of Metals*, pages 453–491. Metals Park, 1973.

[97] K.E. Petersen. Dynamic micromechanics on silicon: Techniques and devices. *IEEE Transactions on Electron Devices*, 25(10):1241–1250, October 1978.

[98] S.P. Duttagupta, X.L. Chen, S.A. Jenekhe, and P.M. Fauchet. Microhardness of porous silicon films and composites. *Solid State Communications*, 101(1):33–37, January 1997.

[99] Zhen qian Fang, Ming Hu, Wei Zhang, Xu rui Zhang, and Hai bo Yang. Mechanical properties of porous silicon by depth-sensing nanoindentation techniques. *Thin Solid Films*, 517(9):2930–2935, March 2009.

[100] Chun Kwan Tsang, Timothy L. Kelly, Michael J. Sailor, and Yang Yang Li. Highly stable porous silicon–carbon composites as label-free optical biosensors. *ACS Nano*, 6(12):10546–10554, November 2012.

[101] Maria Ariza-Avidad, Alejandra Nieto, Alfonso Salinas-Castillo, Luis F Capitan-Vallvey, Gordon M Miskelly, and Michael J Sailor. Monitoring of degradation of porous silicon photonic crystals using digital photography. *Nanoscale Research Letters*, 9(1):410, 2014.

[102] Jonathan Rasson and Laurent A. Francis. Improved stability of porous silicon in aqueous media via atomic layer deposition of oxides. *The Journal of Physical Chemistry C*, 122(1):331–338, December 2017.

[103] Siqi Zhuo, Mingyue Xun, Mingda Li, Xiaoxue Kong, Rui Shao, Tiesong Zheng, Daodong Pan, Jianlin Li, and Qianjin Li. Rapid and label-free optical assay of s-layer protein with high sensitivity using TiO2-coated porous silicon-based microfluidic biosensor. *Sensors and Actuators B: Chemical*, 321:128524, October 2020.

[104] Nekane Reta, Andrew Michelmore, Christopher P. Saint, Beatriz Prieto-Simon, and Nicolas H. Voelcker. Label-free bacterial toxin detection in water supplies using porous silicon nanochannel sensors. *ACS Sensors*, 4(6):1515–1523, May 2019.

[105] Katharina Urmann, Johanna-Gabriela Walter, Thomas Scheper, and Ester Segal. Label-free optical biosensors based on aptamer-functionalized porous silicon scaffolds. *Analytical Chemistry*, 87(3):1999–2006, January 2015.

[106] Allaa A. Jabbar, Alwan M. Alwan, Mehdi Q. Zayer, and Azhar J. Bohan. Efficient single cell monitoring of pathogenic bacteria using bimetallic nanostructures embedded in gradient porous silicon. *Materials Chemistry and Physics*, 241:122359, February 2020.

[107] Katrin-Stephanie Tücking, Roshan B. Vasani, Alex A. Cavallaro, Nicolas H. Voelcker, Holger Schönherr, and Beatriz Prieto-Simon. Hyaluronic acid-modified porous silicon films for the electrochemical sensing of bacterial hyaluronidase. *Macromolecular Rapid Communications*, 39(19):1800178, May 2018.

[108] Hongyan Zhang, Jie Lv, and Zhenhong Jia. Detection of ammonia-oxidizing bacteria (AOB) using a porous silicon optical biosensor based on a multilayered double bragg mirror structure. *Sensors*, 18(2):105, January 2018.

[109] Elena Tenenbaum and Ester Segal. Optical biosensors for bacteria detection by a peptidomimetic antimicrobial compound. *The Analyst*, 140(22):7726–7733, 2015.

[110] Mona Yaghoubi, Fereshteh Rahimi, Babak Negahdari, Ali Hossein Rezayan, and Azizollah Shafiekhani. A lectin-coupled porous silicon-based biosensor: label-free optical detection of bacteria in a real-time mode. *Scientific Reports*, 10(1), September 2020.

[111] K. Urmann, S. Arshavsky-Graham, J. G. Walter, T. Scheper, and E. Segal. Whole-cell detection of live lactobacillus acidophilus on aptamer-decorated porous silicon biosensors. *The Analyst*, 141(18):5432–5440, 2016.

[112] Naama Massad-Ivanir, Giorgi Shtenberg, Nitzan Raz, Christel Gazenbeek, Dries Budding, Martine P. Bos, and Ester Segal. Porous silicon-based biosensors: Towards real-time optical detection of target bacteria in the food industry. *Scientific Reports*, 6(1), November 2016.

[113] Yanyan Tang, Zhen Li, Qiaohui Luo, Jingqing Liu, and Jianmin Wu. Bacteria detection based on its blockage effect on silicon nanopore array. *Biosensors and Bioelectronics*, 79:715–720, May 2016.

[114] Yiliang Zhao, Girija Gaur, Raymond L. Mernaugh, Paul E. Laibinis, and Sharon M. Weiss. Comparative kinetic analysis of closed-ended and open-ended porous sensors. *Nanoscale Research Letters*, 11(1), September 2016.

[115] David Martin-Sanchez, Salvador Ponce-Alcantara, and Jaime Garcia-Ruperez. Sensitivity comparison of a self-standing porous silicon membrane under flow-through and flow-over conditions. *IEEE Sensors Journal*, 19(9):3276–3281, May 2019.

[116] G. Dingemans, F. Einsele, W. Beyer, M. C. M. van de Sanden, and W. M. M. Kessels. Influence of annealing and al2o3 properties on the hydrogen-induced passivation of the si/SiO2 interface. *Journal of Applied Physics*, 111(9):093713, May 2012.

[117] Weifang Lu, Yoshimi Iwasa, Yiyu Ou, Daiki Jinno, Satoshi Kamiyama, Paul Michael Petersen, and Haiyan Ou. Effective optimization of surface passivation on porous silicon carbide using atomic layer deposited al2o3. *RSC Advances*, 7(14):8090–8097, 2017.

[118] Rabeb Layouni, Moinul H. Choudhury, Paul E. Laibinis, and Sharon M. Weiss. Thermally carbonized porous silicon for robust label-free DNA optical sensing. *ACS Applied Bio Materials*, 3(1):622–627, December 2019.

UNIVERSITÉ CATHOLIQUE DE LOUVAIN
École polytechnique de Louvain
Rue Archimède, 1 bte L6.11.01, 1348 Louvain-la-Neuve, Belgique | **www.uclouvain.be/epl**